Interplay between spin, heat, and charge currents in strongly correlated systems

A thesis

Submitted in partial fulfillment of the requirements

Of the degree of

DOCTOR OF PHILOSOPHY

by:

Avirup De

Registration ID : 20133278

Indian Institute of Science Education and Research,

Pune-411008, India

July, 2020

Dedicated to my parents

Certificate

Certified that the work incorporated in the thesis entitled **"Interplay between spin, heat, and charge currents in strongly correlated systems"** Submitted by ***Avirup De*** was carried out by the candidate, under my supervision. The work presented here or any part of it has not been included in any other thesis submitted previously for the award of any degree or diploma from any other University or institution.

Pune
Date: November 20, 2020

(Dr. Sunil Nair)
Thesis Supervisor

Declaration

I declare that this written submission represents my ideas in my own words and where others' ideas have been included, I have adequately cited and referenced the original sources. I also declare that I have adhered to all principles of academic honesty and integrity and have not misrepresented or fabricated or falsified any idea/data/fact/source in my submission. I understand that violation of the above will be cause for disciplinary action by the Institute and can also evoke penal action from the sources which have thus not been properly cited or from whom proper permission has not been taken when needed.

Pune
November 20, 2020

(Avirup De)
ID: 20133278

Acknowledgements

Here, I take the opportunity to express my gratitude to the following individuals whose direct or indirect supports, advice, and encouragement carved me to the successful completion of this work.

First and foremost, I wish to thank my doctoral supervisor, Dr. Sunil Nair, for introducing me to this research field, giving me the liberty to work in the lab, guiding me during instrumentation, advising through many scientific discussions and importantly, keeping me optimistic throughout the research activities. I have learned a great deal from his methodology of dealing with scientific problems, as well as his way of handling the challenges in setting up a facility in the lab. I would also like to acknowledge his efforts in improving my writing skill by a substantial amount, and thus I am also thankful to him for all the detailed revisions made to my manuscripts. Finally, I am grateful to him for being my guide on this long voyage towards Ph.D.

Next, I want to thank my Research Advisory Committee, consisting of Dr. Pattayil Joy (NCL, Pune) and Prof. Satishchandra B. Ogale (IISER, Pune). I thank them for their feedback and insightful suggestions during the annual meetings throughout the Ph.D. tenure. I am also grateful to Prof. Satishchandra B. Ogale for his invaluable assistance in depositing thin films via the Pulsed Laser deposition technique.

I want to thank Dr. Sanjay Singh (IIT-BHU), Anupam Kumar Singh (IIT-BHU), and Dr. Dharmalingam Prabhakaran (University of Oxford) for providing excellent samples to investigate various Spin-Caloritronic signals. It is my great pleasure to acknowledge

their assistance that directly helped us in the investigations presented in this thesis.

I wish to thank Dr. Surjeet Singh for his invaluable support, encouragement, and friendly gestures. I am privileged to get smooth access to the PPMS in his lab.

I would like to thank Dr. Shouvik Datta for providing me the liberty to operate both the sputtering unit and optical lithography unit during the days of my Ph.D.

I want to extend my gratitude to all other IISER faculties. I especially thank Dr. Mukul Kabir, Dr. Ashna Bajpai, Dr. Arijit Bhattacharyay, and Dr. Umakant D Rapol for their support and friendly gestures.

I thankfully acknowledge the University Grants Commission (UGC) and IISER, Pune, for the financial support during my Ph.D. tenure. I would also acknowledge the Infosys Foundation and 2019 Joint MMM-Intermag conference organizers for supporting my travels towards attending international conferences.

I wish to express my heartfelt gratitude to all of my teachers; whose positivity and encouragement brightened my days. You made me a better, more thoughtful person.

I want to extend my gratitude to all the technical staff whose support in setting up the Spin-Caloritronic unit, as well as maintaining the existing facilities, are highly appreciable. Specifically, I thank Mr. Nilesh Dumbre, Mr. Prashant Kale, Mr. Praveen Nasa, Mr. Sudhir Lone, and Mr. T. S. Yathish.

I am thankful to Rajesh Mandal, Shatruhan Singh Rajput, Dibyata Rout, Dr. Rabindranath Bag, Umashankar Rajput, Mulani Imrankhan, Prachi Telang, Kumar Sourabh, Ajith V. J., Dr.Namrata Pattanayak, Aakanksha Kapoor, and Chandan Kumar Singh. All these friends helped me in many ways. I will remember Ajith for his enthusiastic help in learning LABVIEW programming. I acknowledge Shatruhan and Umashankar for assisting me in the AFM measurements. I thank Dibyata and Prachi for their support

during the measurements in PPMS, and others for many remarkable scientific discussions. Finally, I thank Rajesh for his enthusiastic assistance in the fabrication of thin films via the Pulsed Laser deposition technique.

I would like to thank all of my present and former lab-mates: Dr. Soumendra Nath Panja, Dr. Arup Ghosh, Shruti Chakravarty, Dr. Jitender Kumar, Kaustav Dey, Dr. Rohit Kumar, Dr. U. Devarajan, Dr. Abhijit Biswas, Devika Dayanandan, Shanu Dengre, Deepak John Mukkattukavil, Vignesh Sundar, Dr. Shruti, Haritha S. V., Charu Garg, Dr. Ashoka Bali, Vikram Patil, Anna Merin Francis, Sharat, and Dipanjali Halder. In particular, I acknowledge Dr. Arup Ghosh for his enthusiastic assistance during instrumentation. Specifically, I remember that we set together to find out the noise source, and thus we have gone through the tedious job of wiring during instrumentation.

I thank all of my friends in IISER, Pune. In particular, I would like to mention some of them: Amit, Sumit, Chetan, Deepak, Gunjan, Mainak, Shubhanshu, Pulastya, and Milan.

I thank Rituparna, who always encourage me and support me. Finally, I would like to take this opportunity to acknowledge my family, especially my parents, for their continuous support, blessings, love, and encouragement.

Contents

Synopsis

Understanding the interplay between spin, heat, and charge currents is of fundamental importance in the area of Spintronics, where the spin degree of freedom plays a crucial role. The interaction between spin and heat currents alone is classified as the Spin-Caloritronics, which is basically a newly emerging sub-field of Spintronics. Depending on the nature of interaction among spin, heat, and charge degrees of freedom, various kinds of thermally driven spintronic phenomena are observed; and among them, three distinct phenomena are now being actively investigated: (I) The Spin Seebeck effect (SSE), (II) The anomalous Nernst effect (ANE), and (III) The magnon Hall effect (MHE).

(I) The Spin Seebeck effect: This pertains to the generation of pure spin current under the application of a temperature gradient (∇T) across a magnetic material [1–5]. A reliable way to detect this spin current is to use a normal metal (NM) with a large spin Hall angle, e.g., Pt, Ta, or W, on top of the magnetic material. Thermally induced spin current is then pumped into the NM layer via the interfacial exchange interaction between itinerant and localized electrons across the interface, which further gives rise to a transverse voltage via the inverse spin Hall effect (ISHE) [4–8].

(II) The anomalous Nernst effect: This pertains to the generation of a transverse electrical voltage across a magnetic system under the application of a longitudinal thermal gradient. In particular, the ANE is defined in the direction orthogonal to both magnetization and the applied temperature gradient, where the ANE-voltage stems from the

interaction between the conduction electrons with the local magnons under the influence of spin-orbit interactions [9–11].

(III) The magnon Hall effect: This describes the Hall effect of magnon current. Even though the magnons are charged neutral, they exhibit Hall transport that stems from the Berry curvature of the magnon bands [12–15]. Experimentally, the MHE is quantified in terms of the thermal Hall effect of magnons (THEM), which pertains to the generation of a transverse thermal gradient (∇T_{zx}) by the spin excitations (magnons) due to the application of a longitudinal thermal gradient across the magnetic material [12, 15].

This thesis is divided into six parts:

Chapter 1: This Chapter provides an introduction to the research area of Spin-Caloritronics, where the possible mechanisms of the generation, detection, and characterization of various Spin-Caloritronic signals are described in brief. In particular, the issues associated with the (i) SSE, (ii) ANE, and (iii) MHE are highlighted.

Chapter 2: Here we provide the details of the experimental set-up that was designed and developed during the course of this thesis for the sensitive measurements of SSE, ANE, and MHE. The set-up comprises of a closed cycle refrigerator (CCR), a temperature controller, a nano-voltmeter, a source meter, and an electromagnet with an upper field limit of 2 kOe. Two PID controlled heaters control the temperature gradient across the sample, as well as the average temperature of the sample, where the temperatures of the opposite ends of the sample are sensed by two temperature sensors attached near the sample edges. The holder's geometry is so designed that the applied thermal gradient is always orthogonal to the rotation plane of the magnetic field. The whole setup is kept inside a Faraday cage to reduce the noise, and signals as low as 10nV can be reliably measured.

Chapter 3: In this chapter, we discuss the detailed investigations of the longitudinal spin Seebeck effect (LSSE), as measured in the $La_{0.7}Ca_{0.3}MnO_3$/Pt bilayer system. We show that the longitudinal spin Seebeck voltage (V_{LSSE}) is proportional to $T^{0.5}$ in low temperatures, which matches well with that predicted by the magnon-driven spin current model. On the other hand, the critical exponent of V_{LSSE} near the para-to-ferromagnetic transition is found to be much higher than that of the magnetization, and also depends on the thickness of the spin-to-charge conversion layer (the NM layer). These observations highlight the importance of individually ascertaining the temperature evolution of different mechanisms – especially the spin mixing conductance – which contribute to the measured spin Seebeck signal.

Chapter 4: This chapter describes detailed investigations of the $Ni_{1.96}Mn_{1.04}Ga$ system through various magnetic, electronic, and thermal characterizations. Upon cooling, such a material undergoes many sequential phase transitions, like, the pre-martensitic transition (PMT) and martensitic transition (MT). The ANE is primarily investigated, and our measurements of the ANE reveal that it is very sensitive to these phase transitions. In particular, a pronounced change in the ANE signal is observed across the pre-martensitic phase of this material, whereas such a change in other transport and magnetic measurements remains faint. With the ANE being sensitive to changes at the Fermi surface, we have discussed the possible coupling between local magnetism and the Fermi surface – where, the ANE is tuned by the magnetic field-driven changes at the Fermi surface.

Chapter 5: This chapter presents detailed investigations of the THEM-signal in single-crystalline $Y_2V_2O_7$ specimens. The measurements were performed in two different crystals whose planes are cut and polished into two different orientations, {100} and {111}. Unlike the previous experimental detection method [12, 15], we measure

the ∇T_{zx} by putting a thin non-magnetic normal metal (NM), like, Pt, or W, on top of the crystal's plane. The THEM-signal is then quantified in terms of thermo-power, generated along the length of the NM-bar (also called as the detection layer). In contrast to the prior reports, where the ∇T_{zx} was directly measured by utilizing thermocouples [12, 15], our method significantly improves the signal to noise ratio. The detailed investigation on the $Y_2V_2O_7$ crystals reveals that a significant part of the observed THEM signal is contributed by the magnons of the higher energy bands. This is in contrast to the previous report, where only the contribution of the lowest magnon-band was considered to have a role in dictating the THEM-signal [12, 15]. Additionally, the crystal with {111} planes is observed to display a significant magnon drag effect at the interface with that NM layer − which is further linked to the topologically protected chiral surface state of magnons.

Chapter 6: This chapter presents the conclusions of the work described in this thesis, along with possible future directions.

List of Publications

Publications included in this thesis

1. **Temperature Dependence of the Spin Seebeck Effect in a Mixed Valent Manganite**

   Avirup De, Arup Ghosh, Rajesh Mandal, Satishchandra Ogale, and Sunil Nair;

   Phys. Rev. Lett. **124**, 017203 (2020).

2. **Temperature dependence of the anomalous Nernst effect in Ni_2MnGa shape memory alloy**

   Avirup De, Anupam K. Singh, Sanjay Singh, and Sunil Nair;

   Under review in Phys.Rev.B (Rapid communication) (2020).

3. **The magnon Hall effect in single crystalline $Y_2V_2O_7$ specimen**

   Avirup De, Dharmalingam Prabhakaran, and Sunil Nair;

   (Manuscript under preparation (2020))

Publications not included in this thesis

1. **Large anomalous Nernst effect across the magneto-structural transition in a bulk Ni-Co-Mn-Sn full Heusler alloy**

   Arup Ghosh, Avirup De and Sunil Nair;

   Appl. Phys. Lett. 113, 262405 (2018).

Chapter 1

Introduction

In this 21st century, the shape of our society hugely depends on the usage of scientific inventions and technological achievements. This is particularly so in the field of information and communication technology, where the goals are set to make progress of the electronic devices in terms of capacity to store more information in a tiny chip, speed for faster performance, and flexibility for better usage. For instance, one can imagine a computer from the old days used to take a whole room, to a modern-computer of the size of a laptop or tab, kept inside a handbag. Speaking in terms of memory, an old computer from the 1980s used to have a floppy with a few hundred kilobytes (KB) memory, whereas a modern-computer have around 8-gigabyte random access memory (RAM). However, as these devices gain in performance, with their sizes getting smaller and smaller − reaching to the nanoscale − it becomes increasingly difficult to precisely channel the electric charges to where they are needed. Moreover, the continuous miniaturization of the device size for achieving higher circuit densities causes a large leakage current that results in significant power dissipation − limiting the possibilities with the charge-based technologies [16–19]. In this background, new concepts to replace these nanoscale electronic devices has become a hot topic of research for the development of new modern technologies.

1.1 Introduction to Spintronics & Spin-Caloritronics

Conventional electronic devices, like transistors or diodes, work to control the flow of electric charges in the integrated circuits. As an alternative approach, the utilization of spins within the mainstream of electronics became an attractive topic of research in the late 20th century [20]. In this context, in 1936, N. F. Mott first introduced the famous two-spin channel model in order to explain the sudden increase in resistivity of ferromagnetic metals as they are heated above the Curie temperature [21]. It is worth mentioning that the two-spin channel model basically describes the total conductivity of metals as a combination of two spin-dependent conducting channels, corresponding to the up-spin and down-spin electrons, which are distinguished according to the projection of their spins along the quantization axis. This laid the foundation for the search of spin-dependent transport in materials. One of the remarkable breakthroughs that came in its way is the discovery of the giant magnetoresistance (GMR) [22, 23], taking the spin-dependent transport phenomena to new heights. Albert Fert and Peter Grunberg received the Nobel prize in 2007 for their independent contributions to the discovery of the GMR in 1988 − the cornerstone of the Spintronics. The basic principle of the GMR is commonly understood in a spin valve scenario, where a non-magnetic metal separates two ferromagnetic (FM) layers with different magnetic switching fields. In the parallel configuration of the magnetization vectors of both FM layers, electrons with spins parallel to the magnetization can flow without significant scattering that lead to a low-resistance state. On the other hand, the anti-parallel configuration of the magnetization vectors, all the electrons with both spin-types, face significant scattering that result in a high-resistance state. Within a decade, a plethora of research activities has made substantial progress in this direction through the discovery of tunnel magnetoresistance

(TMR) [24–26], where an insulating spacer material replaces the non-magnetic metal of the conventional GMR device – making it more effective in terms of much larger magnetoresistance effect. Today, the GMR and the TMR devices have revolutionized the field of solid-state technology in terms of nonvolatile solid-state memory devices, magnetoresistive random-access memory, and fast programmable logic circuits. Thus, the utilization of the spin degree of freedom acts as an impetus for the energy-efficient, productive, and reliable technologies for future progress [20, 27–29].

Spintronics is one of the emerging disciplines that aims at the development of a new generation of devices relying on the manipulation of the electron's spin. It encompasses various fundamental interactions with other physical quantities that become imperative for the understanding of practical implications [28, 30]. In the last few decades, the collaboration of electric charge with the spin has advanced in the direction of spin-dependent electric transport [31, 32]. Besides the coupling between spin and charge degrees of freedom, the utilization of pure spin-current is now considered for future technologies, where modern researches are focused on understanding the generation, detection, and characterization of such spin-current in material systems [20, 33]. In this context, the issues that deal with the interaction of spins with the heat-current are clubbed to form a new subgroup of Spintronics, called Spin-caloritronics [34–36].

1.2 Fundamental Concepts

In reality, materials consist of complex interactions that offer significant inter-coupling among all current densities with their carries and driving forces. For instance, a thermal gradient applied across a semi-conductor results in a heat-current inside the material – however, conduction electrons are also influenced by the same thermal gradient that

generate charge-current known as thermopower. Another example would be the role of an electric field, which generates a charge-current, can also be responsible for the generation of thermal gradient characterized by the Peltier coefficients. This complex interplay could be described in a more straightforward contemporary way of thermodynamic approaches in terms of the Onsager's reciprocity theorem.

In 1854, William Thomson first introduced a thermodynamic approach in search of the link between the Seebeck and the Peltier coefficients [37, 38]. Almost seventy years later, Lars Onsager, extended the work of Thomson to a more generalised version, and derived the celebrated reciprocal relations between irreversible processes [39, 40]. According to this theory, every flux of a certain quantity x_i within a system is given by the linear combination of driving forces: $j_{x_i} = \sum_{ij} T_{ij}\zeta_j$, where j_{x_j} is the current flux of a certain quantity, ζ_j represents the driving forces for that current, and T_{ij} is the Onsager matrix of transport coefficients that satisfy the reciprocity relation between symmetric elements e.g. T_{ij} and T_{ji}. A concise description of the Onsager reciprocal relations for a material system could be expressed as [35]:

$$\begin{pmatrix} j_c \\ j_s \\ j_q \end{pmatrix} = \begin{pmatrix} T_{cc} & T_{cs} & T_{cq} \\ T_{sc} & T_{ss} & T_{sq} \\ T_{qc} & T_{qs} & T_{qq} \end{pmatrix} \cdot \begin{pmatrix} E \\ \nabla\mu_s \\ -\nabla T \end{pmatrix} \tag{1.1}$$

where, j_c, j_s, j_q, E, $\nabla\mu_s$, and ∇T are the charge-current, spin-current, heat-current, electric field, spin chemical potential and thermal gradient respectively. It shows the linear connection between the current densities like j_c, j_s, and j_q with the force-terms like E, $\nabla\mu_s$, and ∇T through the Onsager matrix of transport coefficient, T_{ij}. Each element of the T_{ij} matrix describes a distinct transport mechanism. For instance, the

total charge-current is given by (obtained from Equation 1.1):

$$j_c = T_{cc}E + T_{cs}\nabla\mu_s - T_{cq}\nabla T \tag{1.2}$$

where T_{cc} describe the generation of charge-current by the application of electric field, and thus is called the conductivity tensor – Ohm's law of electrical transport and various electrical Hall effect [41] are linked with this tensor. Similarly, the second term, T_{cs} pertains to the role of spin chemical potential for the generation of the charge-current, i.e. the inverse spin Hall effect [42–44]. The third term, T_{cq} is a representative tensor of the Seebeck and Nernst effects (including the anomalous Nernst and planar Nernst effects) [45–47]. Quantities that are connected to the charge-current are well-known in literature – however, the relations for other currents, like, j_s or j_q predicts more possible physical phenomena, and some of them have only been discovered very recently.

The expression for the total spin-current is given by:

$$j_s = T_{sc}E + T_{ss}\nabla\mu_s - T_{sq}\nabla T \tag{1.3}$$

where, the T_{sc} suggests the generation of pure spin-current under the application of a charge-current, and the discovery of the spin Hall effect phenomena would be an example of this kind [48]. The second term T_{ss} describes the effects of spin accumulations on the generation of spin currents, e.g. the magnon Hall effect [12]. Similarly, the third term, T_{sq} pertains to the generation of spin-current under the application of a thermal gradient, with the spin Seebeck effect [1, 2, 7] and the spin Nernst effect [49, 50] being perfect examples of this quantity.

In analogy with j_s and j_c, the expression for the total heat current (j_q) is given by.

$$j_q = T_{qc}E + T_{qs}\nabla\mu_s - T_{qq}\nabla T \tag{1.4}$$

where, T_{qc} deals with the heat transport by the conduction electrons, T_{qs} deals with the heat transport by the magnons, and T_{qq} pertains to the generation of heat-current by phonons. Physical phenomena like the conventional Peltier effect [51, 52], spin Peltier effect [53, 54], and the phonon Hall effect [55–58] are linked with these T_{qc}, T_{qs}, and T_{qq} transport coefficients, respectively. Thus, the Onsager reciprocity relations portrays a complete set of transport mechanisms that are possible in the physical systems. A sub-set of that dealing with the interaction of "spin" with the heat-current is considered as Spin-caloritronics. This thesis mainly covers the detailed studies of the spin Seebeck effect, anomalous Nernst effect, magnon Hall effect in three different material systems.

1.2.1 Spin current

By definition, the spin-current is described as the flow of spin angular momentum [35, 59, 60]. In mathematical description it could be written as [60, 61]:

$$j_s = \sum_k s_k^z v_k \tag{1.5}$$

where s_z^k is the z-component of the spin-current density s_k whose spin-quantization is along the z-direction, and v_k is the velocity of the elementary excitation associated with s_k. In materials, there are two different types of carriers for the spin-current. One is the conduction electron, which is associated with its own intrinsic spin-angular momentum, and can contribute to the net spin-current by the spin dependent flow of electrons. The

other one is magnon, i.e. the quantized version of spin-waves.

The concept of pure spin-current does not consider any charge flow along with it. Thus, in the case of conduction electron spin-current, it requires the flow of oppositely spin polarised electrons in the equal and opposite direction, so that it cancels the charge current but develops a net spin chemical potential. In this case, $s_k^z = f_{k,\uparrow}^\dagger f_{k,\uparrow} - f_{k,\downarrow}^\dagger f_{k,\downarrow}$. The symbol $f_{k,\sigma}^\dagger$ stands for the creation operator for an electron of momentum k and spin polarization σ (=↑ or ↓). Similarly, $f_{k,\sigma}$ is a representation of an annihilation operator of a conduction electron with specific spin polarization σ and momentum k. Thus, the contribution of conduction electron to the spin-current will have the form [60–62]:

$$j_s^{el} = I^\uparrow - I^\downarrow = \sum_k v_k \left(\left\langle f_{k,\uparrow}^\dagger f_{k,\uparrow} \right\rangle - \left\langle f_{k,\downarrow}^\dagger f_{k,\downarrow} \right\rangle \right) \tag{1.6}$$

where, j_s^e, $I_\uparrow$, $I_\downarrow$, v_k represent the net spin-current due to conduction electrons, charge-current with spin-up polarizations, charge-current with spin-down polarizations, and velocity of conduction electrons of momentum k, respectively. After considering the statistical average, one can define the net spin-current, j_s^{el} that requires an asymmetry between the up-spin population and the down-spin population to obtain a nonzero value. Fig.1.1 (a)-(c) depicts the role of conduction electrons for the generation of spin-current. For instance, Fig.1.1(a) depicts a net charge current, where the net spin-current is zero because the current of spin-up electrons is equal and in the same direction of the current of spin-down electrons, causing a total cancellation in the transport of spin angular momentum in that direction. Fig.1.1(b) shows a spin-polarized charge current, which is also associated with a non-vanishing spin-current. Here, the current of spin-up electrons is larger than that of the spin-down electrons, which develops a net flow of spin angular momentum in that direction. Fig.1.1(c) depicts a pure spin-current with electrons as a carrier. In this particular case, the net charge-current is zero because the flow of

spin-up and spin-down electrons are equal and opposite direction, which contributes to a net spin-voltage in the horizontal direction with a total cancellation of electric voltage.

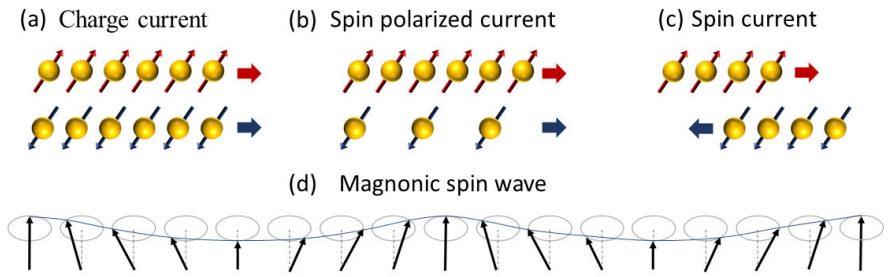

Figure 1.1: (a) pure charge-current, (b) spin polarised charge-current that takes partial contribution to the flow of spin angular momentum, (c) pure spin-current due to the conduction electrons, and (d) pure spin-current due to spin wave.

One of the main problems with the conduction electron spin-current is that its spin diffusion length is very small ($\approx$ 10nm) that sets an upper limit to the propagation length of the spin current. In contrast, the magnons can carry spin angular momentum to a much longer length scale ($\approx 1 - 10$ mm). Moreover, it is not associated with any charge current. Thus, magnons are widely considered for the generation of pure spin current. Fig.1.1(d) depicts the magnon driven spin-current, where the main requirement is to have a long-range magnetic ordering inside a material. In this case, the spin density could be written as $s_k^z = S_0 - b_k^\dagger b_k$, where $b_k^\dagger$ is the creation operator of magnon. Thus, from Equation 1.5, the magnonic contribution to the spin-current could be written as [61, 62] :

$$j_s^m = \sum_k v_k \left(\left\langle b_k^\dagger b_k \right\rangle - \left\langle b_{-k}^\dagger b_{-k} \right\rangle \right) \tag{1.7}$$

with the magnon velocity v_k that holds the relation $v_{-k} = -v_k$. The magnonic expression for the spin-current suggests that the asymmetry between the left-moving population of magnon and the right-moving population of magnon is necessary to obtain a

non-zero magnon current.

1.2.2 Spin-charge inter conversion

Since spin-current is not associated with the charge of its carries, the detection of spin-current or spin-voltage is not trivial. An inter conversion between pure spin-current and charge-current (spin-current ↔ charge-current) plays a crucial role in the detection, and as well as the quantification of the spin-current.

1.2.2.1 Spin Hall effect

The spin Hall effect (SHE) acts as the central mechanism for the conversion of a charge-current into a transverse spin-current inside nonmagnetic metallic systems with a large spin Hall angle. Due to spin-orbit interaction, a flow of electric charges can induce a transverse spin flow (or spin-current) even in the absence of an external magnetic field [48, 63–65]. Dyakonov and Perel first proposed this phenomenon in 1971 [66], and after that, it took almost thirty years for experimental detection of this quantity. Initially, SHE was detected by an optical detection-technique [67], and later electrical-detection has been demonstrated [68]. Nowadays, SHE has become a versatile tool for the generation of spin-current inside a nonmagnetic system which in turn can be used either to excite spin waves in an adjacent magnetic system or to switch the magnetization of an adjacent ferromagnet [69, 70]. Fig.1.2(a) depicts a macroscopic picture of the SHE, which illustrates the spin-dependent scattering of the conduction electrons, resulting in the emergence of transverse spin-current. Microscopically, depending on the relative orientation of the spin polarization, electrons scatter in a direction orthogonal to both the applied electric field and the spin-polarization vectors, where the scattering

angles are opposite for the oppositely spin-orientations.

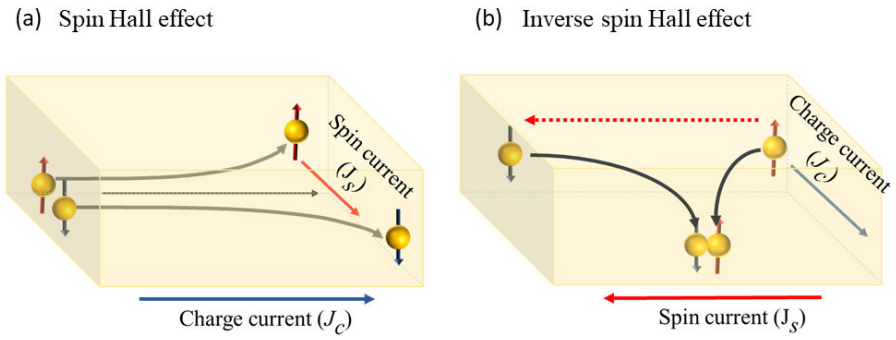

Figure 1.2: (a) depicts the spin Hall effect mechanism, where a injected charge current generates a transverse spin-current, and (b) depicts the inverse spin Hall effect, where a injected spin-current is converted into a transverse charge-current.

1.2.2.2 Inverse spin Hall effect

The inverse spin Hall effect (ISHE) is a reciprocal effect of the SHE, where a spin-current injected into a metal with sizeable spin-orbit coupling generates an electrical current orthogonal to both the spin-current and the polarization direction of the conduction electrons [42–44, 71]. Commonly, non-magnetic heavy metals, like Pt, W, or Ta, are used for the detection of a spin-current [72]. Fig.1.2(b) depicts the ISHE inside that heavy metal. Mathematically, the SHE and the ISHE can be expressed as [42]:

$$\vec{j_s} \propto \theta_{SH} \left(\frac{2e}{\hbar}\right) \vec{\sigma} \times \vec{j_c} \tag{1.8}$$

and,

$$\vec{j_c} \propto \theta_{SH} \left(\frac{2e}{\hbar}\right) \vec{\sigma} \times \vec{j_s} \tag{1.9}$$

where, θ_{SH} is the spin Hall angle of the material, $\vec{\sigma}$ is the polarization of the conduction electrons, $\vec{j_c}$ is the electrical current, and the j_s is the spin-current. The microscopic origin of SHE or ISHE is the spin-orbit interaction, which can be decomposed into three

distinct mechanisms – (I) skew scattering, (II) side jumping, and (III) Berry curvature effect [48, 63, 64].

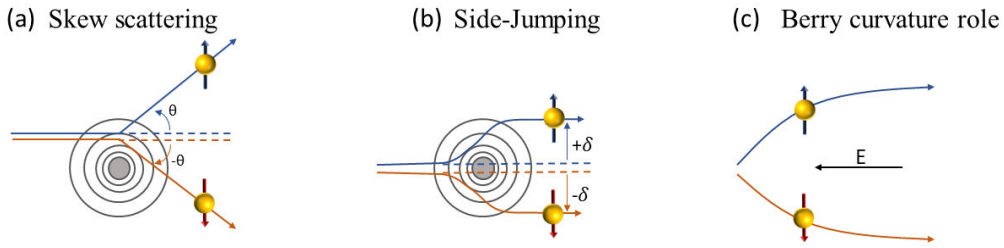

Figure 1.3: (a), (b), and (c) are showing the cartoon of skew scattering, side jumping, and Berry curvature effects, respectively.

(I) Skew scattering usually acts as an extrinsic mechanism governed by the asymmetric scatterings of the conduction electrons. Fig.1.3(a) illustrates the skew scattering mechanism. It considers the scatterings from impurities in the presence of strong spin-orbit coupling, where the scattering cross-section depends on the scattering-angle and sign of spin and orbital angular momenta [73, 74]. Thus, depending on the spin orientation of the conduction electrons, it will scatter that moving electrons into the opposite directions (either left or right) for having opposite spin polarizations, and that develops a transverse potential [73, 75]. In the case of SHE, it will generate a spin-voltage. Similarly, in the case of ISHE, it will develop an measurable electrical-voltage.

(II) Side jumping mechanism is also governed by the asymmetric scatterings of the conduction electrons from impurity potentials concerning their relative spin orientations, which results in a spin-dependent lateral shift of conduction electron packet [48, 63, 76, 77]. Fig.1.3(b) represents a schematic of the side jump mechanism. Depending on the spin orientations of the conduction electrons, the equal amount of lateral shift occurs in the opposite direction of the opposite spin polarizations – developing the transverse potential difference.

(III) Berry curvature effect is an intrinsic mechanism associated with the spin-dependent band structure of the crystalline material – which is significantly different from all aforementioned asymmetric scattering pictures. Fig.1.3(c) shows a schematic of this effect. In this intrinsic picture, due to inter-band coherence induced by an external electric field, electrons gain an anomalous velocity orthogonal to the field direction. Depending on the Berry curvature of the conduction electrons, a transverse potential difference occurs across the material system [48, 78–82].

It interesting to note that Pt, a popular candidate used as a detection layer for the spin-current, is also reported for possessing a significant Berry phase effect in determining the SHE or the ISHE [83, 84].

1.2.3 Interplay of spin-heat-charge degrees of freedom

1.2.3.1 Hall and Nernst effect

The aforementioned mechanisms, namely skew-scattering, side jump, and Berry curvature effect, certainly explain the microscopic origin of the transverse motion of electrons even in the absence of an external magnetic field – where the role of spin-orbit coupling is undeniable. Nonetheless, the motion of a conduction electron is also influenced by an external field, where the role of spin-orbit coupling is not always necessary. For instance, the Lorentz force acting on a freely moving charged particle can explain the role of an external magnetic field on the moving electrons that causes the conventional Hall or Nernst effect, illustrated in Fig. 1.4(a) and 1.4(b), respectively.

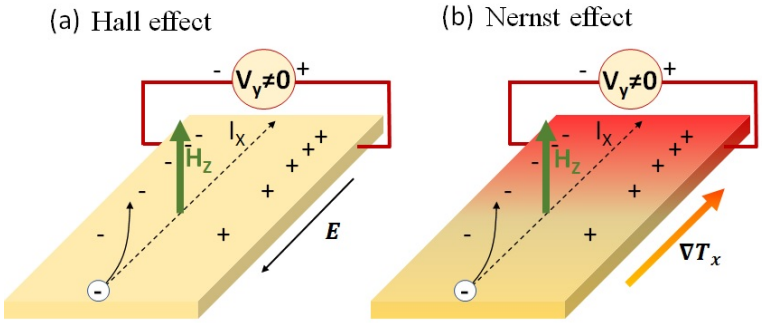

Figure 1.4: (a) and (b) depict the Hall and Nernst effects, respectively.

In the case of ordinary Hall effect, the associated Lorentz force could be written as $\vec{F} = q[\vec{E} + \vec{v} \times \vec{B}]$ where q is the charge, v is the velocity of that charge, $\vec{E}$ is the applied electric field causing the longitudinal motion, and $\vec{B}$ is the magnetic field causing the transverse motion of the charged particle [85]. The nomenclature is due to Edwin H. Hall, who first observed the role of an external magnetic field on the injected current in a non-magnetic gold leaf [86]. In the case of the ordinary Nernst effect, instead of a longitudinal electric field, the applied thermal gradient acts as a driving force. Thus, the Nernst effect is a thermal analogue of the ordinary Hall effect. Conventionally, the Hall-voltage (or Nernst-voltage) is determined by the transverse voltage (V_y), measured in a direction orthogonal to both the applied electric field (or thermal gradient) and the external magnetic field. Presently, the Hall measurement is a well-known experimental technique to determine the sign and density of the charged carriers, where Hall voltages can be expressed as

$$V_y = \frac{1}{nq}\frac{I_x}{d}B_z \tag{1.10}$$

with the carrier density n, the applied magnetic B_z along the z-direction, applied current I_x along the x-direction, and thickness of the specimen d. Fig. 1.4(a) and 1.4(b) depict the measurement-geometry for the Hall and Nernst voltages, respectively. It is important to note that Equation 1.10 is strictly valid in a single band picture. If the material

has multiple bands at the Fermi energy (E_F) contributing to the conductivity, the carrier density n has to be replaced by the effective carrier density, n_{eff} – where the analysis of the Hall effect would be more complicated [85].

1.2.3.2 Anomalous Hall and anomalous Nernst effect

In the case of a magnetic material, the Hall or the Nernst signal gain an additional contribution due to the magnetization of the specimen, which is described as the anomalous Hall effect (AHE) or the anomalous Nernst effect (ANE). Thus, fundamentally, the ANE or the AHE could be present even in the absence of any external magnetic field. Microscopically, the origin of these anomalous effects is explained in the light of skew-scattering and side jumping processes (extrinsic mechanism) as well as Berry curvature contribution (intrinsic mechanisms) [9, 10, 87, 88]. However, unlike SHE or ISHE, an asymmetry between the population of spin-up and spin-down conduction electrons is necessary for the generation of AHE or ANE. This asymmetry creates an imbalance in the scattered population of the charged carriers, which results in a net voltage in a direction orthogonal to both the applied current (in AHE) or thermal gradient (in a thermal gradient) in ANE) and the magnetization. Thus, the geometry of the device is important for the measurement of those signals. Conventionally, a mutually orthogonal geometry of the device is preferred – where, the voltage detection axis, the thermal gradient (during measurements of ANE) or the applied current direction (during measurements of AHE), and the applied external Magnetic field (or the direction of the $\vec{M}$) are kept mutually orthogonal to each other. Fig. 1.5(a) and 1.5(b) illustrate the measurement geometry for the AHE and the ANE, respectively. Fig. 1.5(c) and 1.5(d) illustrate the SHE and the SNE in comparison with other effects, such as ANE or AHE.

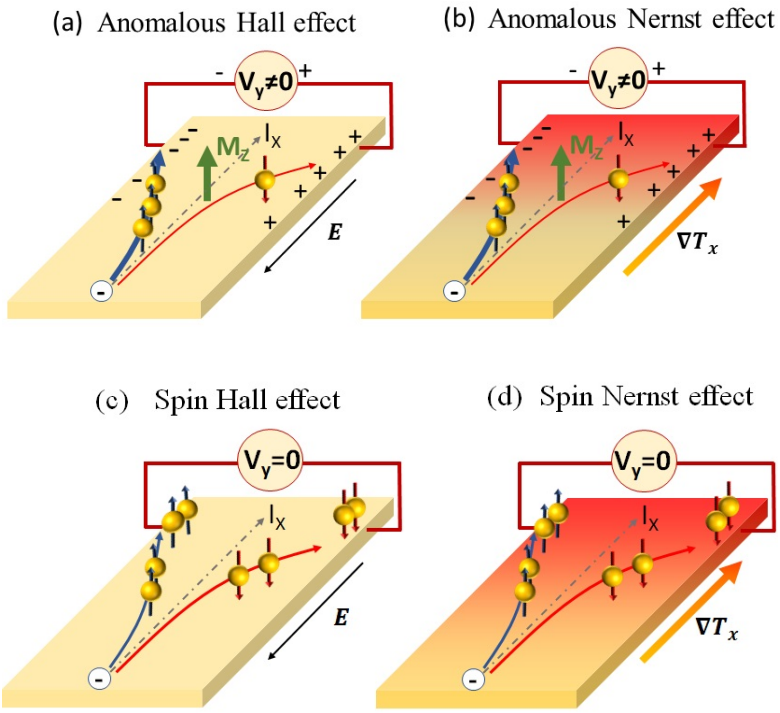

Figure 1.5: (a) and (b) depict the anomalous Hall and anomalous Nernst effects, respectively. In contrast, (c) and (d) depict the spin Hall and spin Nernst effects, respectively.

A macroscopic empirical formula of the AHE or the ANE can be expressed as:

$$v_y \propto \vec{M} \times \vec{\tau} \tag{1.11}$$

Here, v_y is the transverse voltage generated by AHE or ANE, $\vec{M}$ is the magnetization of the material, and $\vec{\tau}$ is the driving force for the longitudinal motion of the electrons. In particular, $\vec{\tau}$ represents either the applied thermal gradient ($\vec{\nabla}T$) or the electric field ($\vec{E}$) to describe the ANE or the AHE, respectively. Mott's relations of the transport conductivities explains one of the main difference between the AHE and the ANE. Fundamentally, it relates thermal and electrical conductivities. According to the Mott's relations, the anomalous Nernst coefficient (α_{xy}) can be expressed in terms of anomalous Hall

coefficient (σ_{xy}), such that [9]:

$$\alpha_{xy} = \frac{\pi^2 k_B^2 T}{3e} \cdot \left(\frac{\partial \sigma_{xy}}{\partial E} \right)_{E_F} \tag{1.12}$$

where, k_B, T, e, E, and E_F are the Boltzmann constant, temperature of the sample, charge of an electron, the energy of the conducting electrons, and the Fermi energy of the specimen, respectively. Equation 1.12 suggests that α_{xy} is more sensitive to the changes in the Fermi surface [89].

1.2.3.3 Planar Hall and planar Nernst effect

The Planar Hall effect, as well as planar Nernst effect (PNE), are also spin-orbit couplings driven asymmetric scattering phenomenon, whose origin is quite similar to that of the AHE (or the ANE) [90, 91]. Conventionally, the PNE is determined by the in-plane voltage measured along the transverse direction of the applied in-plane thermal gradient across a magnetic material, whose magnetization also belongs to the same plane of the thermal gradient [92–94]. Fig. 1.6 (b) shows the schematics of the measurement geometry of the PNE − where the applied thermal gradient ($\vec{\nabla} T$) is along the x-direction, the magnetization ($\vec{M}$) is at an angle θ with the $\vec{\nabla} T$ in the xy-plane, and the PNE voltage (V_{PNE}) is measured along the y-direction.

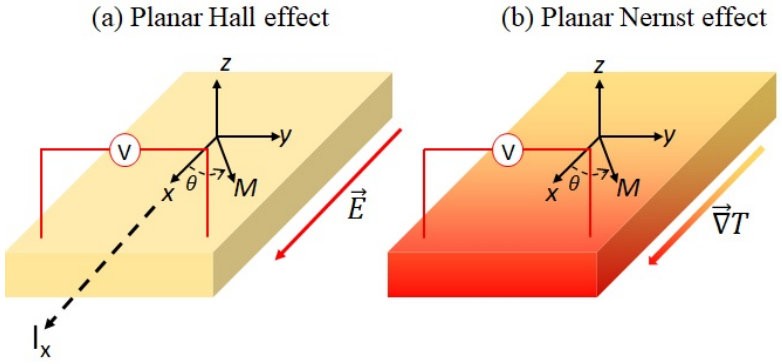

Figure 1.6: (a) and (b) depicts the planar Hall effect and planar Nernst effect, respectively. In both cases, the magnetization ($\vec{M}$) lies in the same plane as the thermal gradient, $\vec{\nabla}T$

Macroscopically, V_{PNE} can be expressed as [95]:

$$V_{PNE} \propto | \vec{M} \times (\vec{M} \times \vec{\nabla}T) | \propto | M |^2 \nabla T sin(2\theta) \tag{1.13}$$

The measurement geometry of the PHE is similar to that of the PNE, shown in Fig. 1.6(a), where the only difference is that the $\vec{\nabla}T$ has to be replaced by the applied electric field. Unlike the anomalous Hall or Nernst signals, both the planar Hall or Nernst signals are measured in the in-plane geometry – which makes a significant impact in the nature of observed signals.

1.2.4 Generation and detection of magnonic spin-current

The interplay of spin and charge degrees of freedom has paved the way for modern spintronic devices and technologies through various magneto-resistive effects, like, GMR, TMR, etc. The functionality of those devices is governed by manipulating spin-charge interaction, which helps to control the motion of conducting electrons. However, such control is also limited by the spin-flip scattering mechanisms. A promising alternative could be the use of spin-current, which can replace all the charge-current-based logic

gates by the spin-current-based logic gates for much faster processing speed with much lower heat dissipation. Today, many research activities are focused on generating, detecting, and characterizing the spin-current inside various material systems.

1.2.4.1 Microwave excitation

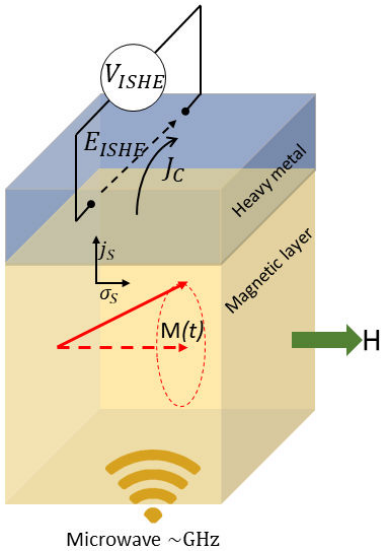

Figure 1.7: represents a cartoon for the microwave spin-pumping mechanism. The dynamics of the magnetization near to the interface is responsible for net spin-pumping.

The generation of spin-wave inside magnetic materials under application of microwave is known as ferromagnetic resonance or FMR technique, where the response of magnetic moments to an external magnetic excitation such as a weak alternating field in the microwave range (few GHz) is mainly responsible for the generation of spin-current [96, 97]. A schematic of this technique is depicted in Fig. 1.7. A thin non-magnetic heavy metal (HM) with a large spin Hall angle, coated on top of the magnetic material, plays an important role in detecting the pumped spin-current detection [72]. Microscopically, the net spin-current pumped through the interface is further converted into a transverse electric field by the ISHE in the HM layer [42].

1.2.4.2 Spin Seebeck effect (SSE)

The conventional Seebeck effect is known for the generation of an electrical current across a material under the application of a thermal gradient. In a similar analogy, the spin Seebeck effect (SSE) describes the generation of a thermally induced magnonic spin current inside a magnetic material under the application of an external temperature gradient ($\vec{\nabla}T$) [1–3, 7, 71, 98]. In order to detect that spin-current, a NM layer with a large spin-orbit coupling (typically Pt) is deposited on top of that magnetic material. As a result, a certain amount of the generated spin-current, propagating towards the interface, enters into the NM-layer due to thermal spin-pumping. Finally, this pumped spin-current is converted into a transverse electric-field by the ISHE at this NM-layer. The first experimental demonstration of SSE was reported in 2008 by K. Uchida and co-workers, where they used a thin film (20 nm) of ferromagnetic metal $Fe_{81}Fe_{19}$ to generate the spin-current and a Pt strip (10 nm) on top as a spin detector [1]. Initially, the SSE was explained in the light of conduction electrons driven spin-current model [1]; however, two years later, similar observations on magnetic semiconductors [3] and insulators [2] established the profound nature of spin-wave driven spin-currents. Nowadays, magnons are considered as the primary carrier of the pure spin-current owing to their considerable propagation length, as well as the fact that they are not associated with the flow of electric charges.

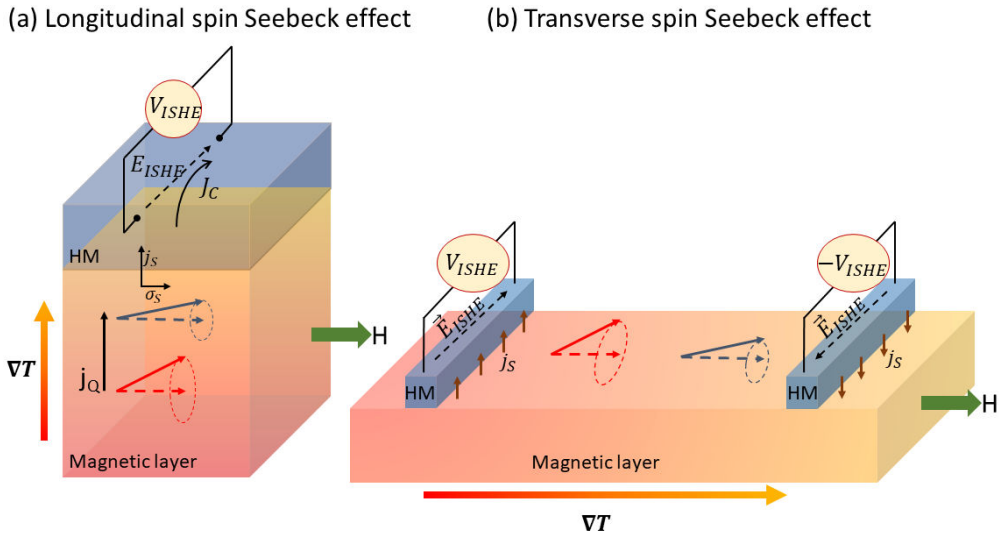

Figure 1.8: (a) depicts the longitudinal spin Seebeck effect (LSSE) where the applied $\vec{\nabla}T$ is parallel to the pumped spin-current direction ($\vec{j_s}$). (b) shows the transverse spin Seebeck effect (TSSE), where $\vec{\nabla}T$ and $\vec{j_s}$ are orthogonal to each other.

Prior measurements of SSE were performed in two different types of device geometry, called the longitudinal mode of SSE and the transverse mode of SSE [6, 60–62]. The schematics of these devices are shown in Fig. 1.8 (a) and (b). The first one depicted in Fig. 1.8 (a), is the longitudinal mode, where the pumped spin-current is parallel to the applied thermal gradient direction. Whereas, Fig. 1.8 (b) depicts the transverse mode, in which the pumped spin current is orthogonal to the applied thermal gradient. Presently, the longitudinal mode is widely used for the detection of spin currents because of the fact that the total signal in the transverse mode is also partially contributed by a parasitic effect of longitudinal spin Seebeck effect (LSSE) owing to the incidental out-of-plane thermal gradient. Such role of parasitic cross-effects in the transverse mode is confirmed in a recent experiment, reported by D. Meier and co-workers published in 2015 [6]. In this thesis, the presented SSE signals are measured in the longitudinal mode, and details are discussed in Chapter 3.

1.2.5 Interfacial spin pumping

Interfacial spin pumping is an important function that determines the effective transfer of spin angular momentum into the detection layer. In other words, it decides the net spin-current in the NM layer. The essential ingredient of spin-pumping is the interaction between spins of itinerant electrons in an NM-layer and the localized moments in the magnetic layer, and such interaction is usually quantified by a parameter called the spin mixing conductance ($g_{\uparrow\downarrow}$) [97, 99–101]. The total $g_{\uparrow\downarrow} = g_r + ig_i$, where g_r is the real part, and g_i is the imaginary part of the spin mixing conductance. Ideally, g_r is related to the effective spin current that is pumped through the interface, and g_i represents the loss at the interface. Mathematically, the amount of spin-current pumped from the ferromagnet to the NM is described in terms of the thermally activated magnetization dynamics at the interface, and could be expressed as [7, 62]:

$$\vec{j}_{sp} = \frac{\hbar}{4\pi}\left(g_r\vec{M}(t) \times \dot{\vec{M}}(t) + g_i\dot{\vec{M}}(t)\right) \tag{1.14}$$

where the magnetization dynamics is modelled in terms of Landau-Lifshitz-Gilbert (LLG) equation. The LLG equation is given by [7, 62]

$$\dot{\vec{M}}(t) = -\gamma\vec{M}(r,t) \times [\vec{H}_{eff}(r) + \vec{h}(r,t)] + \alpha\vec{M}(r,t) \times \dot{\vec{M}}(t) \tag{1.15}$$

where, γ is the gyromagnetic ratio, H_{eff} is the total magnetic field that is responsible for the precessional motion of the magnetization, h is random fluctuating field due to thermal energy and various damping factors near to the magnetic moment, and α is the total magnetic damping factor. Apart from $\vec{j}_{sp}$, there is another spin current flowing in the opposite direction called the spin back-flow ($\vec{j}_{sb}$), which is caused by the thermal

noise in NM. The effect of that thermal noise in NM on the magnetic layer can be described by a random magnetic field (h') acting on the magnetization and results in $\vec{j}_{sb}$. In mathematical language it is expressed as [7, 62]:

$$\vec{j}_{sb} = -\frac{M_s V}{\gamma}\gamma\vec{m}(t) \times \vec{h}'(t) \tag{1.16}$$

where, M_s is the saturation magnetization, V is the volume of that ferromagnetic specimen, $\vec{m}$ is the unit vector parallel to the magnetization. The negative sign in the Equation 1.16 represents the spin back-flow. Thus the effective spin current pumped through the interface is given by the statistical average [7]:

$$\vec{j}_s = \langle\vec{j}_{sp}\rangle + \langle\vec{j}_{sb}\rangle = \frac{M_s V}{\gamma}\left[\alpha' \langle\vec{m} \times \dot{\vec{m}}\rangle - \gamma \langle\vec{m} \times \vec{h}'\rangle\right] \tag{1.17}$$

where $\alpha' = \left(\frac{\gamma\hbar}{4\pi M_s V}\right) g_r$ is the magnetization damping contribution due to spin pumping. It is important to note that the contribution of the imaginary part in Equation 1.14 does not contribute to the effective pumped spin current due to the fact that $\langle\dot{\vec{m}}\rangle = 0$.

The aforementioned expression is more or less a macro-spin model, and this work was further extended by J. Xaio and co-workers where they considered a simple ferromagnet/NM bilayer system and magnon excitation of all wave vectors. After taking the statistical average, the macroscopic mathematical formulation of the z-component spin-current (actual pumped spin-current into the NM layer) is expressed as [7]:

$$\langle j_s\rangle_z \approx \frac{\gamma\hbar K_B}{2\pi M_s V_a}\frac{g_r}{A}(T_F - T_N) \tag{1.18}$$

where, k_B is the Boltzmann constant, A is a constant associated to the interface, T_F is effective temperature of the magnon near to the interface, T_N is the effective temperature

of the electrons of the NM layer near to the interface. The important factor is that now the total magnetic volume (V) is replaced by the magnetic coherence volume fraction V_a, i.e. $V \rightarrow V_a$. Thus, apart from the M_s, V_a also contributes to the temperature dependence of the j_s. The functional form of V_a is given by [7]:

$$V_a = \frac{2}{3\zeta(\frac{5}{2})}\left(\frac{4\pi D}{K_B T}\right)^{\frac{3}{2}} \tag{1.19}$$

where, D is the spin-stiffness of the ferromagnet, T is the average temperature of the magnetic specimen.

Detection of spin current is executed by converting this $\langle j_s \rangle_z$ into an electrical voltage via ISHE. In particular, Equation 1.18 suggests that a thermal gradient (∇T) applied across the interface provides a non-equilibrium thermodynamic environment such that $T_F \neq T_N$, which results in a net spin-current flowing through the interface. S M Rezende and co-workers first provided a mathematical description for the inverse spin Hall voltage (V_{LSSE}) associated with the longitudinally pumped spin-current $\langle j_s \rangle_z$. According to this, V_{LSSE} is given by [8, 43, 102]:

$$V_{LSSE} = R_N w \lambda_N \frac{2e}{\hbar}\theta_{SH}\left[tanh\left(\frac{t_N}{2\lambda_N}\right)\right]\langle j_s \rangle_z \tag{1.20}$$

where, R_N is the resistance between the voltage probes on the NM-layer, w and t_N are the width and thickness of the NM-layer respectively, θ_{SH} is spin Hall angle of the NM-material, and λ_N is the spin diffusion length in the NM-layer. The fact that the sign of the $\langle j_s \rangle_z$ is reversed by either reversing the magnetization direction (M_s) or reversing the thermal gradient(∇T), also results in reversing the polarity of the detected V_{LSSE}. Furthermore, the V_{LSSE} also reversed its polarity by reversing the sign of θ_{SH} of the NM-layer. Thus, the LSSE signal is confirmed by studying transverse voltage, V_{LSSE}

as a function of applied magnetic filed, thermal gradient, and NM-layers with opposite θ_{SH}.

1.2.6 Detection of LSSE in a magnetic-metal/Pt system

Since both the LSSE and the ANE are an anti-symmetric function of the control parameters, like, $\vec{\nabla}T$ and applied magnetic field ($\vec{H}$), the investigation of LSSE-signals in a magnetic metal (MM) is hampered by an incidental ANE-signal in the magnetic subunit. On top, since Pt is near the Stoner ferromagnetic instability, the utilization of Pt as a spin-to-charge conversion layer could be associated with the proximity induced magnetism in the vicinity of the interface, which could also trigger an addition ANE signal. Thus, the investigation of LSSE in MM/Pt system is plagued by the contaminated LSSE-signals, where the parasitic signals emerge as a result of ANE in the magnetic subunit as well as the proximity induced ANE in the Pt-layer [103]. It is worth mentioning that these ANE-signals – by virtue of measurement geometry – contribute additively to the LSSE-signal. Thus, the disentanglement of ANE's parasitic effects from the spin Seebeck signal is clearly imperative for an accurate description of the LSSE. In prior experiments, such disentanglement was performed by inserting a spacer layer in-between the magnetic layer and the detection layer [104–106]. However, such insertion of a spacer layer may attenuate the original LSSE signal [107, 108]. Recently, without the utilization of a spacer layer, a quantitative disentanglement of the SSE from these spurious ANE contributions was reported [103]. Using a set of Pt-$NiFe_2O_x$/$Ni_{33}Fe_{67}$ bilayers (with sample resistances varying across seven decades) and utilizing in-plane and out-of-plane measurement geometries, it was demonstrated that the proximity-induced ANE was a contributory factor only in the most metallic specimens whose resistivity (ρ) remains in the order of 10^{-7} Ω-m [103]. Whereas, the

proximity induced Nernst effect was showed to be negligibly small in magnetic system with $\rho \geq 10^{-5}$ Ω-m [103]. This also explains why the prior reports on the investigation of LSSE in the magnetic insulator(MI)/Pt systems observed no ANE contamination in the LSSE component [109, 110]. Thus, in the case of MM, whose resistivity is typically in the order of 10^{-5} Ω-m or larger, the aforementioned disentanglement could be done just by estimating both the conventional ANE in the bare magnetic layer and the total signal in that ferromagnet/Pt device – where the proximity induced ANE could be ignored. Fig. 1.9(a) and 1.9(b) depict the device geometry for the measurements of ANE and total signals (ANE + LSSE), respectively.

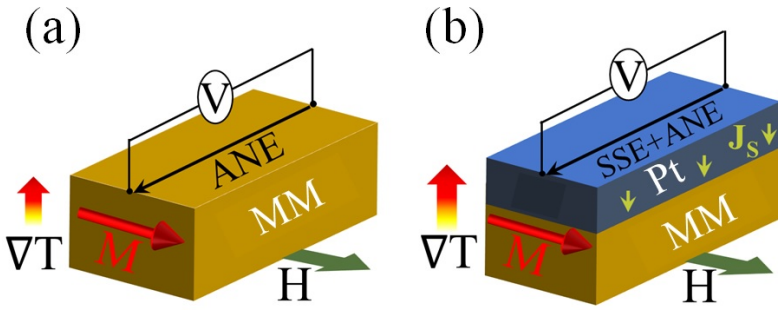

Figure 1.9: (a) depicts the measurement geometry of ANE in the bare magnetic layer. (b) depicts the measurement geometry of the total signal (ANE+LSSE) by utilizing Pt as the detection layer.

Since the ANE and the total signal appears against different effective resistances, the LSSE component in the MDM could be approximated as

$$V_{LSSE} \approx \frac{V_{total}}{\nabla T * R_{total}} - \frac{V_{ANE}}{\nabla T * R_{ANE}} \tag{1.21}$$

where, V_{total}, R_{total}, V_{ANE}, R_{ANE}, and ∇T are the measured total voltage in the MDM/Pt

device, the effecttive resistance across which the V_{total} is appeared, the measured ANE-voltage in the bare MDM layer, the corresponding resistance across which the ANE-voltage is appeared, and the applied thermal gradient, respectively. Here we consider that the geometrical dimension of both devices (depicted in Fig. 1.9 (a) and 1.9 (b)) are kept identical. Otherwise, the measured signals also need to be normalized by a factor, $\frac{l_y}{l_z}$, where l_z is the thickness of the MDM-layer, and l_y is the distance between the voltage probes. Besides the ∇T, the applied magnetic field (H) is also considered to be similar in both measurements.

1.2.7 Magnon Hall effect

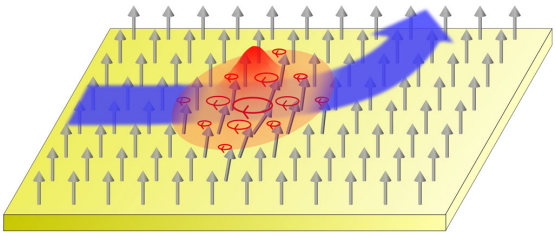

Figure 1.10: depicts the schematics of MHE, where the transverse magnon flow results in transverse thermal gradient [12]. The figure is adapted from Ref.[12] with permission from AAAS.

The generation of magnon current is a well-described phenomenon in the context of SSE or microwave-excitations. A fundamental question for the magnon current is whether it exhibits the Hall effect. In this context, the magnon Hall effect (MHE) describes how the magnons, even though they are charged neutral, exhibit Hall transport. Fig. 1.10 depicts a schematic of the MHE. In 2010, H. Katsura et al. first introduced a theoretical prediction of MHE in terms of the thermal Hall effect of magnons (THEM),

where they calculated the transverse thermal conductivity (K_{xy}) by using the Kubo formula and showed that the K_{xy} emerged due to the Berry curvature in k-space, associated with the magnon wave-functions [111]. First experimental demonstration was performed by Y. Onose and co-workers, where the THEM was measured in a pyrochlore single crystal of $Lu_2V_2O_7$ specimen [12]. Till date, the MHE was studied in the thermal Hall geometry, where the magnetic field dependence of the transverse thermal conductivity (K_{xy}) was measured in a direction orthogonal to both the applied thermal gradient and magnetic field [15, 111]. Crystals, like $Lu_2V_2O_7$, $Ho_2V_2O_7$, and $In_2Mn_2O_7$, have been explored in this fashion [15]. Apart from the transverse heat current measurements (or the transverse thermal gradient measurements), inelastic neutron scattering experiments carried out in the $Lu_2V_2O_7$ sample also confirmed the notion of MHE [112]. In this thesis, we have investigated the THEM in signal crystalline $Y_2V_2O_7$ specimen, detailed in Chapter 5.

1.3 Scope of this thesis

This thesis aims to explore various thermal aspects of spintronics, which could be classified in the sub-set of Spin-caloritronics. In particular, three distinct phenomena are investigated: (*i*) the spin Seebeck effect (SSE), (*ii*) the anomalous Nernst effect (ANE), and (*iii*) magnon Hall effect (MHE). We began with building up the measurement-unit for the investigations of different kinds of spin-Caloritronic phenomena. The details of the instrumentation and other experimental tools are discussed in chapter 2. This apparatus was then used for investigation of a number of spin caloritronic phenomena. In particular, this thesis presents:

(*I*) Temperature dependence of the LSSE in the $La_{0.7}Ca_{0.3}MnO_3$/Pt bilayer system

is presented, where the observed LSSE signal exhibits a $T^{0.5}$ dependence in the low-temperature regime, which matches well with that predicted by the magnon-driven spin current model. Across the double exchange driven para-ferromagnetic transition, the LSSE exponent is significantly higher than the magnetization one, and also depends on the thickness of the spin-to-charge conversion layer. These observations highlight the importance of individually ascertaining the temperature evolution of different mechanisms – especially the spin mixing conductance – which contributes to the measured spin Seebeck signal.

(*II*) A detailed study of the temperature dependence of ANE in an off-stoichiometric $Ni_{1.96}Mn_{1.04}Ga$ (NMG) is presented for the first time in this Ni-Mn-Ga class of materials, where the ANE shows a substantial sensitivity across the premartensitic phase transition (PMT) of this sample, in contrast to other transport as well as the magnetization measurements. A possible coupling between the Fermi surface and the magnetism in this premartensitic phase of the sample is also suggested from the anomalous Nernst characteristics.

(*III*) A detailed investigation on the THEM in single-crystalline $Y_2V_2O_7$ specimens, where the measurements are performed in two different crystals whose planes are cut and polished into two different orientations, like, {100} and {111}. Unlike the previous experimental detection method [12, 15], we measure the transverse thermal gradient (∇T_{zx}) by putting a thin non-magnetic normal metal (NM), like, Pt, or W, on top of the crystal's plane. The THEM is then quantified in terms of thermo-power, generated along the length of the NM-bar (also called as the detection layer). In contrast to the prior reports, where the ∇T_{zx} was directly measured by utilizing thermocouples [12, 15], our method significantly improves

the signal to noise ratio. An observation confirms that a significant amount of the THEM-signal in this $Y_2V_2O_7$ specimen is contributed by the magnons of higher energy bands. Additionally, the crystal with {111} planes is observed to display a significant magnon drag effect at the interface with the NM layer – which is further linked to the topologically protected chiral surface state of magnons.

Chapter 2

Instrumentations and experimental techniques

This chapter provides a brief description of the sample fabrication, characterization, and spin-caloritronics measurement techniques. All the measurements to study the spin-caloritronic phenomena are performed in a home-made set-up. The chapter is written in two main sections. The first section contains the details of instrumentation along with the measurement-protocols and the limitations of our instrument. The second section covers all other experimental techniques used for the fabrication of devices as well as its characterization via X-ray diffraction, magnetic, and electrical transport measurements.

2.1 Instrumentation & spin-caloritronic measurements

We have designed and developed a home made apparatus for sensitive measurements of the spin Seebeck effect (SSE), the anomalous Nernst effect (ANE), and the magnon Hall effect (MHE). The set-up comprises of a closed cycle refrigerator (CCR), a temperature controller, a nano-voltmeter, a source meter, and an electromagnet with an upper field limit of 2 kOe. The temperature gradient across the sample and also the average

temperature of the sample is controlled by two PID controlled heaters and the temperature is measured by two temperature sensors attached near the sample edge. The geometry of the holder is such that the applied thermal gradient is always orthogonal to the rotation plane of the magnetic field. The whole set-up is put inside a Faraday cage for reducing the noise, and signals as low as ten nV can be reliably measured. The details of the set-up are described in the following sub-sections.

2.1.1 Accessing low temperatures

Since the spintronic signals are strongly correlated to the magnetic and electronic state of the material, these voltages are measured with respect to the sample temperature, applied electric, and magnetic field. Thus, accessing low temperatures is one of the crucial parts of the instrumentation, in which the samples are commonly cooled down by using a cryo-liquid to perform low-temperature experiments. Generally, liquid Nitrogen (N_2) or Helium (H_2) is used as a cryo-liquid. A dewar flask, which is a specialized type of vacuum flask, is commonly used to store the cryo-liquid. In specifically, a dewar-flask is a double side-wall glass container with a certain vacuum in-between the walls, which keeps the cryo-liquid thermally isolated from the outside environments. Moreover, a light-reflecting coating is also employed on the glass-walls to stop heating through radiations. Thus, it significantly takes care of the thermal-isolation by prohibiting heat conduction, convection, and radiation from the surrounding to the cryo-liquid.

As another alternative, a CCR provides cryogenic temperatures without the use of cryo-liquid, and also requires minor maintenance [113]. The basic working principle of a CCR is based on the thermodynamic refrigeration cycle through a periodic expansion and compression of gas (e.g., Gifford McMahon (GM) cycle [114]). The major components of a CCR are the refrigerator, compressor, Helium hoses, and vacuum shroud.

Figure 2.1 shows all the components of a CCR. At the refrigerator, the GM-cycle takes place in which Helium gas is used to run the cycle. Two flexible helium hoses are used to supply high-pressure Helium gas from the compressor to the refrigerator through the supply line, and low-pressure Helium gas returns from the refrigerator to the compressor through the return line. Technically, the compressor provides the necessary Helium gas flow rate at the high and low pressure for the refrigerator to convert into the desired refrigeration capacity. Cold-water is also circulated to maintain the temperature inside the compressor. The low temperature is accessed from the cold end of the refrigerator, also called cold-head. A compatible sample holder is further attached to the cold-head for mounting samples. A vacuum shroud is used to keep both the cold-head and the sample holder under vacuum to achieve significant thermal isolation from the outside environments.

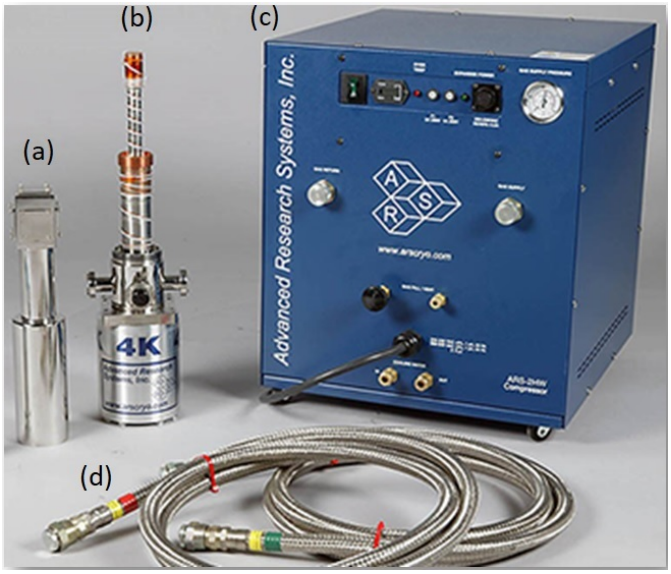

Figure 2.1: (a) vacuum shroud, (b) refrigerator, (c) compressor, and (d) Helium hoses are depicted.

We have used a CCR from Advanced Research System (ARS) with model number: DE-202. The lowest achievable temperature of the cold-head without attaching the

sample holder is 7K. However, with the sample holder, it goes up to 10K due to the addition of thermal mass of the sample holder. A strip heater is attached at the cold-head to control the base temperature, while the temperature at the cold-head is measured by a Cernox sensor. Both the sensor and the heater are connected to the temperature-controller for stabilizing the temperature of the cold-head.

2.1.2 Designing sample holder

A compatible sample holder, mounted at the bottom of the cold-head of the CCR, has been designed for all kinds of longitudinal spin-caloritronic measurements. The sample is mounted at the sample holder by sandwiching in-between two Copper blocks. Apart from the strip heater mounted at the cold head, two cartridge heaters are also attached at the sample holder to control the thermal gradient across the sample ($\vec{\nabla}T$) as well as the average temperature of the sample (T_{av}). Technically, the sample temperature is maintained by two-stage heating. The strip heater first maintains the base temperature, and then the cartridge heaters are operated on top of this base-temperature to maintain both the $|\nabla T|$ and the T_{av}. It worth mentioning that there are two more Cernox temperature sensors used at the sample holder for measuring the temperatures across the sample. The operational temperature-range in our set-up is $12K \leq T_{av} \leq 315K$, where the maximum limit of the applicable thermal gradient across the sample is 15K. A LakeShore-340 temperature controller is used to maintain both the sample average temperature as well as the thermal gradient across the sample. The geometry of the sample holder ensures that the thermal gradient is always directed along the $\pm z$-direction. Since the heat flow in a CCR mainly occurs through the conduction process, Apiezon-N grease is used between the cold-head of the CCR and the sample holder for better thermal contact. For the electrical isolation, and good thermal conduction between

the sample and the holder, the front surface of the Copper blocks are covered by using sapphire plates. The temperature sensors are attached to the top of these sapphire plates.

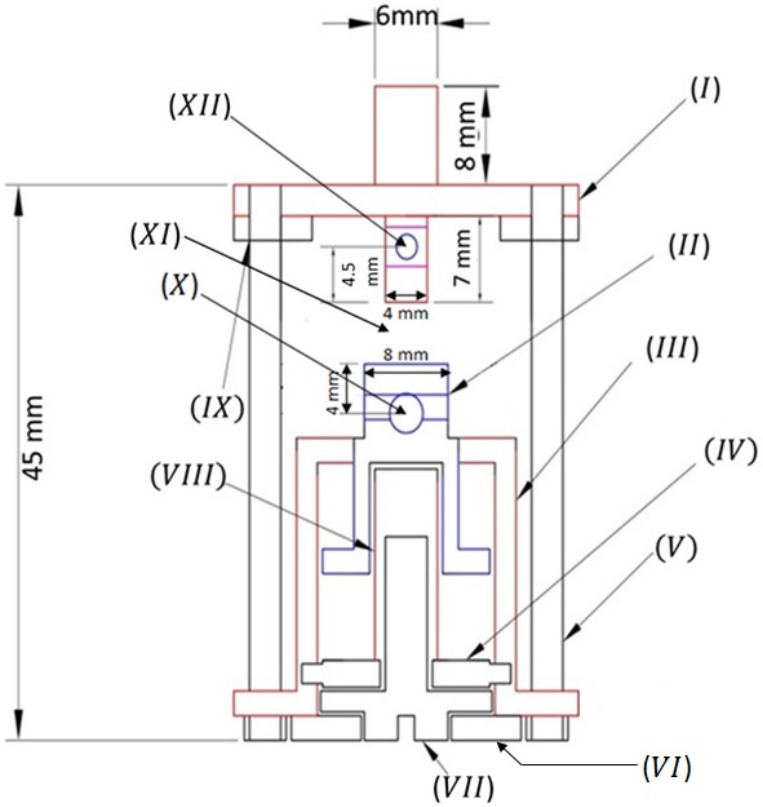

Figure 2.2: depicts a sketching of the sample holder.

Fig.2.2 shows the sketch of the sample holder. The dimensions of each part is also mentioned in the sketch. The different parts of that holder, marked in Roman letters, are described below:

- (I) represents the upper Copper block, which is directly attached to the cold-head of the CCR.
- (II) represents the lower Copper block, which is necessary for mounting the sample, and it also helps in applying the thermal gradient across the sample.

- (III) is a hollow Brass cylinder that holds the lower cooper block. It helps in minimizing the vibration by proving supports to the Copper block, and thus reduces noise during measurements.

- (IV) represents a threaded ring, kept inside the Brass cylinder, which helps in pushing the lower Copper block while sandwiching the sample.

- (V) represents a long threaded Copper screw that helps in attaching all the lower assembly of the sample holder with the upper Copper block along with the CCR cold-head. There is a total of three such screws used in the holder.

- (VI & VII) depict the Brass screw and the Brass disk, respectively. This assembly facilitates for the movement of the lower Copper block in tightening the sample in-between the blocks.

- (VIII) represents a spring used for minimizing the vibration during measurements, and it also helps in better thermal anchoring between the sample and the Copper blocks.

- (IX) is the PCB attachments with the pin-connectors, required for electrical connections to the voltage measurement leads.

- (X & XII) depict the through-holes at lower and upper Coper blocks, respectively. It is made to place the cartridge heaters.

- (XI) is showing the sample space, where the sample is sandwiched between the Copper blocks.

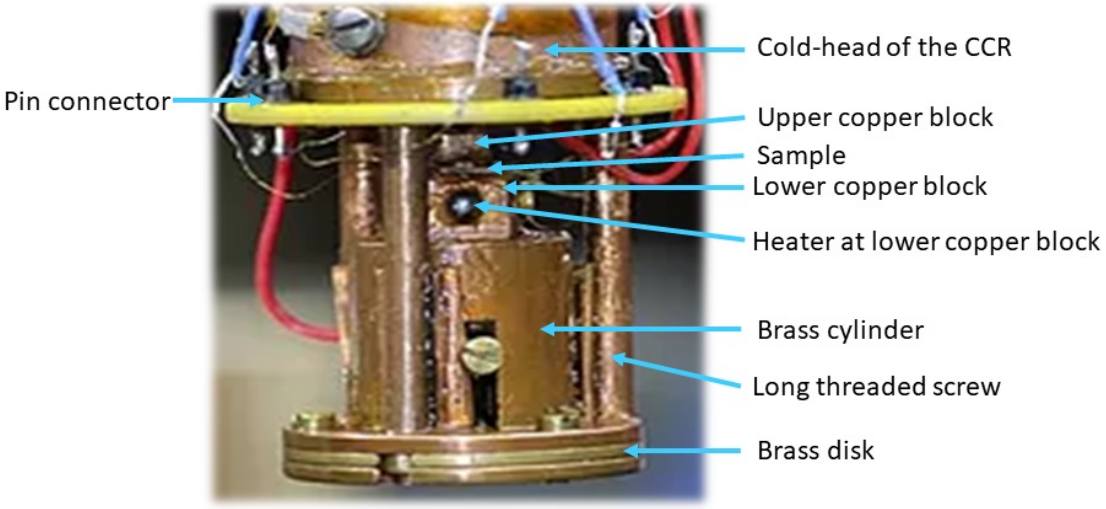

Figure 2.3: depicts a picture of the sample holder, attached at the cold-head of the CCR.

A picture of the mounted sample holder is presented in Fig.2.3. The total weight of the holder is 82 gm, which is an important factor in determining the lowest achievable temperature from the CCR.

2.1.3 Designing the CCR mounting frame, and the set-up

After mounting the sample in the sample-holder attached at the CCR cold-head, it is covered by the vacuum shroud to keep the inner assembly under the vacuum. A vacuum pressure of the order of 10^{-3} millibar is usually achieved before switching on the CCR compressor for cooling. A rotary pump connected to the vacuum shroud is used to create the desired vacuum.

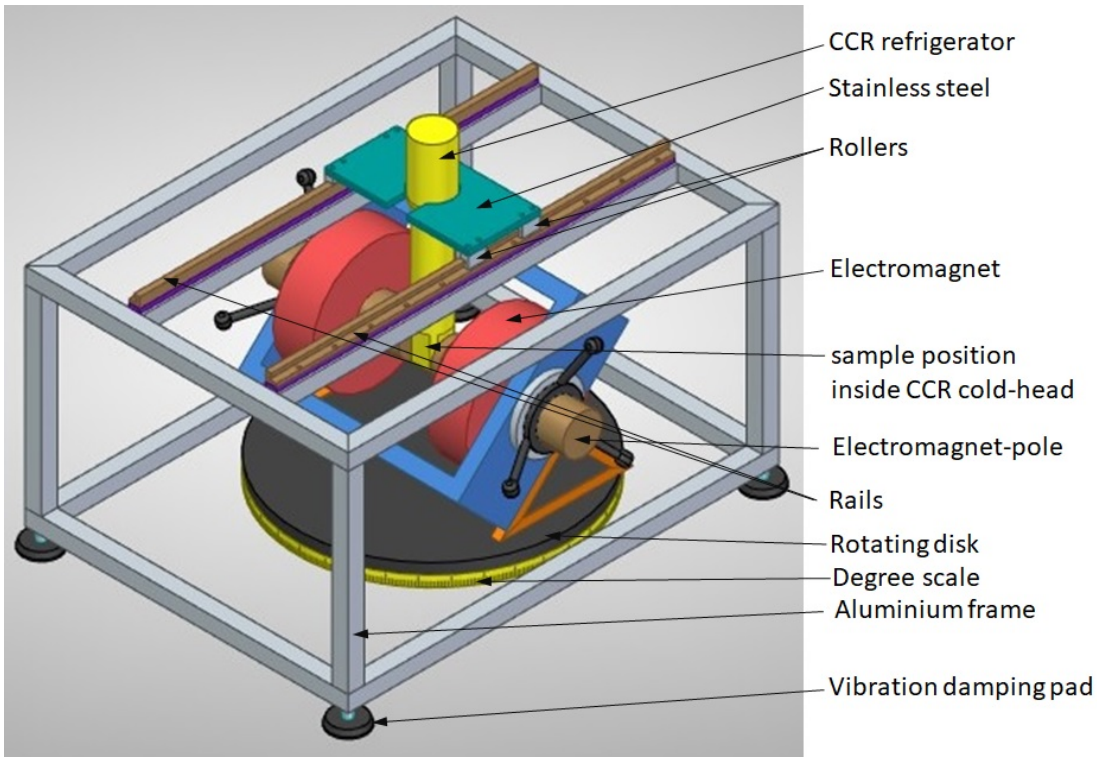

Figure 2.4: It shows the sketch of the set-up. Here, the CCR is mounted on the roller and rail assembly so that the sample can be taken in between the poles of the electromagnet, and brought back to unload the sample. The utilization of vibration damping pads, attached to the CCR mounting frame, is also depicted. These help in reducing the noise in the measured signals.

The next requirement is to put the whole assembly inside an electromagnet (EM) to access the external magnetic field, as required for the proposed measurements. For this purpose, an Aluminium frame with two parallel rails was designed. A diagram of the CCR-holding frame is depicted in Fig.2.4. The CCR, held by a stainless steel plate (SS-plate), was placed on top of the rails to transport the whole assembly into the EM so that the sample could be moved in-between the poles of the EM. Again, to take out the sample, the assembly could be moved out from the EM to open the vacuum shroud for unloading the sample. All the legs of the frame have a height-adjustable screw along with the vibration damping pads. The electromagnet was mounted on a rotating disk,

and thus the magnetic field could be rotated at any arbitrary angle in the xy-plane. However, the direction of the applied magnetic field always stays orthogonal to the thermal gradient across the sample. The spin-caloritronic signals are measured by using a nano-voltmeter (Keithley-2082A). The power supply for the electromagnet was brought from Delta Elektronika (SM 70-ar-24). The maximum applicable DC-current to the electromagnet is 15 Amps, and the maximum available magnetic field at the sample position is 2000 Oe. A picture of the set-up is shown in Fig.2.5.

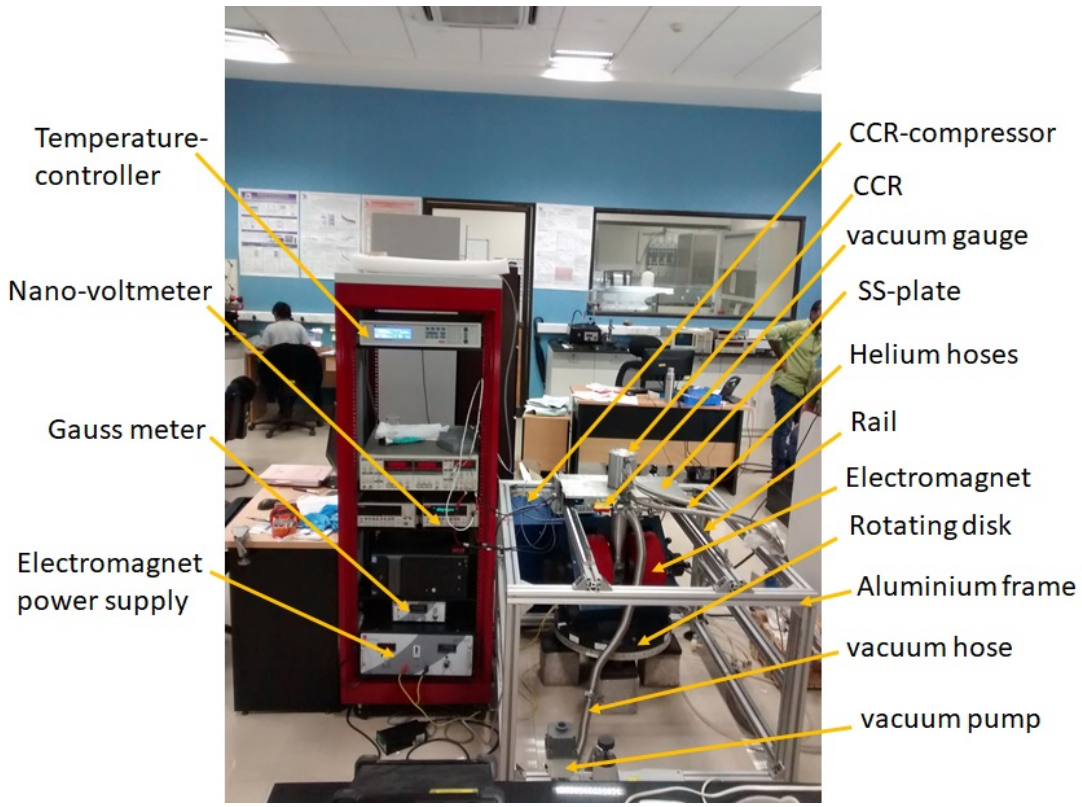

Figure 2.5: It shows a picture of the whole set-up before it is covered by the Faraday cage. The rack, kept at the side of the CCR mounting frame, contains all the electronics components, except the nano-voltmeter. The body of this metallic rack is also grounded along with the CCR-body.

A close view of the roller and rails assembly is depicted in Fig.2.6. The utilization of vibration damping pads is shown here. Such pads helps to reduce the noise in the

measured signals.

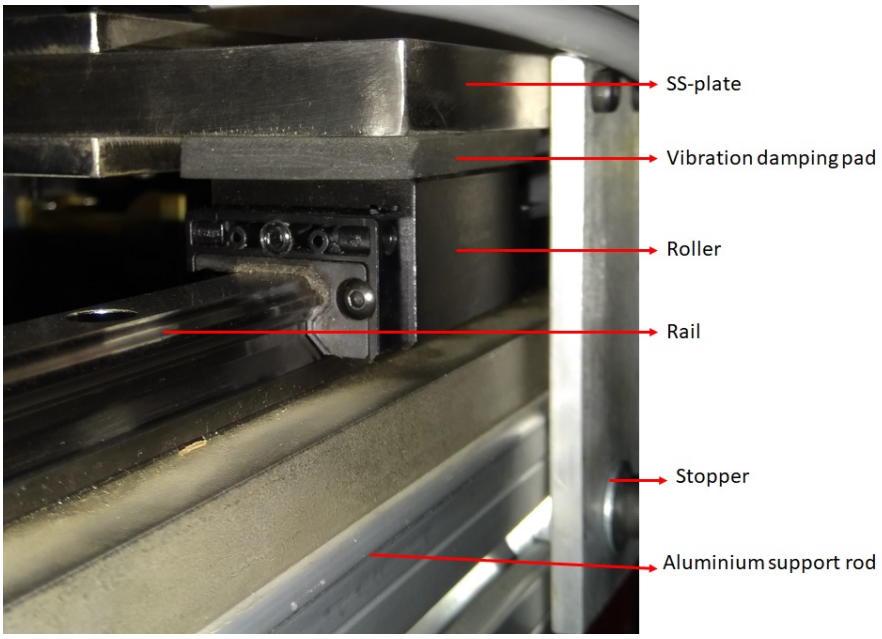

Figure 2.6: A closer view of the roller and rails assembly, mounted on the CCR-mounting frame is shown. This also incorporates vibration damping pads to effectively absorb vibrations from the CCR-refrigerator.

2.1.4 Steps for noise reduction

Noise reduction is one of the main challenges in instrumentation, and the aim is to improve the signal to noise ratio during the spin-caloritronic measurements. Generally, the lock-in detection technique is used to detect any small AC-signal, where an AC-modulation is used to measure the signal in a very narrow frequency range. However, the spin-caloritronic signals of our interest are mainly DC-voltages and also in the nano-volt (nV) range, which requires to isolate out all the noise sources to improve the signal quality.

The steps to reduce the noise are discussed as follows:

(I) The first and essential part is to make good electrical connections in detecting the signals. All the solderings to the wires are made with a shiny curved surface avoiding any sharp features. The main reason is that such a spike may act as an antenna to catch noise. The number of soldered joints is also minimized.

(II) Two coaxial-cables are chosen for sensing the voltage, where the shields of both cables are shorted and connected at a single point of the CCR body. Thus, those shields are also connected to the ground via the CCR-body. It significantly reduces the inductive noise to the wires. LakeShore SC-type cables are used for these voltage measurements.

(III) Each shielding of the coaxial cable is star grounded at the CCR body to avoid ground loop.

(IV) Proper thermal anchoring to the cables is done by tightly placing them around the cold-head of the CCR. It is also taken care that none of the cables moves during measurements. It is important because some portion of the cables are also exposed to the external magnetic field. Thus, any small vibration can induce an electromotive force (EMF) inside the cable. Since our signal is in the range of a few decades of nV, it is crucial to reduce such EMF induction.

(V) The voltage sensing cables are placed at a maximum possible distance apart from the temperature sensing cables, and also connected to a vacuum compatible LEMO connector to send out a signal from the CCR to nano-voltmeter. All other cables are connected to a separate 16-pin connector.

(VI) Vibration damping pads are used in the frame to reduce the vibration in the set-up. Also, extra weights are put on the frame as well as on the SS-plate to reduce

the vibrations. Figure 2.4 and Fig.2.6 depict various vibration damping pads used in our set-up.

(VII) The whole set-up is put inside a Faraday cage, made by Aluminium plates. This arrangement helps significantly in cutting down all the external electromagnetic noise sources. Figure 2.7-(a) & (b) show the inside and outside view of the Faraday cage, respectively.

(VIII) As we put the CCR inside the Faraday cage, the sound of CCR makes a standing wave trapped inside the cage. Thus, sound-absorbing foams are attached to the inner walls of the Faraday cage to reduce this effect.

(IX) The nano-voltmeter is also kept inside the Faraday cage. Chassis ground of the nano-voltmeter is also connected to the CCR-body.

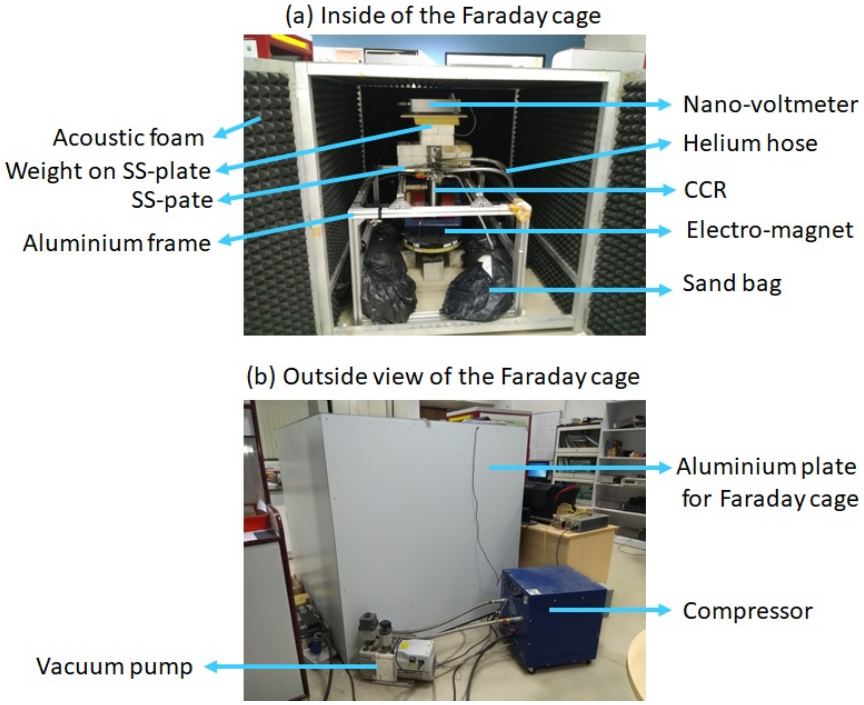

Figure 2.7: (a) shows inside view of the Faraday cage, (b) shows outside view of the Faraday cage.

The noise level is checked by shorting the ends of the voltage picking wires at the sample holder. The temperature of the sample-space was maintained at 290 K by the heaters attached to the holder. The CCR compressor was kept ON. Thus, the observed voltage is due to the background contributions which is basically the thermopower generated in the wires by the cooling process. A magnetic field of 2000 Oe was also applied to check whether there is any EMF induced noise in the wires. Fig. 2.8 shows a plot that depicts the background voltage with respect to the elapsed time. It is observed that initially, the background varies rapidly, and then it slowly comes down to a constant level. It is also observed that it takes almost 3-hours to settle down to a constant level where the noise level is found to be around 5nV.

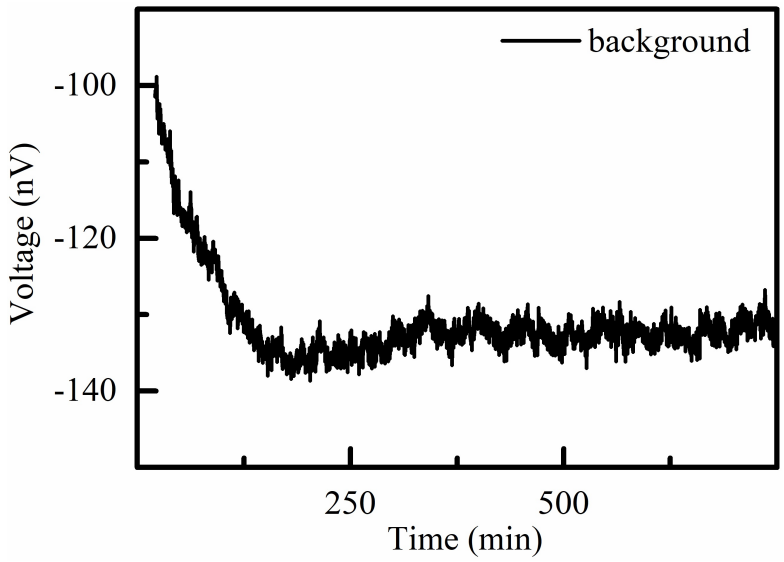

Figure 2.8: shows the background voltage, measured in our set-up. It was measured at the applied magnetic field of 2000 Oe.

2.1.5 Measurement protocols:

Since the spin-caloritronics signals appear in a direction orthogonal to both the applied magnetic field (H) and the thermal gradient ($\vec{\nabla}T$), the geometry of the sample

is always chosen to be rectangular. The protocols used for different spin-caloritronic measurements are as follows:

(I) **T-dependence of the signal:** In this measurement, the average sample temperature (T_{av}) varies stepwise from 12K to 300K, while the applied thermal gradient ($\vec{\nabla}T$) and strength of the magnetic are kept constant. The voltage is measured in a direction transverse to both the applied magnetic field and the thermal gradient. The direction of the magnetic field is reversed to cancel the background contribution during temperature-dependent measurements. Thus, the actual signal is quantified by $V_{signal}(T) = \frac{1}{2}\left(V(+H) - V(-H)\right)$.

(II) **H-dependence of the signal:** In this case, the signal is measured by varying the magnetic field. However, the voltage measurement axis is always kept orthogonal to both the magnetic field and the thermal gradient. The initial voltage at $H = 0$ Oe is considered as the background-voltage. Thus, the signal is quantified as $V_{signal}(H) = (V(H) - V(0))$, while both the T_{av} and the $\vec{\nabla}T$ are kept fixed.

(III) **∇T-dependence of the signal:** In this type of measurement, the signal is measured by varying the thermal gradient in a stepwise manner up-to $(\nabla T)_{max} = 15$K, while the magnitude of the external magnetic field and the cold end of the sample are kept constant. It is worth mentioning that the direction of the magnetic is also reversed to cancel out the background, and thus the signal is quantified as $V_{signal}(\nabla T) = \frac{1}{2}\left(V(+H, \nabla T) - V(-H, \nabla T)\right)$.

(IV) **θ-dependence of the signal:** In this particular type of measurement, the direction of the external magnetic is rotated in a plane orthogonal to the applied thermal gradient. The angle θ is measured with respect to the voltage detection axis. It is worth mentioning that all other parameters, like, the magnitude of the magnetic

field ($|H|$), applied thermal gradient($\vec{\nabla}T$), and the sample temperature (T_{av}), are kept fixed. The signal is quantified as $V_{signal} = (V(\theta) - V(0))$.

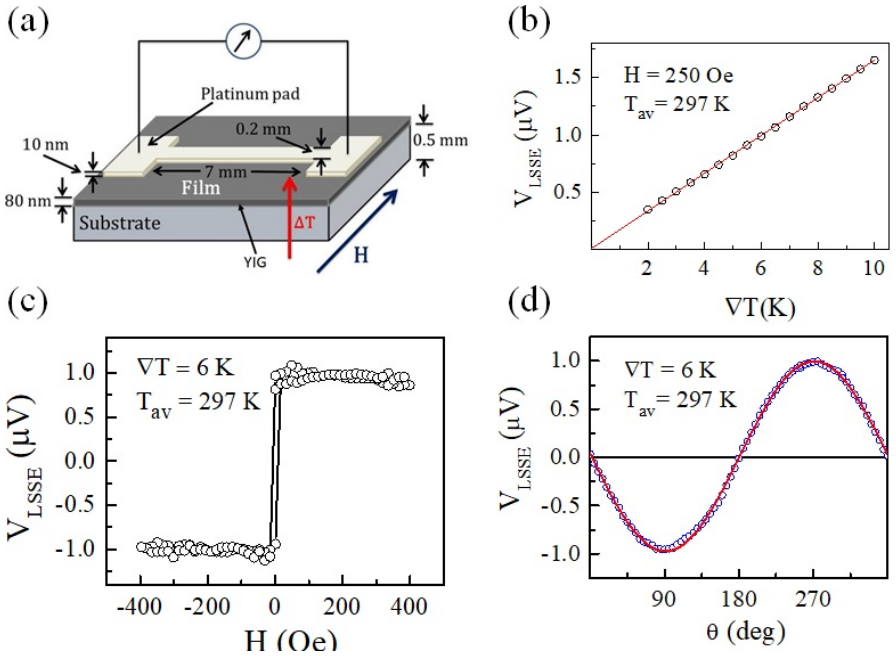

Figure 2.9: (a) shows the device geometry made up with YIG/Pt bilayer system, (b) depicts the V_{LSSE} vs. $\vec{\nabla}T$ plot, (c) depicts the V_{LSSE} vs. H plot, and (d) depicts V_{LSSE} vs. θ plot.

After setting up the measurement unit, the first attempt was to reproduce the LSSE signal in a magnetic-insulator. Yttrium Iron Garnet (YIG) sample has been used as the magnetic-insulator, and Pt has been used as the spin-to-charge conversion layer. 80 nm thick YIG film has been grown on a non-magnetic GGG ($Gd_3Ga_5O_{12}$) substrate by the pulsed laser deposition technique. The Pt-layer of 10 nm thickness has been deposited on top of that YIG layer by the DC-sputtering deposition technique. The standard optical lithography technique was used for patterning the Pt-bar. Fig.2.9-(a) depicts the YIG/Pt device used for the observation of the LSSE signal. The linearity of the measured voltage as a function of ∇T with the cold end of the device is fixed at 292 K, and the magnetic field at 250 Oe is shown in Fig. 2.9(b). Fig. 2.9(c) depicts the hysteresis in the signal as a function of varying magnetic fields at a mean sample

temperature, T_{av} = 297K. Fig. 2.9(d) depicts a sinusoidal variation of the signal, measured by rotating the magnetic field in a plane orthogonal to the applied $\vec{\nabla}T$, where all other parameters, like, the $\vec{\nabla}T$, $|H|$, and T_{av} are kept fixed at 6 K, 250 Oe, and 297 K, respectively. It is observed that the measured signals from the YIG/Pt thin film system are in good agreement with the previous reports [115–117].

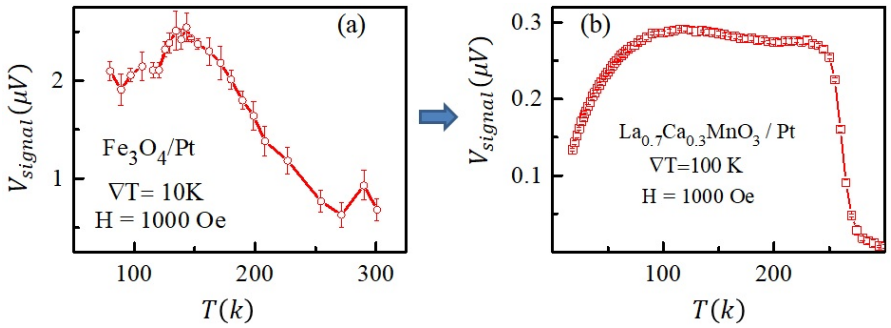

Figure 2.10: shows the improvements in signal to noise ratio by the steps taken for reducing the noise.

All the measurements on this YIG/Pt system have been taken before enclosing the set-up in the Faraday cage. The signal to noise ratio is much improved after using the Faraday cage. Figure 2.10 is presented to show the progress in terms of the quality of the measured signals by the steps taken care of to reduce the noise. Figure 2.10(a) shows measurements on the Fe_3O_4/Pt system, where the maximum signal is approximately 2.5μV, where the maximum noise level is approximately 200 nV. However, after taking care of all noise reduction steps, it is observed that a much better signal to noise ratio could be achieved. Figure 2.10 (b) depicts a recent measurement on the $La_{0.7}Ca_{0.3}MnO_3$/Pt system, where the signal voltage of 0.3μV with a noise level of less than 5 nV could be reliably measured. It is worth mentioning that every time we wait for 3 to 4 hours after switching ON the compressor and continuously monitor whether the background achieves its steady-state before starting any further measurement. The

background level in a loaded sample may change due to the contacts made across the sample and/or incidental thermo-power generated across the sample.

2.2 Sample fabrication & characterization

All the techniques and tools used for device fabrication and characterizations, are briefly discussed in the following sub-sections.

2.2.1 Fabrication tools

(I) Pulsed laser deposition (PLD) technique: This tool is commonly used to grow epitaxial oxide thin films. The basic operation of this technique is based on the direct ablation of target materials of a desired composition by using a high powered laser to deposit the material on top of the substrate facing the target. This process can occur in an ultra-high vacuum or in the presence of a background gas, such as oxygen, when depositing films of oxides. Figure 2.11 depicts a schematic of the PLD system.

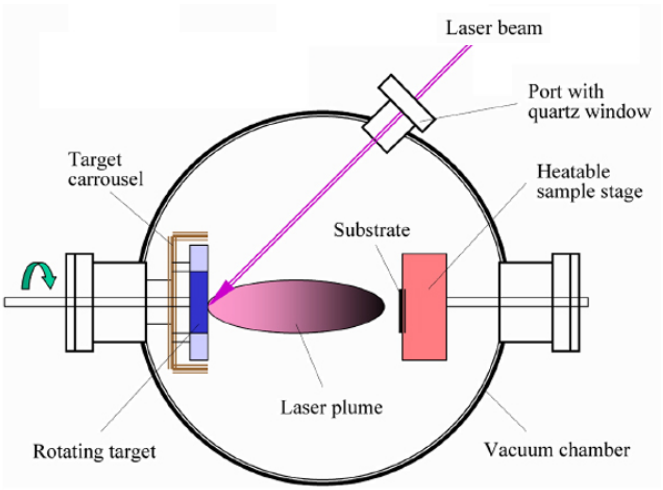

Figure 2.11: Schematic representation of PLD process. Figure is reprinted from Ref. [118], with the permission of AIP.

The complete depositing process occurs in three steps. The first step is the interaction of the laser beam with the target-material. When the high power laser strikes the material, it penetrates inside the target surface (approximately 10 nm) and ejects free electrons due to electronic excitation by the laser. This process depends on the energy of the laser beam. Thus, the wavelength of the laser is an important parameter in this deposition technique. In the second step, the released free electrons collide with the target material and generate enough heat to vaporize the material. This evaporated material again interacts with the incident laser beam resulting in an isothermal plasma formation. In the last step, the plasma adiabatically expands in a direction perpendicular to the target surface, and gets deposited on the substrate.

The deposited film quality depends on the pressure inside the chamber, substrate temperature, laser energy, laser pulse rate, and lattice mismatch between substrate and target material [119]. For instance, we have used the KrF excimer laser of wavelength $\lambda = 248$ nm for the deposition of $La_{0.7}Ca_{0.3}MnO_3$ (LCMO) thin films, as mentioned in Chapter 3. All the films are grown on the [100] planes of the substrates, where single-crystalline $LaAlO_3$ (LAO) and $SrTiO_3$ (STO) are taken as the substrates owing to their low lattice parameter mismatch with LCMO. The pulse frequency of the laser beam is kept at 5 Hz, and the energy density of the laser spot on the target is kept fixed at $2J/cm^2$. The substrate temperature is kept at 700°C, and the Oxygen pressure during the deposition is kept at 100 milli-Torrs. All these conditions are maintained for growing an epitaxial LCMO film on the substrate. The detailed characterizations are mentioned in Chapter 3.

(II) Magnetron sputtering technique: Sputtering is one of the easiest and most flexible ways of making uniform thin films. Similar to PLD, sputtering is also a physical vapor deposition technique. The basic principle of sputtering is based on the ejection

of atoms from the target surface by the bombardment of highly energetic positive ions called sputter-gas [120–123]. The sputtering ions are accelerated by a negative voltage applied to the target, which acts as a cathode, causing the bombardment process for the removal of target atoms. The sputtered atoms are then condensed on a substrate as a thin film. The conventional sputtering process usually gives low deposition rates and needs very high cathode voltage along with high sputter-gas pressure to sustain the plasma [121]. Alternatively, the magnetron sputtering technique can be used to overcome the problems in a conventional sputtering system. A magnetron-sputtering system utilizes strong magnetic fields to confine charged plasma particles close to the surface of the sputter-target in order to increase the sputter yield. This is done by placing magnets behind the target. The sputtered atoms are mostly charge-neutral and also much heavier than the sputter-gas atoms and are therefore unaffected by the magnetic trap. Since magnetron sputtering system contains magnetic field, sputtering of non-magnetic metals are more easier as compared to magnetic metals in terms of depositing good quality film. We mainly used the magnetron sputtering technique for depositing metals, like, Pt, W, Au, Cu, and Ta.

Based on the sputter-gas used during sputtering, there are two types of sputtering process are performed in depositing thin films. The first type is a non-reactive sputtering process where an inert gas (typically Ar) is used. The second type is reactive sputtering, where a chemically reactive gas (O_2, N_2, etc.) is inserted into the system. The basic configuration of a sputtering-system is shown in Fig.2.12 where the target material to be used as a coating is placed in a vacuum chamber parallel to the substrate to be coated. A target holder is used for holding the target-material as well as applying the required electric field for the sputtering process. The distance between the substrate and the target is also calibrated for achieving the desired coating rate. The thickness

monitoring sensor attached near the substrate measures the thickness of the coating. A quartz crystal microbalance (QCM) is used as the thickness sensor.

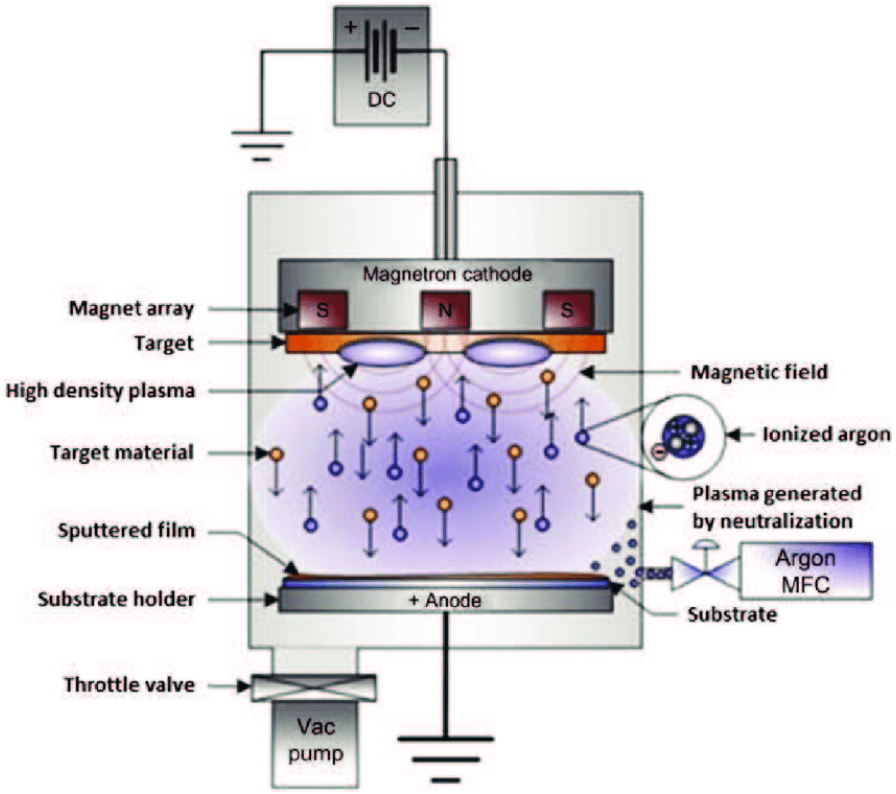

Figure 2.12: depicts a schematic of DC-magnetron sputtering process [124]. Figure is reprinted with permission from Ref. [124], Copyright (2019) by the Elsevier.

After loading the target and the substrate, the vacuum chamber is evacuated to a base pressure of 10^{-7} millibar and then partially backfilled with a high purity Argon gas to an operating-pressure of 5×10^{-3} to 8×10^{-3} millibar during the deposition process. A DC electrical bias typically in the -200 to -400 Volt range is then applied to the target. A positive bias is also applied to the cap of the target-holder, which becomes the anode. The process begins with a stray electron near the cathode being accelerated towards the anode, which collides with a neutral gas atom converting it to a positively charged ion. The electrically charged Argon ions then accelerate towards the target to knock out the

atoms from the surface of the negatively charged target. Argon is commonly used as the sputter-gas due to its relative mass and ability to transfer kinetic energy upon impact during the collisions in the plasma that creates the gas ions. The deposition rate is kept at 0.3 Å/sec.

(III) Other fabrication tools: Besides the aforementioned techniques, various other facilities, like, crystal cutting and polishing tools (to cut the crystals in a desired dimensions and shapes), high temperature tube and box furnaces (for preparation of sputtering targets), and ball milling (for making fine powders) have also been used during the course of this work. Prof. Satishchandra B. Ogale from IISER Pune, India, has helped us during the PLD deposition process of LCMO thin films. The Ni-Mn-Ga alloy was prepared using the arc-melting technique by Dr. Sanjay Singh (Banaras Hindu University, India). $Y_2V_2O_7$ single crystals have been grown via the optical float zone technique by Dr. Dharmalingam Prabhakaran (University of Oxford, UK).

2.2.2 Characterization tools

(I) X-Ray diffraction (XRD): It is a powerful and non-destructive tool used to study the crystallographic structure of materials and thin films. In principle, when a monochromatic X-Ray beam of a specific wavelength λ is incident on a crystalline material, it is scattered elastically by the electrons of the atoms arranged periodically forming the material structure. These scattered X-Rays form a constructive interference pattern if the periodic arrangement of atoms comprises a set of parallel planes which satisfy the Bragg's law. The Bragg's law is given by:

$$2dsin(\theta) = n\lambda \tag{2.1}$$

where d is the inter planar distance, θ is the angle between the incident beam and the diffracting plane, and n is an integer. Thus, the intensities and positions of the peaks obtained in an X ray diffractogram directly yield the structural information of the material under study.

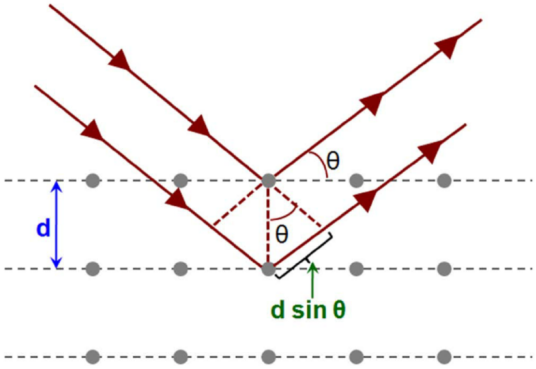

Figure 2.13: Schematic representation of X-Ray diffraction process.

The XRD measurements in this work were performed using a Bruker D8 Advance X-Ray diffractometer which works in Bragg-Brentano geometry ($\theta-2\theta$ scan), where the sample is kept fixed whereas both the incident X-Ray beam and the detector are moved simultaneously. The X-Ray wavelength used was 1.542Å(Cu-K_α radiation). The XRD pattern of the powdered sample was matched with the references provided by the Joint Committee of Powder Diffraction Standard (JCPDS) database.

(II) Magnetic characterizations: All the magnetic measurements, like, temperature dependence of the DC-magnetization (M-T), magnetic field dependence of the DC-magnetizations (M-H), and temperature dependence of the AC-magnetic susceptibility (χ-T), have been performed using the MPMS (Magnetic property measurement system)-XL SQUID (Superconducting Quantum Interface Device) from Quantum Design, USA. The measurement principle is based on the Faraday law of induction. It basically measures the voltage at the pick-up coil induced by the magnetic sample placed

inside the coil. The induced voltage is linked to the rate of change in the total magnetic flux across pick-up coil, and mathematically it can be written as :

$$V = -n\frac{d\phi}{dt} = -nA\frac{dB}{dt} \tag{2.2}$$

where n is the number of turns in the pick-up coil, A is the area under a single turn, and B is the magnetic field linked to the coil. In the MPMS-XL SQUID, the signal is picked up in a superconducting pick-up coil, placed at the center of a superconducting magnet. When the sample moves inside the pick-up coil, it produces a change in the persistent current which is inductively coupled to a SQUID loop. The SQUID loop is basically a closed superconducting loop containing one or two Josephson junctions. The magnetic field inside the SQUID is always quantized whose unit is in terms magnetic flux quanta: $\phi_0 = \frac{2\pi\hbar}{2e} \approx 2.0678 \times 10^{-15}$ Wb. This makes the SQUID detection extremely sensitive to measure minute changes in the magnetic flux. A schematic of the SQUID magnetometer is depicted in the Figure 2.14.

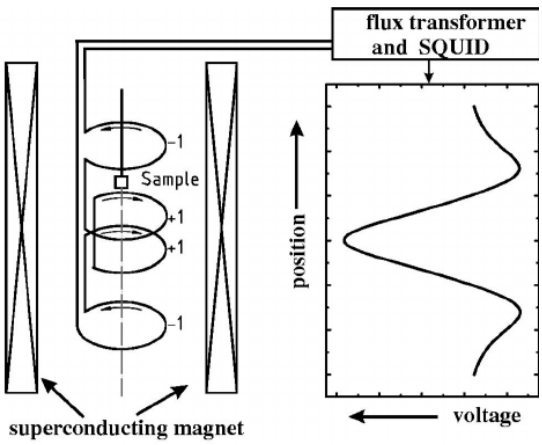

Figure 2.14: Schematic representation of a SQUID magnetometer [125].

(III) Transport characterizations: Various type of transport measurements like,

temperature (T) and field (H) dependence of the resistivity ($\rho(T)$ or $\rho(H)$), thermal-conductivity ($K(T)$), and Seebeck coefficient ($S_{xx}(T)$) have been carried out in the PPMS (Physical Property Measurements System) with the Model No-6000 from Quantum Design, USA. All the measurements are performed in the range $2K$ to 300K using the four probe method.

(IV) Other characterization tools: Apart from the above mentioned characterization tools, various other facilities, like, atomic force microscopy (AFM) and Energy dispersive X-ray spectroscopy (EDXS) have been used during the course of this work for measuring the surface roughness of the thin films and to confirm the compositions of the materials, respectively. Laue diffraction was performed on single crystalline samples for determining the crystal orientation as well.

Chapter 3

The longitudinal spin Seebeck effect in a mixed valent manganite

This chapter describes detailed investigations about the temperature dependence of the longitudinal spin Seebeck effect (LSSE) signal, as measured in the bilayer system of $La_{0.7}Ca_{0.3}MnO_3$(LCMO)/Pt. By disentangling the parasitic contribution arising due to the anisotropic Nernst effect (ANE), we observe that the LSSE exhibits a $T^{0.5}$ dependence in the low-temperature regime, which matches well with the prediction of the magnon-driven spin current model. On the other hand, the LSSE exponent is found to be significantly higher than the magnetization one across the double exchange driven paramagnetic-to-ferromagnetic transition. Moreover, it is also observed that the critical exponent of the LSSE signal depends on the thickness of the spin-to-charge conversion layer. These observations emphasize the importance of individually ascertaining the temperature evolution of different mechanisms – especially the spin mixing conductance – which contribute to the measured spin Seebeck signal.

3.1 Introduction

The spin analogue of the Seebeck effect, the Spin Seebeck effect (SSE) refers to the generation of a magnonic spin current under the application of a thermal gradient ($\vec{\nabla}T$) across a magnetic material [1–5, 7]. The preferred measurement approach for this spin current is in the form of the longitudinal spin Seebeck effect (LSSE). In this longitudinal mode, a normal metal (NM) having a substantial spin-orbit interaction (typically Pt or W) is coated on top of the magnetic material, and a temperature gradient is applied perpendicular to the plane of the interface [6]. As a result, the spin current generated in bulk of the magnetic layer flows parallel to the applied thermal gradient towards the interface, and a certain amount of this spin current enters into the NM layer by means of thermal spin-pumping. Finally, the net pumped spin current in the NM layer is further converted into a measurable electrical voltage through the inverse spin Hall effect (ISHE) [126]. Mathematically, the voltage due to the ISHE could be written as $\vec{E}_{LSSE} \propto \theta_{SH}(\vec{j_s} \times \vec{\sigma})$ – where, θ_{SH} is the spin Hall angle of the NM layer, $\vec{j_s}$ is the net spin current at the NM layer, and $\vec{\sigma}$ is the spin polarization vector of the conduction electrons in the NM layer [1, 126]. It is worth mentioning that the polarity of the detected voltage is determined by contributing factors like θ_{SH}, $\vec{\sigma}$, and $\vec{j_s}$. Thus, the true nature of the SSE could be confirmed by utilizing different spin-to-charge conversion layers (e.g. Pt and W) having opposite sign of the spin Hall angles [72]. Till date, a volume of investigation on the SSE in magnetic insulators (MI) has been detailed in literature. Heterojunctions consisting of the ferrimagnetic insulator $Y_3Fe_5O_{12}$ (YIG) and Pt are now recognized as being model systems for studying of the LSSE. After initial measurements aimed at validating the true magnonic nature of the spin current [2, 3,

7] and weeding out possible experimental artifacts [109, 110, 127], more recent measurements have focused on the dependence of the LSSE signals on control parameters like temperature, [4, 117, 128, 129], magnetic field [130, 131] and sample thickness [107, 132]. In this context, temperature dependent LSSE measurements have unveiled a distinct connection of this quantity with intrinsic properties of the magnetic material which also manifests itself in the form on a non-trivial T-dependence of the measured LSSE voltage. A natural extension of this mode of enquiry would be to use LSSE measurements in the investigation of other temperature dependent strongly correlated phenomena to ascertain the relative roles of the underlying microscopic mechanisms. A few systems have already been explored in this fashion, including the Verwey transition in Fe_3O_4 [133], the spin reorientation transition in $Gd_3Fe_5O_{12}$ [71] and the double exchange driven para-to-ferromagnetic transition in $La_{0.7}Sr_{0.3}MnO_3$ [134].

It is to be noted, that an applied thermal gradient ($\vec{\nabla}T$) across a magnetic metal (MM) can also generate a transverse voltage orthogonal to both the magnetization ($\vec{M}$) and the $\vec{\nabla}T$ owing to the anomalous Nernst effect (ANE) [88, 103, 135, 136]. The electric field due to ANE could be expressed as $\vec{E}_{ANE} \propto \vec{\nabla}T \times \vec{M}$ [137]. Since magnetic insulators (MI) do not have conduction charges, the LSSE measurements in MI enable harvesting of pure spin currents [5, 109, 110]. Besides the possible emergence of ANE in the magnetic sub-unit, the utilization of Pt as a spin-to-charge conversion could be associated with the proximity induced ANE. Thus, investigation of LSSE in MM/Pt system is plagued by the contaminated LSSE-signals, where the parasitic signals emerge as a result of ANE in the magnetic subunit as well as the proximity induced ANE in the Pt-layer [103]. Here we note that, along with the LSSE, the incidental ANE contributes additively to the measured voltage under the geometry of the LSSE-measurements. Clearly, the disentanglement of the ANE contribution from

the LSSE signal is essential for an accurate quantification of the LSSE phenomena. This is especially important since the agreement between theory and experiments remains tenuous both in the vicinity of the magnetic phase transitions, as well as in the low-temperature regime where the magnonic spin current is expected to be relatively unaffected by phonons and other associated scattering mechanisms [138, 139].

Mixed valent manganites of the form $La_{1-x}A_xMnO_3$ (with A being a divalent alkali metal) and their layered variants have been the subject of extensive investigations in the past. The optimally doped members of this family, where double exchange gives rise to ferromagnetism as well as concomitant metallicity, are of special interest in spintronics owing to their high spin polarization and colossal magnetoresistance [140]. A previous LSSE report based on the $La_{0.67}Sr_{0.33}MnO_3$/Pt system suggests that more than 95% of the measured voltage arises due to the LSSE alone where the ANE contribution is negligibly small [134]. However, the characterization of that LSSE signal is ambiguous because the measured spin Seebeck voltages with both Pt and W spin-to-charge conversion layers are in the same polarity although the sign of the spin Hall angle of Pt and W are opposite to each other [72]. This chapter provides the measurements of the LSSE signals in a closely related $La_{0.7}Ca_{0.3}MnO_3$ (LCMO) system in an attempt to resolve the apparent ambiguity in LSSE signals as reported in the $La_{0.67}Sr_{0.33}MnO_3$ system. More importantly, our findings provide critical insights into the functional form of the LSSE-signal – especially in the low-temperature regime as well as in the vicinity of the magnetic phase transition.

3.2 Deposition of the LCMO films and X-Ray characterization

The LCMO films of thickness 200 nm were deposited on both the $LaAlO_3$ (LAO[100]) and the $SrTiO_3$ (STO[100]) substrates by utilizing the PLD techniques. A KrF excimer laser ($\lambda = 248nm$) was operated at a frequency of 5 Hz with energy density 2J/cm^2 for the deposition process. The temperature of the substrates was maintained at 700°C during the deposition process, while the Oxygen pressure inside the PLD-chamber was kept at 100 mTorr. After the deposition process, all the films were annealed at 900°C in an O_2 atmosphere with 1 atm pressure for 3 hours.

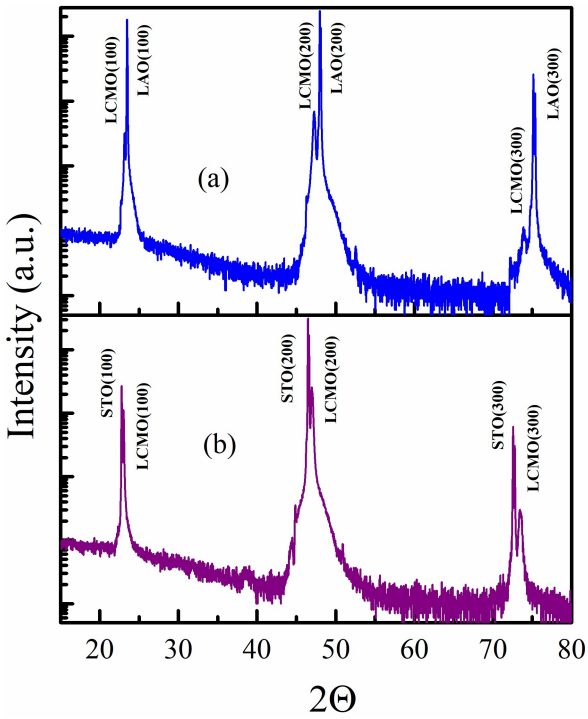

Figure 3.1: (a) and (b) depict the XRD patterns of the epitaxial film of LCMO, grown on LAO[100] and STO[100] substrates, respectively.

Figure 3.1 (a) and (b) depict the XRD pattern of the LCMO films deposited on

LAO[100] and STO[100] substrates, respectively. The LCMO films on both the LAO and the STO substrates are found to be epitaxial. It is worth mentioning that all the films on the LAO [100] substrates were deposited and annealed together in a single batch – thus, the properties of all the LAO/LCMO systems are expected to be identical. Similarly, all the films on the STO substrates were deposited and annealed together in another batch. The primary purpose of the STO/LCMO films is to cross-check the role of the effective thermal gradient ($\vec{\nabla}T_{eff}$), that is employed across the LCMO layer only, in determining the T-dependence of the LSSE signal. Bruker D8 Advance high-resolution X-ray diffractometer was used to take the XRD measurements.

3.3 Magnetic and transport characterizations

The LCMO films are also characterized by magnetic and transport measurements. Temperature dependence of the magnetization ($M(T)$) was measured at an external magnetic field of 1000 Oe, whereas resistivity ($\rho(T)$) measurements were performed in the absence of any magnetic field. Figure 3.2(a) depicts a double-plot of both the $M(T)$ and the $\rho(T)$ data of the LCMO film grown on the LAO substrate (LAO/LCMO), whereas Fig. 3.2(b) illustrates the first derivative of the $M(T)$ of LAO/LCMO film. The para-to-ferromagnetic transition temperature (T_C) of this LAO/LCMO film is determined from the first derivative of the $M(T)$ data, where the T_C is found to be 258.5 K. Similarly, Figure 3.2(c) depicts another double-plot illustrating both the $M(T)$ and the $\rho(T)$ data of the LCMO film grown on the STO substrate (STO/LCMO). The T_C of this STO/LCMO system is found to be around 230 K as illustrated in Figure 3.2(d). It is worth mentioning that the T_C of LAO/LCMO system matches well with that of the stoichiometric $La_{0.7}Ca_{0.3}MnO_3$ composition [141, 142]. However, T_C of the STO/LCMO

system is at a lower temperature in comparison with the LAO/LCMO system possibly due to slight Oxygen deficiency. A volume of investigation has been detailed in literature determining the T_C of the LCMO thin films, and both the magnetic and resistive characterizations of our LCMO films are in agreement with the previous reports of the thin films of similar compositions [143–146].

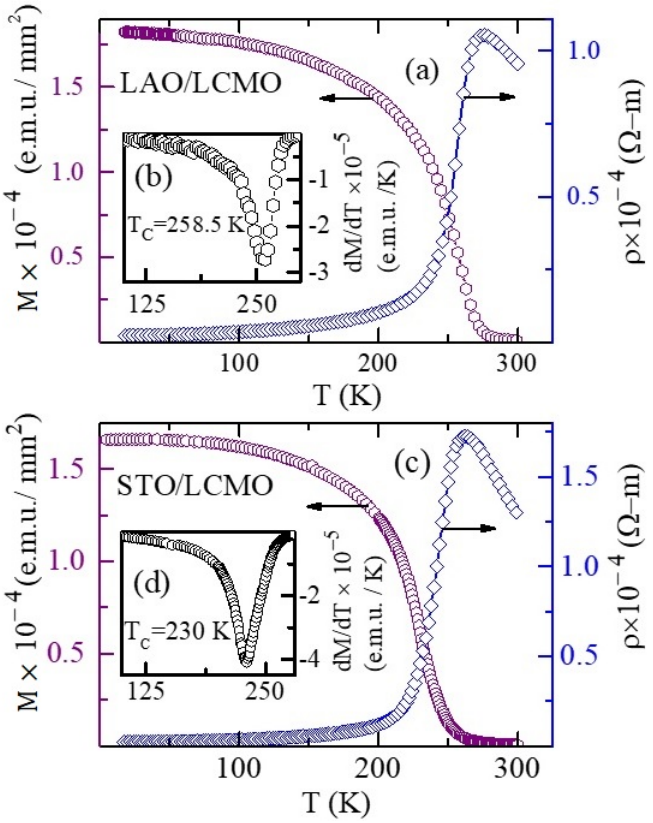

Figure 3.2: (a) double plot for the temperature dependence of both the magnetization and the resistivity of the LAO/LCMO system. (b) $\left(\frac{dM}{dT}\right)$ vs. T plot showing the T_C at 258.5K. (c) double plot for the temperature dependence of both the magnetization and the resistivity of the STO/LCMO system (d) $\left(\frac{dM}{dT}\right)$ vs. T plot showing the T_C at 230K.

3.4 Spin-caloritronic measurements

For measuring the LSSE voltage, a thin layer of Pt is deposited on top of the LCMO layer by DC magnetron sputtering. Depending on the thickness of the Pt layer, as well

as the choice of substrate, three different devices were made: (i) LAO/LCMO/Pt10, (ii) LAO/LCMO/Pt5, and (iii) STO/LCMO/Pt10 - with the Pt thickness in these devices being 10 nm, 5 nm, and 10 nm respectively. A separate device (LAO/LCMO/W13) was also fabricated, where 13 nm of W was used instead of Pt for the spin-to-charge conversion to confirm the intrinsic nature of the inferred LSSE signals. Since the LCMO films are metallic in nature (as observed from Fig.3.2 (a)& (b)), the LSSE signal appears along with the inevitable ANE signals. To date, many experiments are focused on disentangling the LSSE signal from the ANE by using a non-magnetic spacer layer between the ferromagnet and the NM layer [147–149]. Although insertion of such a spacer layer is useful for harvesting pure LSSE signal, it can also change the properties of the interface and can attenuate the intrinsic LSSE signal [107, 108]. Thus, instead of utilizing such a spacer layer, the measurements are taken in the standard LSSE geometry on both a bare LCMO film and LCMO-Pt (or LCMO-W) bilayer system – where we separately measured the ANE signal (V_{ANE}) from the bare LCMO films, and then it was subtracted from the total signal (V_{Total}) measured from the LCMO/Pt (or LCMO/W) bilayer system. It is important to note that we neglect the possible role of proximity induced ANE contribution. Recently, a quantitative disentanglement of the LSSE from the spurious ANE contributions has been reported – where, using a set of $NiFe_2O_x$/$Ni_{33}Fe_{67}$-Pt bilayers (with sample resistances varying across 7 decades) in both in-plane and out-of-plane measurement geometries, it was demonstrated that the proximity-induced ANE was a contributory factor only in the most metallic of specimens (with $\rho \propto 10^{-7}\Omega m$) [103], and it became negligible if the resistivity of the magnetic sistem is in the order of $10^{-5}\Omega m$ or larger ($\rho \geq 10^{-5}\Omega m$). Since manganites are known to be *dirty* metals (with resistivity of the order of $10^{-4}\Omega m$), contamination of the LSSE signals by the proximity-induced ANE can thus be ignored, where the V_{Total}

is considered to be the sum of the intrinsic LSSE contribution (V_{LSSE}) and the V_{ANE} generated in the bare LCMO layer. Figure 3.3 (a) and (b) depict the schematics of the device for the measurement of ANE and total-signal (LSSE+ANE), respectively. In our geometry, the ∇T is applied across the thickness of the films (along the z-direction). The external magnetic field (H) is applied along the x-direction (in-plane with the films), and the transverse voltage is measured along the y-direction.

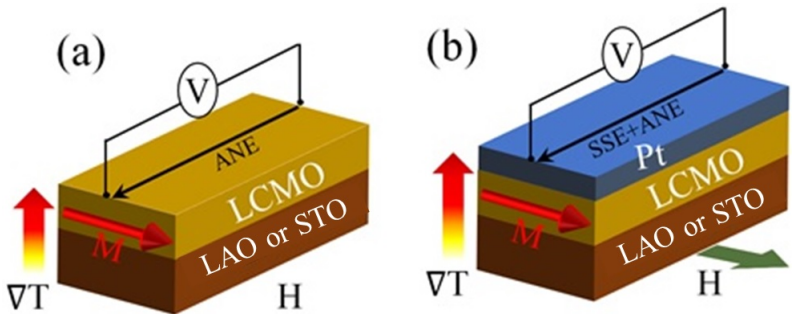

Figure 3.3: (a) and (b) are the schematic illustrations of the device for measuring the ANE and the Total signal (LSSE+ANE), respectively.

Since these voltages are measured across different effective resistances, we report all the voltages in their normalized form, i.e., $V_i = V_i'/(R_i'\nabla T L_y)$, where V_i' is the measured transverse voltage, R_i' is the corresponding resistance between the contact probes, L_y is the distance between the contact probes, and the index $'i'$ refers to the ANE and the total-signal. Thus, the LSSE signal is quantified as

$$V_{LSSE} = V_{Total} - V_{ANE} = \frac{V'_{Total}}{\Delta T * R'_{Total} * L_y} - \frac{V'_{ANE}}{\Delta T * R'_{ANE} * L_y} \tag{3.1}$$

where, V'_{Total} and R'_{Total} are the raw total voltage and the corresponding resistance between the contact probes on the LCMO/Pt system, respectively. Similarly, V'_{ANE} and R'_{ANE} are the raw ANE-voltage and the corresponding resistances between the contact probes on the bare LCMO film, respectively. Thus, during the ANE measurement, the

$V_i' \equiv V_{ANE}'$, and similarly, during the measurements of the raw total-signal $V_i' \equiv V_{Total}'$. The measured L_y from each film is mentioned in the Table 3.1.

Table 3.1: L_y of each film

Measured signal	**Device**	L_y (mm)
ANE	LAO/LCMO	3
Total	LAO/LCMO/Pt10	2.7
Total	LAO/LCMO/Pt5	3
ANE	STO/LCMO	3.2
Total	STO/LCMO/Pt10	3.2

Figure 3.4(a) depicts the hysteresis in these signals (ANE, total, and LSSE) as a function of varying magnetic field at a mean sample temperature of 105K, with the ∇T being fixed at 10 K. Figure 3.4(b) depicts the linearity of the measured voltages (and the inferred V_{LSSE}) as a function of ∇T with the cold end of the specimen fixed at 100 K and the magnetic field at 1000 Oe. The magnitude and the sign of the measured V_{LSSE} with the Pt and W spin-charge conversion layers are commensurate with the experimentally determined Spin Hall angles of these heavy metals [72] – confirming the intrinsic nature of the inferred LSSE signals.

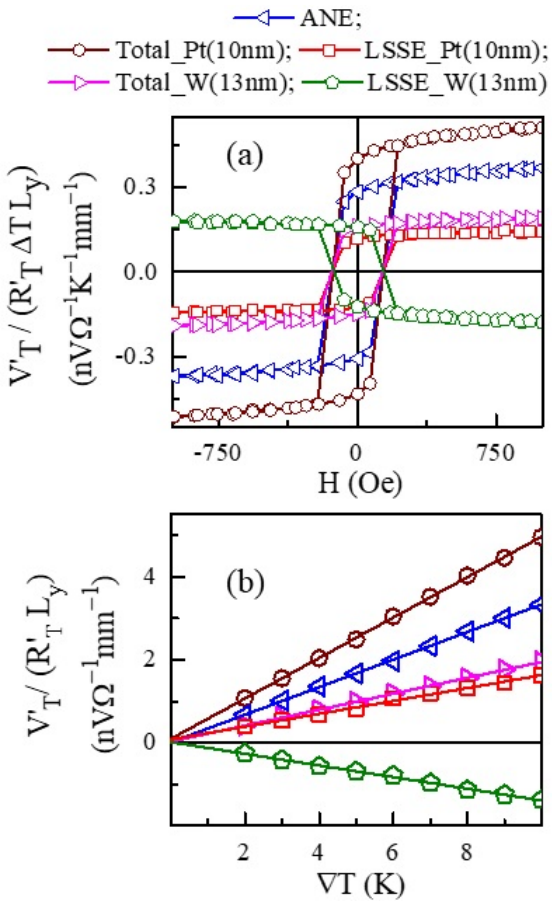

Figure 3.4: (a) and (b) depict the H and ∇T dependence of these signals with a 10 nm Pt and a 13 nm W spin-to-charge conversion layer. The linearity as a function of ∇T and the reversal of the sign of the LSSE signal between the Pt and W layers confirms the intrinsic nature of the measured spin Seebeck signal.

3.4.1 Measurements of T-dependent LSSE

The temperature dependence of both the raw ANE-voltage (V'_{ANE}) and the corresponding resistance (R'_{ANE}) between contact probes are depicted in Figure 3.5 (a) & (b) measured from the LAO/LCMO and STO/LCMO systems, respectively. Both the ∇T and the H are maintained at 10K and 1000 Oe, respectively – whereas, the average sample temperature (T) varies stepwise from 18 K to 300 K during the measurements.

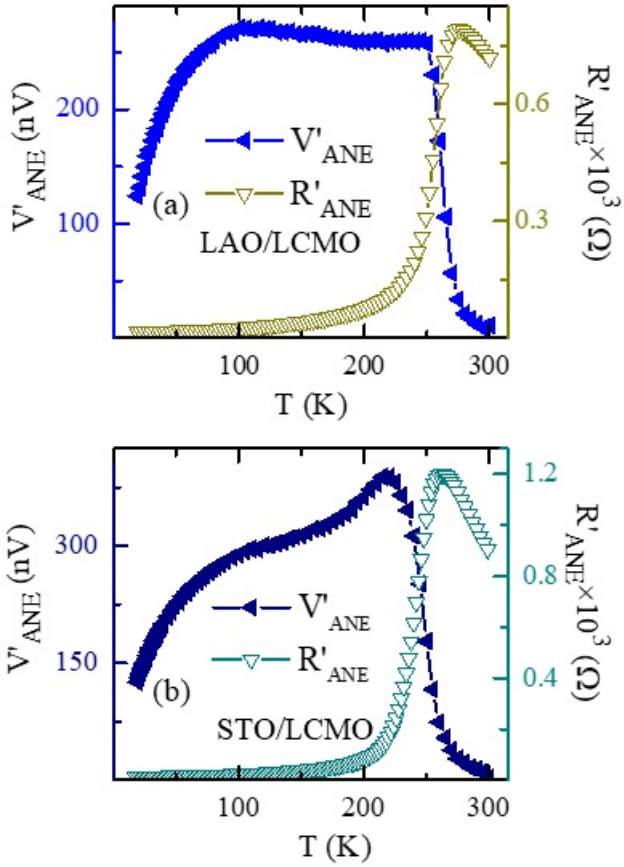

Figure 3.5: (a) and (b) depict a double plot of both the $V'_{ANE}(T)$ and the corresponding $R'_{ANE}(T)$, measured from the LAO/LCMO and the STO/LCMO system, respectively.

Similarly, the temperature dependence of both the raw total-voltage (V'_{Total}) and the corresponding resistance (R'_{Total}) between contact probes are also depicted together in a double-plot for each device. Fig. 3.5(a), 3.5(b), and 3.5(c) illustrate these double-plot where the measurements are taken from (i) LAO/LCMO/Pt10, (ii) LAO/LCMO/Pt5 and (iii) STO/LCMO/Pt10 systems, respectively. The measurement protocols of the total signal are similar to that for the ANE-signal (the $\nabla T = 10$ K, and $H = 1000$ Oe).

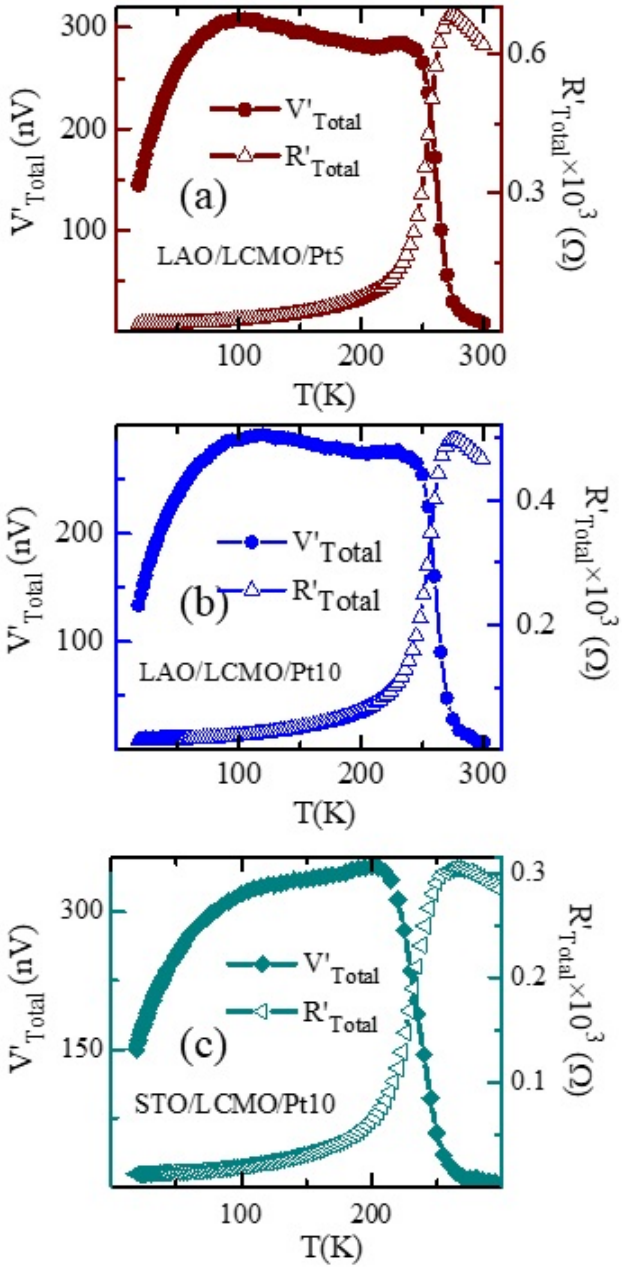

Figure 3.6: (a), (b), and (c) depict a double plot of both the $V'_{Total}(T)$ and the corresponding $R'_{Total}(T)$, measured from the LAO/LCMO/Pt10, the LAO/LCMO/Pt5, and the STO/LCMO/Pt system, respectively.

3.5 Analysis of the T-dependent LSSE signals

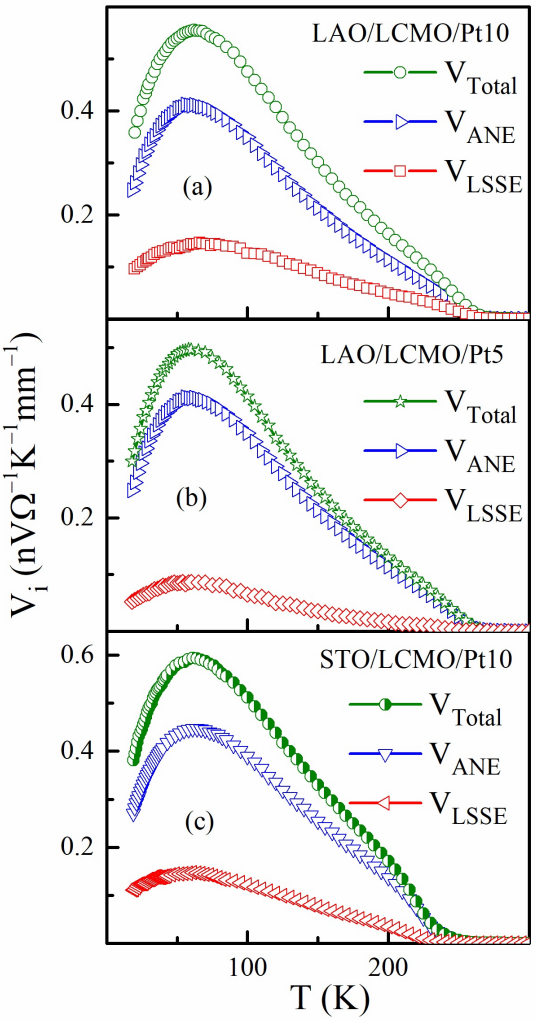

Figure 3.7: (a), (b), and (c) depict the temperature dependence of the total, ANE and LSSE signals as measured from LAO/LCMO/Pt10, LAO/LCMO/Pt5, and STO/LCMO/Pt10 systems, respectively.

Temperature dependence of the individual LSSE signals from all three LCMO/Pt devices, along with the associated ANE and the total signals, are depicted in Fig.3.7 (a)-to-(c). Plots corresponding to Fig.3.7(a), 3.7(b), and 3.7(c) illustrate the measurements

taken from (i) LAO/LCMO/Pt10, (ii) LAO/LCMO/Pt5, and (iii) STO/LCMO/Pt10 devices, respectively. Figure 3.7(a) and 3.7(b) indicate that a slight reduction in the magnitude of LSSE signals as a function of decreasing Pt thickness, which is consistent with prior reports on YIG/Pt bilayers [150, 151]. In similarity to that reported in other systems, a peak in the $V_{LSSE}(T)$ is also observed at lower temperatures [117, 132]. This peak deep within the magnetically ordered regime is a defining feature of all T-dependent measurements of LSSE and is attributed to the temperature dependence of the magnon relaxation rates and population.

3.5.1 LSSE in the low-temperature regime

Theoretical descriptions suggest that the magnon-driven Spin Seebeck effect depends on the mechanism of interfacial spin pumping caused by a finite difference between the effective magnon temperature in the ferromagnetic material and the electron (and phonon) temperature in the NM layer [7, 8]. The first theoretical model was proposed in the context of the transverse measurement geometry [7]. This model was later modified for the LSSE geometry by Rezende and co-workers [8]. Under the application of a thermal gradient $\vec{\nabla}T$, the spin current density ($\vec{J_s}$) flowing through the interface is given by $\vec{J_s} = D_s\vec{\nabla}T$ [7]. The interfacial spin Seebeck coefficient (D_s) is given by $D_s = \gamma\hbar k_B g^{\uparrow\downarrow}/(2\pi M_s V_a)$, where γ, $\hbar$, $g^{\uparrow\downarrow}$,k_B, M_s, and V_a refer to the gyromagnetic ratio, the Planck constant, the spin-mixing conductance, the Boltzmann constant, the saturation magnetization, and the magnetic coherence volume, respectively. The functional form of V_a could be written as $V_a = \frac{2}{3\zeta\frac{5}{2}}\frac{4\pi}{K_B}(\frac{D}{T})^{\frac{3}{2}}$, where ζ is the Riemann Zeta function, and D is the spin stiffness [152]. Thus, the temperature dependence of this spin current is primarily expected to arise as a consequence of the T dependence of the magnetic coherence volume, implying that $J_S \propto \frac{g^{\uparrow\downarrow}}{M_s}(\frac{T}{D})^{\frac{3}{2}}$. This spin current flows into the Pt layer,

with a spin diffusion length λ_{Pt} and generates a charge current $\vec{J_c} = \left(\frac{2e}{\hbar}\right)\theta_{Pt} J_s \vec{\times} \sigma$ where, e, θ_{Pt}, and σ refer to the electronic charge, spin Hall angle of Pt, and spin polarization of the conduction electrons in Pt, respectively [1, 126]. The corresponding LSSE signal is determined as $V_{LSSE} = V'_{LSSE}/R_d = l_{Pt}\lambda_{Pt}\frac{2e}{\hbar}\theta_{Pt}\tanh\left(\frac{t_{Pt}}{2\lambda_{Pt}}\right) J_s$, where V'_{LSSE}, R_d, l_{Pt}, and t_{Pt} are the measured transverse voltage, the resistance across the Pt bar, length of the Pt bar, and thickness of the Pt bar, respectively [8, 43, 102]. Since $\tanh\left(\frac{t_{Pt}}{2\lambda_{Pt}}\right) \approx 1$ in our case, and with $\lambda_{Pt} \propto T^{-1}$ [153], and M_s being invariant at low temperatures, the $V_{LSSE} \propto \frac{\theta_{Pt} g^{\uparrow\downarrow} T^{\frac{1}{2}}}{D^{\frac{3}{2}}}$ - implying that the V_{LSSE} should vary as $T^{0.5}$, at-least at low temperatures. However, prior measurements on the model YIG-Pt system have revealed a linear T dependence, which has been attributed to the quadratic magnon dispersion in YIG [117], or the influence of the thermal conductivity in determining the functional form of V_{LSSE} [128].

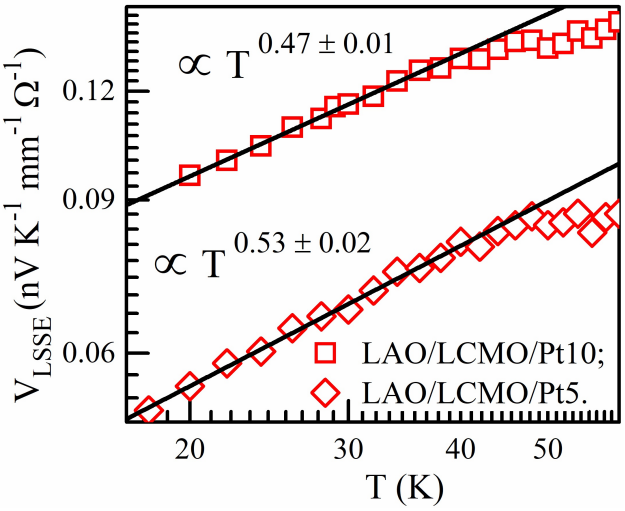

Figure 3.8: The temperature dependence of V_{LSSE} at temperatures below 60K. In the region where ΔT_{eff} remains invariant, the LSSE signal varies as 0.47 ± 0.01 and 0.53±0.02 in LAO/LCMO/Pt devices with Pt thickness of 10 nm and 5 nm respectively.

Figure 3.8 depicts an expanded view of the T dependence of V_{LSSE}, measured from both the LAO/LCMO/Pt10 and LAO/LCMO/Pt5 systems, at low temperatures in which

it is found that the V_{LSSE} varies approximately as $T^{0.5}$ - an observation which is in good agreement with the spin magnon theory. It is also observed that the LSSE exponent is nearly invariant as a function of Pt thickness. With the proximity induced ANE being reported to exhibit a pronounced dependence on the thickness of the Pt layer [154, 155], this observation also confirms that the contamination of the LSSE signals by the proximity-induced ANE should be negligibly small, and thus could be ruled out in our case.

Since the spin current is proportional to the effective temperature gradient (ΔT_{eff}) across the LCMO layer, it is important to estimate how this quantity varies in this temperature range. The ∇T_{eff} is estimated for the LAO/LCMO (or the STO/LCMO) by using the following mathematical expression:

$$\nabla T_{eff} = \frac{\nabla T_{applied}}{1 + \frac{K_{LCMO}}{K_{sub}} \frac{t_{sub}}{t_{LCMO}}} \tag{3.2}$$

where $\nabla T_{applied}$ = 10 K, t_{sub} = 0.5 mm (thickness of the LAO or STO substrate), and t_{LCMO} = 200nm (thickness of the LCMO film). K_{LCMO} and K_{sub} are the thermal conductivities of the LCMO and the substrate, respectively. Depending on the previous reports of the thermal conductivities of the both LAO single crystal [156] and the $LCMO$ material of similar composition [157], the ∇T_{eff} is estimated for the LAO/LCMO bilayer and depicted in Fig.3.9(a). It shows a narrow temperature regime, $18K \leq T \leq 32K$, where ∇T_{eff} remains invariant in temperatures. It is also found that the functional form of the V_{LSSE} obeys $T^{0.5}$ characteristic only in this regime in which ΔT_{eff} is nearly invariant, as depicted in Fig. 3.9(a) and 3.9(b). For further confirmation, we have studied the temperature dependence of V_{LSSE} on a similar LCMO film where the substrate was changed to STO − implying a possible change in the functional form

of ∇T_{eff}. The temperature dependence of the estimated ∇T_{eff} along with the V_{LSSE} are depicted in Fig. 3.9(c) and 3.9(d), respectively. The thermal conductivity of single-crystal STO is taken from the published report by M.T.Buscaglia and co-workers [158]. The STO/LCMO system shows a much narrower temperature regime, $18K \leq T \leq 24K$, where the ∇T_{eff} remains invariant in temperatures (Fig.3.9(c)). Interestingly, $V_{LSSE}(T)$ is again found to exhibit approximately $T^{0.5}$ dependence, as predicted by the aforementioned magnonic spin current model, only in the temperature regime where ∇T_{eff} is estimated to be invariant in this case as well.

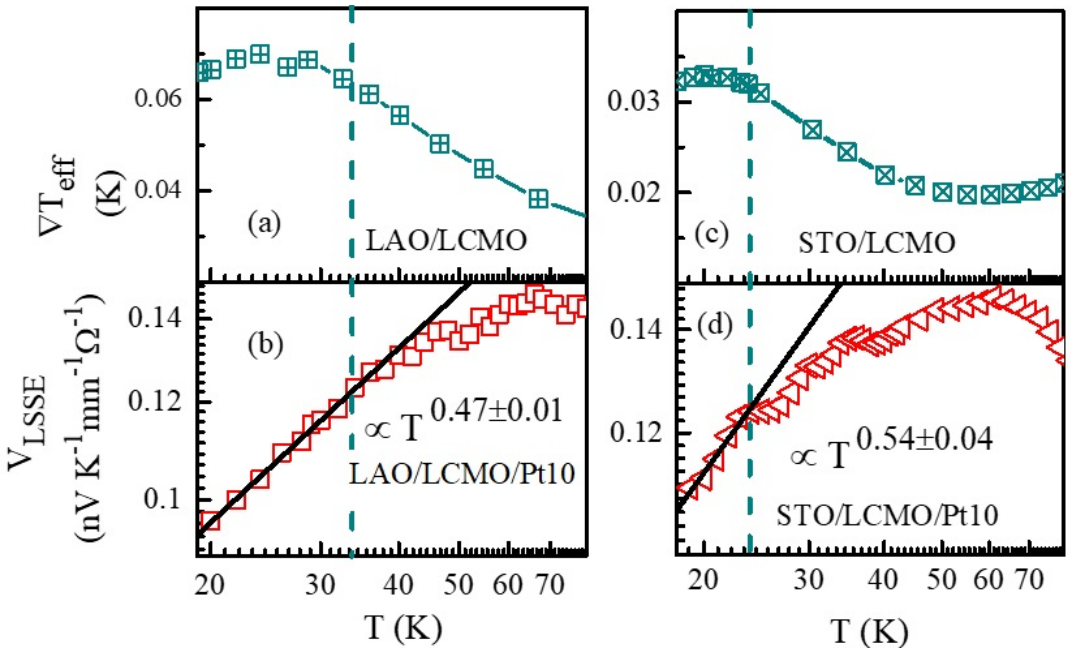

Figure 3.9: (a) & (b) show the estimation of the ∇T_{eff} for the LAO/LCMO system and the V_{LSSE} measured in the LAO/LCMO/Pt10 system, respectively. Similarly, (c) & (d) show the estimation of the ∇T_{eff} for the STO/LCMO system and the V_{LSSE} measured in the STO/LCMO/Pt10 system, respectively.

It has been suggested earlier that the low energy (or sub-thermal) magnons contribute disproportionately to the measured V_{LSSE} signal, and that phonon mediated magnon scattering needs to be explicitly considered in describing the magnitude as well

as the T and H dependence of the LSSE [130, 138, 159, 160]. In contrast, another report on YIG-Pt devices has also suggested an intimate coupling between the thermal conductivity (κ) and the measured V_{LSSE}, reinforcing the importance of phonon-mediated processes in the LSSE [128]. The fact that at higher temperatures, our V_{LSSE} signals deviate from $T^{0.5}$ indicates that an inordinate change in ΔT_{eff} across the magnetic LCMO film provides the upper bound for observing the theoretically expected functional form of V_{LSSE}.

3.5.2 LSSE near para-to-ferromagnetic phase transition

Theory and experiments have also failed to reconcile with regard to the functional form of the SSE near the magnetic phase transition. The only prior measurements on YIG-Pt devices have reported that the SSE signal varied as $(T_c - T)^3$ [4] or as $(T_C - T)^{1.5}$ [129] in the vicinity of the magnetic phase transition, while the magnetization scaled as $(T_c - T)^{0.5}$, as is expected from mean-field theory. However, previous theoretical investigations have predicted that the SSE should vary in consonance with the magnetization. For instance, an atomic numerical simulation considering the full spin-wave spectrum of the ferrimagnetic YIG predicted that both the SSE and the magnetization should have the same critical exponent [161]. In another theoretical prediction based on time dependent Ginzburg-Landau analytical calculation on a (simple single-sublattice) ferromagnet also suggested that the SSE signal should vary along with the magnetization as $(T_c - T)^{0.5}$ [162].

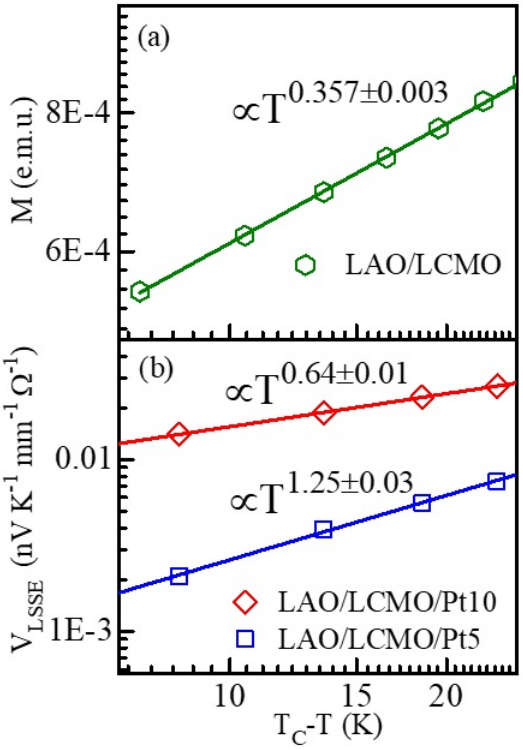

Figure 3.10: The $T_C - T$ dependence of the magnetization and the LSSE signal is depicted in (a) and (b) respectively. The critical exponent of V_{LSSE} is seen to be much larger than that of the magnetization, and also varies with the thickness of the Pt spin-to-charge conversion layer.

The temperature dependence of both the magnetization (M) and the LSSE signal (V_{LSSE}) in the vicinity of the magnetic phase transition of the LCMO are depicted in Fig. 3.10(a) and 3.10(b), respectively. The critical exponent of the magnetization is found to be 0.357 ± 0.003, which is in good agreement with previous reports [163, 164]. Interestingly, in the same region, we obtain an exponent of 0.64 ± 0.01 and 1.25 ± 0.03 for the $V_{LSSE}(T)$ with Pt thicknesses of 10 nm and 5 nm, respectively. It was speculated that the difference between the magnetization and LSSE exponents in the case of YIG/Pt could arise as a consequence of the *ferri*magnetic nature of YIG, or other considerations like the magnetic surface anisotropy [162]. Though spin-wave spectra are expected to be specific to the material, the fact that we observe a similar discrepancy between the magnetization and LSSE exponents in the case of LCMO/Pt

indicates this could be a generic feature of the LSSE signals in the vicinity of a magnetic phase transition.

3.5.3 Role of spin mixing conductance

The difference between the M and V_{LSSE} critical exponents, as observed in Fig. 3.10(a) and 3.10(b), could be a consequence of the fact that the functional form of LSSE signal is not only dependent on the static magnetization but is also influenced by the T-dependence of other factors, like, the spin mixing conductance, the spin-diffusion length and the spin-Hall angle of the NM layer [4]. Previous reports demonstrated that the intrinsic spin Hall angle of Pt is reported to be invariant in the temperature range of the LCMO transition [165, 166], and hence is unlikely to be a contributory factor. It has also been demonstrated earlier that the spin diffusion length of Pt (λ_{Pt}) is nearly invariant in the temperature range of the LCMO phase transition [153, 166]. The magnon-driven spin current density is expected to vary inversely with the magnetic coherence volume (V_a), which in turn has a $D^{3/2}$ dependence (with D being the spin stiffness co-efficient). Interestingly, it has been reported that the spin stiffness co-efficient of LCMO has an anomalous T dependence in the vicinity of the phase transition and does not fall to zero as $T \rightarrow T_c$. This is presumably due to the finite magnetic correlations in the paramagnetic phase - a hallmark of the colossal magnetoresistive manganites [167]. However, the anomalous T dependence of the magnetic coherence volume (V_a), as well as the effective temperature gradient (ΔT_{eff}) should be similar for both the films depicted in Figure 3.10(b). The fact that we observe a pronounced increase in the LSSE exponent as a function of decreasing Pt thickness suggests that the temperature dependence of the spin momentum transfer at the interface could be responsible for this anomalous temperature dependence of the LSSE signal.

Prior ferromagnetic resonance (FMR) investigations on a LCMO film of similar composition have reported a pronounced change in the FMR line-width (ΔH) across the para-ferromagnetic phase transition [168] -implying a change in the Gilbert damping(α) since $\alpha = \frac{\gamma \Delta H}{2\omega}$, with γ and ω being the gyromagnetic ratio and the microwave frequency, respectively [100, 169]. The spin mixing conductance being related to the Gilbert damping through the relation $g_r^{\uparrow\downarrow} = \frac{4\pi M_S d_f}{g\mu_\beta}\Delta\alpha$ (with M_S, d_f and g being the spontaneous magnetization, film thickness and the Lande's g factor respectively) [100, 169, 170], would thus be expected to have a significant influence on the observed V_{LSSE} exponent. Interestingly, previous reports have also revealed that the effective $g_r^{\uparrow\downarrow}$ (or $\Delta\alpha$) depends on parameters like the quality of the interface [171] and the thickness of the Pt layer [172–174]. Since we observe a two-fold increase in the V_{LSSE} exponent as a function of decreasing Pt thickness, it suggests that $g_r^{\uparrow\downarrow}(T)$ plays a critical role in determining the functional form of V_{LSSE} in the vicinity of the magnetic phase transition. This temperature dependence of the spin mixing conductance could also probably explain why our measured $V_{LSSE}(T)$ matches well with the magnon-driven spin current model in the low-T regime, whereas model systems like YIG-Pt do not exhibit this behavior. Recent ferromagnetic resonance (FMR) measurements on YIG have indicated a pronounced T-dependence of the FMR linewidth (ΔH) [175, 176], implying a change in the Gilbert damping(α) and consequently the spin mixing conductance at low temperatures. On the other hand, early FMR measurements on $La_{0.7}Ca_{0.3}MnO_3$ have indicated that ΔH is relatively T independent below 100K [168], suggesting that it is this relative T invariance of the spin mixing conductance and other terms that allows us to observe the theoretically predicted $T^{0.5}$ dependence of $V_{LSSE}(T)$ in the low temperature regime.

3.6 Conclusion

In conclusion, we describe investigations of the temperature dependence of the LSSE in an optimally doped $La_{0.7}Ca_{0.3}MnO_3$ system. After disentangling the ANE contribution, we observe that in the low T regime, $V_{LSSE}(T)$ varies as $T^{0.5}$, as is expected by the magnon-driven spin current model. In the para-to-ferromagnetic transition region, the LSSE exponent is found to be much larger than that of the magnetization. This could be generic to most of the phase transitions of this nature. Interestingly, this exponent is also found to vary with the thickness of the Pt layer, indicating that a temperature-dependent spin mixing conductance plays an important role in the measured $V_{LSSE}(T)$. Our observations reinforce the need to individually ascertain the T dependencies of contributory mechanisms − especially the spin mixing conductance − which play a role in dictating both the magnitude of spin current as well as the extent of spin to charge conversion to understand the temperature-dependent LSSE in strongly correlated materials.

Chapter 4

The anomalous Nernst effect in a Ni-Mn-Ga system

Ni-Mn-Ga Heusler system is well-known as an important functional material that shows significant magnetic shape memory effect (MSME). Upon cooling, such a material undergoes many sequential phase transitions, sensitive to their compositional variations. This chapter describes the detailed investigation of the $Ni_{1.96}Mn_{1.04}Ga$ system through various magnetic, electronic, and thermal characterizations. The anomalous Nernst effect (ANE) is primarily investigated, and it is observed that the ANE is extremely sensitive to all those sequential transitions. In particular, a pronounced change in the ANE signal is observed across the pre-martensitic phase of this material, whereas, in contrast, such a change in other transport and magnetic measurements remains faint. With the ANE being sensitive to changes at the Fermi surface, we have discussed the possible coupling between local magnetism and the change in the Fermi surface associated with the structural modulations.

4.1 Introduction

The Ni_2MnGa Heusler alloy and its near stoichiometric compositions has received tremendous attention as an important functional material due to its substantial magneto-caloric [177, 178], magneto-resistive [179], and magnetic shape memory effects (MSME) [180, 181]. To date, many experimental and theoretical investigations have been focused on understanding the complex interplay of its structural, magnetic, and electronic degrees of freedom. Besides its fundamental importance, the generation of large magnetic field induced strain (MFIS), that can exceed 11% in some systems [182, 183], enhances its importance as a potential candidate for the development of efficient magneto-mechanical actuators. The stoichiometric Ni_2MnGa has been widely used as a model system, and previous reports confirmed the sequential transitions in this material, where all the phases below the Curie temperature, $T_c \approx 376$K, are ferromagnetic in nature [184, 185]. At room temperature, Ni_2MnGa has a cubic $L2_1$ crystal structure ($a = 5.825$Åand space group $Fm\bar{3}m$), which is referred to as the austenite phase [185]. Upon cooling, it transforms to the martensitic phase at $T_M \approx 210$ K via an intermediate pre-martensitic transition (PMT) which occurs at $T_{PM} \approx 260$K [185–187]. In general, the pre-martensitic phase is considered to be a precursor state of the low temperature martensite phase with preserved cubic phase symmetry having a long period modulated structure[185, 186]. The modulations originates from a periodic shuffling of the (110) planes along the $[1\bar{1}0]$ direction with a periodicity of six atomic layers, also called the 3-fold or 3M modulation [188–190]. On the other hand, the crystal structure of the martensitic phase is still under debate between the body-centered tetragonal [184, 191] and the orthorhombic [185, 187, 189] unit-cell structures. Even though it possesses

extended structural modulation, the magnitude of such modulation also remains debatable between the 7M [185, 187, 192] and the 5M [191, 193] modulations. Nonetheless, prior reports suggest that the large magnetic field induced strain of Ni_2MnGa is closely linked with the modulation of the martensite phase [182, 194], where it appears through the modulated premartensite phase [186, 189, 195]. Here we note that, since the PMT offers such modulations by maintaining the same lattice parameters of the austenite phase, the premartensitic phase is considered as a perfect arena for the investigation of the possible cause and/or effects of such modulations [196]. It is especially important since the microscopic mechanism of such modulations, as well as its possible link to both the MSME and ferromagnetism, remain in ambiguity. However, most of the conventional experimental tools are relatively insensitive across the PMT – limiting the flexibility of various investigation processes for addressing the issues associated with these modulations.

A volume of investigation has been detailed in the literature, describing the modulated structure of both the martensite and the premartensite phases. It is presently well-understood that all such modulations are incommensurate type [186, 187, 192]. A systematic study on off-stoichiometric $Ni_{2+x}Mn_{1-x}Ga$ has shown that both the premartensitic and the martensitic transitions are very sensitive to compositional variations of the alloy [197–199]. Here, we discuss the detailed investigation of a near stoichiometric $Ni_{1.96}Mn_{1.04}Ga$ system through various kinds of magnetic, electronic, and thermal measurements. In particular, the ANE is investigated for the first time in this Ni-Mn-Ga class, depicting a substantial sensitivity in the premartensite phase in comparison to other transport, as well as magnetization measurements. Our ANE data also suggests a possible coupling between the local magnetism and the Fermi surface of the specimen. Our investigation clearly shows that the ANE could be utilized as a

powerful tool to probe the effects associated to the minute changes in the Fermi surface.

4.2 Sample preparation

The polycrystalline Ni-Mn-Ga sample was prepared by the conventional arc-melting method using the appropriate quantities of each constituent. The sample was melted several times to get uniform composition, and finally, the melted ingot was annealed in evacuated quartz ampoule at temperature 1100K for 3 days to achieve further homogeneity and then quenched in the ice water mixture. For compositional analysis, a small piece from the annealed ingot was evaluated using energy dispersive x-ray analysis. This data was collected at different regions of the sample, and the average composition was found to be $Ni_{1.96}Mn_{1.04}Ga$ (hereafter termed as Ni_2MnGa). The phase of the sample is characterized by the X-Ray diffraction (XRD) experiment, carried out at the room temperature. Both the sample preparation and the X-Ray characterization was carried out by Dr. Sanjay Singh and his group members from IIT-BHU, India. The Rietveld refinement of the room temperature XRD data confirms that the sample is in the single phase, with the cubic $L2_1$ crystal structure under the space group of $Fm\bar{3}m$.

4.3 Magnetic measurements

The temperature dependent static magnetization ($M(T)$) was measured at different magnetic fields of 100 Oe, 500 Oe, and 2000 Oe. Each $M(T)$ measurement is taken in the temperature range of 4K to 398 K by using a vibrating sample magnetometer (Quantum Design, PPMS) in both the field cooled cooling (FCC) and the field cooled warming (FCW) modes. In the FCC-mode, the sample is first heated above the Curie temperature

(T_C) and after that the magnetic field is applied and then measurement is performed during cooling of the sample temperature. After achieving the lowest sample temperature, magnetization measurement in the FCW mode is performed, where the magnetization is measured during warming of the sample temperature in the same magnetic field. Figure 4.1(a) illustrates the temperature dependence of static magnetization ($M(T)$) of our sample at a low applied magnetic field (100 Oe), which confirms the sequential phase transitions in this alloy as reported in the literature[189]. Upon cooling, the para-to-ferromagnetic, the austenite-to-premartensite, and the premartensite-to-martensite transitions are observed at 383K (T_C), 233K (T_{PM}), and 167K (T_M) respectively. During warming, all those transitions again appear in the reverse sequential order with a clear thermal hysteresis at both the martensite and premartensite phase transitions, which is also a characteristic of these transitions [189, 200–203].

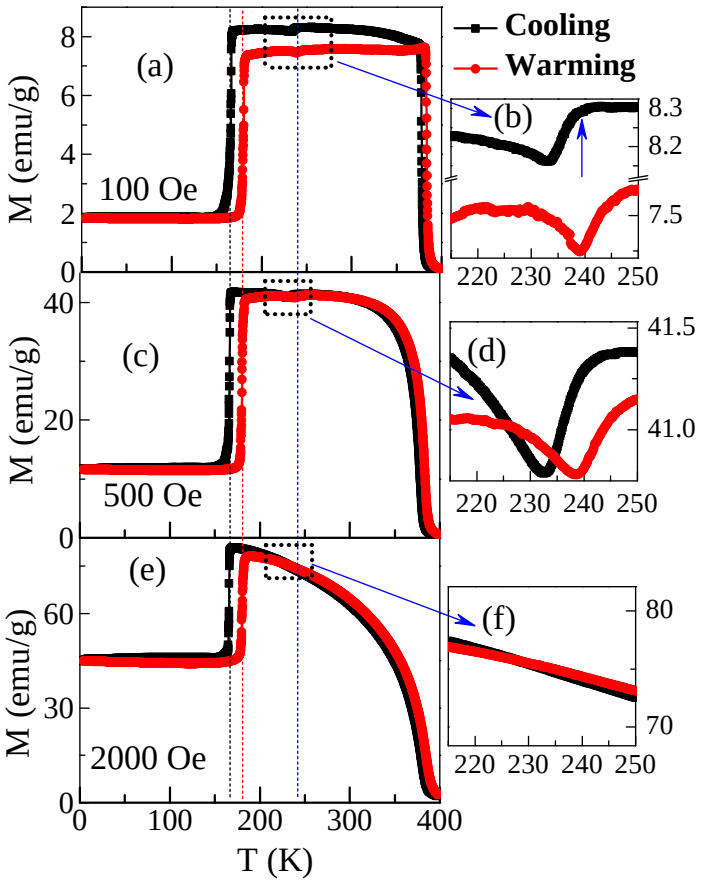

Figure 4.1: Temperature dependence of DC-magnetization at magnetic field of (a) 100 Oe, (c) 500 Oe, and (e) 2000 Oe − whereas (b), (d), and (f) are illustrating a magnified part of the respective $M(T)$ plot around the premartensitic transition. The blue dotted line is guiding to show the premartensitic transition, and similarly the red dotted line (or the black-dotted line) is guiding the martensitic transition during warming (or cooling)

.

In comparison to the previous reports on stoichiometric Ni_2MnGa [184, 185, 204], the present composition ($Ni_{1.96}Mn_{1.04}Ga$) of our sample shows that both the T_{PM} and the T_M shift to lower temperatures, which could be due to slight variation in Ni and Mn content. These results are in good agreement with the reported phase diagram [197, 198]. Figure 4.1(c) and 4.1(e) depict the temperature dependence of magnetization $M(T)$, measured at two different higher magnetic fields of 500 Oe and 2000 Oe, respectively. Figure 4.1(c) depicts a small shift (around 1K) in the T_{PM} at a lower temperature

in comparison to the low field (100 Oe) data of the $M(T)$. Moreover, the anomaly in the $M(T)$ plot across the premartensitic transition is suppressed by higher magnetic field as observed from Figure 4.1(a), 4.1(c), and 4.1(e). Such an anomaly in $M(T)$ is almost completely suppressed at a magnetic field of 2000 Oe, which is depicted in Figure 4.1(e). The suppression of such anomaly in the $M(T)$ data across the premartensitic transition as well as the decreasing nature of T_{PM} with increasing the magnetic field is attributed to emergence of magnetoelastic coupling in the premartensite phase, and this is consistent with previous reports [195, 202–204]. Figure 4.1(b), 4.1(d), and 4.1(f) depict a clear view of the magnetization-plots around the premartensitic transition (guided by blue arrows), which are basically the magnified version of the $M(T)$-curves shown in Figure 4.1(a), 4.1(c), and 4.1(e), respectively. The blue arrow in Figure 4.1(b) shows the premartensitic starting temperature (T^s_{PM} around 238K) during cooling.

4.4 Transport measurements

Apart from magnetic measurements, both the premartensitic and the martensitic transitions are also observed in various transport measurements. Temperature dependence of resistivity ($\rho(T)$), thermal conductivity ($K(T)$), and the longitudinal Seebeck coefficient ($S_{xx}(T)$), measured in the absence of magnetic field, are depicted in Figure 4.2, 4.3, and 4.4, respectively. Here, the $\rho(T)$ is measured at an applied magnetic field of 2 kOe, whereas the $S_{xx}(T)$ and the $K_{xx}(T)$ are measured in the absence of a magnetic field.All the $\rho(T)$, $K(T)$, and $S_{xx}(T)$ plots suggest that the sensitivity of all these conventional transport measurements are quite faint across the pre-martensitic transition. Nonetheless, the $\rho(T)$ curve confirms the metallic behaviour of the sample. Similarly, the dominating contributions of the electron-type carriers at the longitudinal

thermopower is also confirmed by the negative sign of the $S_{xx}(T)$ in the whole temperature range.

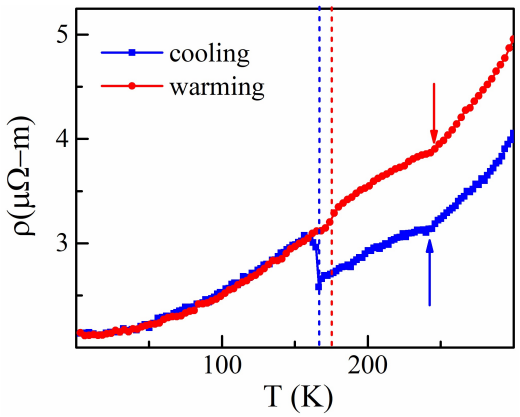

Figure 4.2: Temperature dependence of the resistivity, measured during warming (red-circle) and cooling (blue-square) of the sample temperature. The blue dotted line (or the red-dotted line) is marked at the martensitic transition temperature during cooling (or warming) of the sample temperature. Similarly, the blue arrow (or the red arrow) is marked at the pre-martensitic transition temperature during cooling (or warming) of the sample temperature.

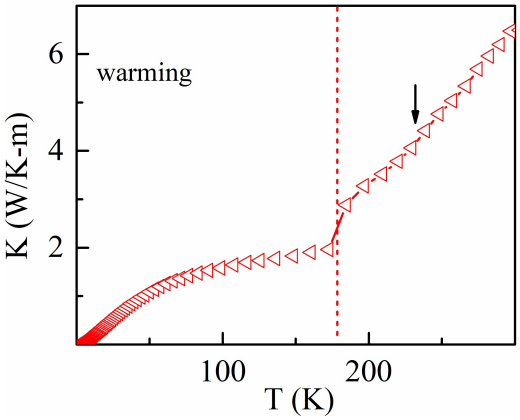

Figure 4.3: Temperature dependence of thermal conductivity ($K(T)$), measured during warming the sample temperature. The dotted line is marked at the martensitic transition, whereas the black arrows is marked the pre-martensitic transition in the $K(T)$ plot.

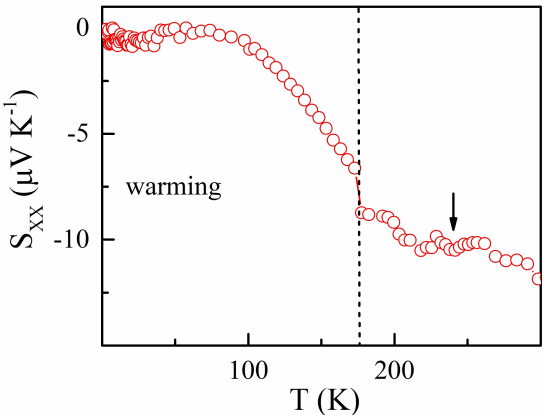

Figure 4.4: Temperature dependence of Seebeck coefficient ($S_{xx}(T)$), measured during warming the sample temperature. The dotted line is marked the martensitic transition and the black arrows is marked at the premartensitic transition in this $S_{xx}(T)$ plot.

.

4.4.1 ANE measurements

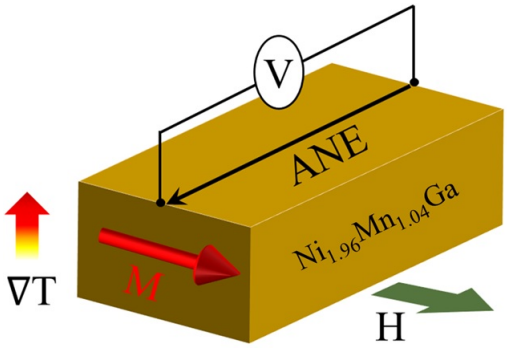

Figure 4.5: Device geometry for the measurement of ANE.

.

The ANE or anomalous Nernst effect pertains to the generation of a transverse electrical voltage (V_t) orthogonal to both the $\vec{M}$ and the applied thermal gradient ($\vec{\nabla}T$) across a magnetic metal – where, the $\vec{\nabla}T$ acts as a driving force, analogous to an electric bias causing anomalous Hall effect [9, 10]. In mathematical language, it can be described

by an empirical formula:

$$V_t = S_{xy}\vec{M} \times \vec{\nabla}T \tag{4.1}$$

where S_{xy} is defined as the transverse Seebeck coefficient [10, 11, 205]. The measurement protocols of the V_t are mentioned in Chapter 1 of this thesis. Figure 4.5 illustrates the geometry of our device, where the polycrystalline sample is cut and polished to form a rectangular slab of dimensions $7 \times 3 \times 1\ mm^3$. The $\vec{\nabla}T$ is applied across the width (l_z = 1 mm), and the magnetic field (H) is applied along the breadth (l_x) of the sample. Therefore, the transverse ANE-voltage (V_t) is measured along the y-direction by using two gold wires, attached at the same surface of that rectangular slab at a distance of 3.6 mm (l_y) apart.

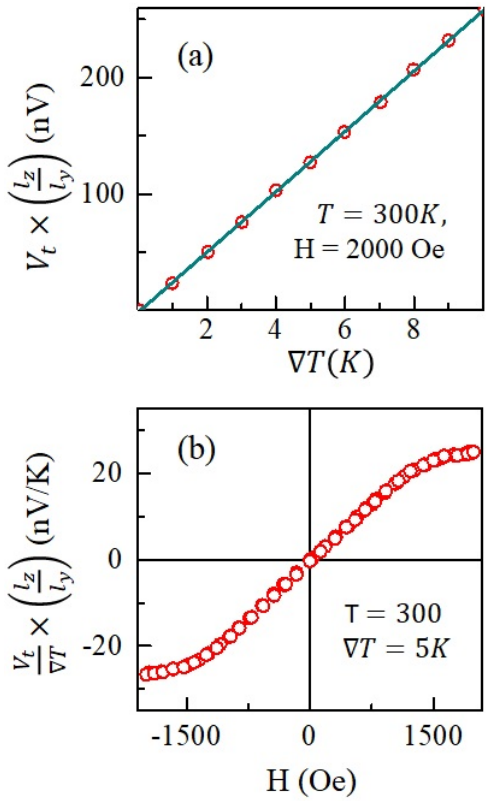

Figure 4.6: (a) illustrates the ∇T dependence of the ANE-signal. (b) shows the magnetic field dependence of V_{ANE} signal, measured at room temperature with ∇T = 10K.

Figure 4.6(a) depicts the linear dependence of V_t on the applied ∇T, where the cold-end of the sample is fixed at 300K, and the applied magnetic field is kept fixed at 2000 Oe. The linearity of the V_t vs. ∇T-plot along with zero intercept confirm the absence of any thermal loss in our measurement. Figure 4.6(b) shows the magnetic field dependence of the ANE signal, where average sample temperature (T_{av}) is at $300K$ and the ∇T = 10K. Both Figure 4.6 (a) and (b) confirm the observation of ANE signal from our Heusler specimen.

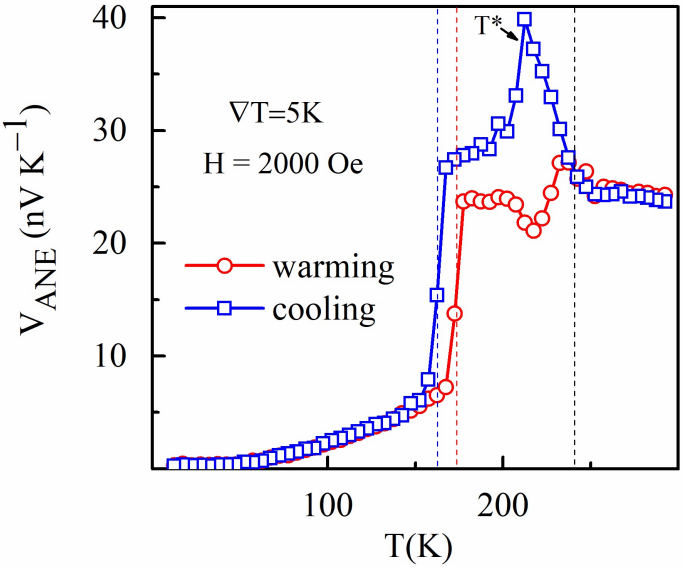

Figure 4.7: depicts the temperature dependence of the ANE signal, $V_{ANE}(T)$ where the ∇T = 5K and H = 2000 Oe are kept fixed.

.

Figure 4.7 illustrates the temperature dependence of the normalized ANE-signal, $V_{ANE}(T) = \left(\frac{l_z}{l_y \nabla T}\right) V_t(T)$, where both the $\vec{H}$ and the $\vec{\nabla} T$ are kept fixed at 2000 Oe and 5K, respectively. It is worth mentioning that the average sample temperature is determined by $T_{av} = \frac{1}{2}(T_1 + T_2)$, where the $\mid \vec{\nabla} T \mid = \nabla T = T_2 - T_1$, where T_1 and T_2 are the temperatures at cold-end and hot-end of the sample, respectively.

A large ANE-signal is observed at room temperature. In agreement with the previous reports on Heusler alloys [11], the present Ni-Mn-Ga system also shows a significant drop in the $V_{ANE}(T)$-signal across the martensitic transition. Another important observation is that the $V_{ANE}(T)$ turns out to be very sensitive across the premartensitic transition, even though such anomaly in the $M(T)$ curve across the premartensitic transition is insignificant at this field of 2000 Oe. Therefore, from equation 4.1, it is suggested that consideration of the characteristic of the S_{xy} is important for further understanding of the ANE signal.

4.5 Discussion

The origin of ANE is well understood in the picture of an effective spin-orbit interaction − which is further decomposed into three different mechanisms, like, Berry curvature effect, side jumping, and skew scattering mechanisms [9, 10]. The origin could also be understood in terms of the Mott's relation, which gives the link between the transverse thermoelectric coefficient (α_{xy}) and the transverse electrical conductivity (σ_{xy}). It is given by the following relation:

$$\alpha_{xy} = \frac{\pi^2 k_B^2 T}{3e} \times \left(\frac{\partial \sigma_{xy}}{\partial E}\right)_{E_F} \tag{4.2}$$

where k_B, e, E, and E_F are the Boltzmann constant, charge of an electron, energy of the conduction electrons, and the Fermi energy of the sample, respectively [9–11, 205]. Thus, α_{xy} depends on both the temperature and the slope of the σ_{xy} tensor with the Fermi-surface, or $\left(\frac{\partial \sigma_{xy}}{\partial E}\right)_{E_F}$. Therefore, the S_{xy}, being linked to α_{xy} through the relation: $S_{xy} = \rho(\alpha_{xy} - \sigma_{xy} S_{xx})$ [10, 11, 205], also becomes sensitive to the changes in

the Fermi surface. Interestingly, a previous report has also claimed such sensitivity of the Nernst signal on the Fermi-surface distortions [89].

The large MFIS of the Ni_2MnGa is intimately linked with the existence of a long periodic modulation in the microscopic structure of the sample. However, the origin of those modulations is still under debate − and there are two diverse scenarios referred to as its possible mechanisms. One of them is the Adaptive model, where the modulation is portrayed as an effective twinning emerging from the minimization of elastic energy [191, 206]. The other one is the soft-phonon mode-based displacive modulation model. The latter has received more theoretical and experimental support [188–190, 207–213], where a change in the Fermi surface (in terms of nesting of the Fermi surface) appears as an imperative outcome of the phonon softening.

Despite these debates, it is worth mentioning that previous neutron scattering experiments have confirmed the signature of phonon softening [188, 190, 207] and the phasons [208] associated with the charge density wave (CDW) resulting from the Fermi surface nesting at both the premartensite and the martensite phases. The high-resolution X-ray diffraction studies also revealed the non-uniform atomic displacements in the modulated phase, phason broadening in satellite peaks, and a temperature variation of modulation wave vector without any commensurate lock in the phase [187, 189]. Recently, another experiment based on the photoemission spectroscopy has also confirmed the occurrence of CDW at the onset of the premartensitic transition [209], which is again associated with the phonon softening or the Fermi surface nesting. Finally, a recent electron-positron annihilation experiment has confirmed the nesting features of the Fermi surface in the premartensite phase of the Ni_2MnGa specimen[214]. So, based on these findings, it can be argued that the significant sensitivity of the ANE-signal across the premartensite phase (in Fig. 4.7) is presumably due to the change in

the Fermi surface via its nesting features, which occurs at the onset of the premartensitic transition (T_{PM}). It is also important to note that there is also a finite possibility for an additional contribution of the σ_{xy} alone due to its crucial connection to the S_{xy}. However, with $\rho_{xy} \propto M\rho^n$, where ρ_{xy} is the Hall resistivity and n is a number that typically varies within 0 to 2 [9, 10, 85, 88] – the solitary role of the σ_{xy} for the large anomaly in the $V_{ANE}(T)$ around the T_{PM} would be negligible since both the $M(T)$ & $\rho(T)$ are faint across the premartensitic transition. In support, a prior report on the Hall measurement in a Ni-Mn-Ga thin film shows that Hall signal is quite insensitive to both the premartensitic and the martensitic transitions [215]. Thus, ANE could be another evidence in support of the phonon softening model. Interestingly, previous reports also suggest such sensitivity of ANE signal in a CDW state [216–218]. It also is worth mentioning that the nesting feature does also exist in the martensite phase too [212–214] – however, its impact on the ANE signal can not be evident because of the structural transformation associated with the martensitic transition which also results in a substantial drop in the magnetization.

Apart from T_{PM} and T_M, the $V_{ANE}(T)$ also depicts another characteristic temperature T^* – well below the onset of premartensitic transition – across which, a significant change in the V_{ANE} is also observed, as shown in Fig.4.7. A possible explanation could be inferred that during cooling the ANE voltage starts to change (rise) around 238K (onset of premartensitic transition) as a consequence of the change in electronic state of the system at this starting point of premartensite phase transition. The ANE-voltage continues to rise with the appearance of the premartensite phase until it encompasses the entire sample space, i.e., the occurrence of nesting of the Fermi surface evolves until T^*. Below this temperature, the $V_{ANE}(T)$ starts to decrease as a function of decreasing sample temperature – a phenomena that could be understood from the Mott's relation

described in equation 4.2. Although, such a sharp change in the ANE-signal across the T^* hints the appearance of local traces of the martensite phase inside the premartensite regime just below T^* (around 210K), resulting in a further modification of the Fermi surface. Previous NMR experiments have clearly revealed such temperature regime in between the T_M and T_{PM}, where both the premartensite and the martensitic phase do coexist[210]. On further cooling, the main martensitic transition occurs, which is also observed in all the measurements, characterized by T_M. A reasonable thermal hysteresis in the $V_{ANE}(T)$ is also observed across both the martensitic and premartensitic transitions. The nature of the $V_{ANE}(T)$ seems to vary differently during the cooling and warming cycles – and, we interpret such differences as a reconstruction of the Fermi surface during cooling and warming through the premartensitic phase.

4.5.1 Role of coupling between the local magnetism and the Fermi surface

The Mott relation certainly explains the ANE-signal; however, it also suggests that the $S_{xx} \propto (\frac{\partial \sigma_{xx}}{\partial E})_{E_F}$ [9–11] – implying that it should also be sensitive across the premartensite phase, whereas it does not seem so according to the Figure 4.4. A possible explanation could be the role of the externally applied magnetic field. In the S_{xx}, where the measurements are taken in the absence of an external magnetic field, an additional sizeable electronic background of the unchanged Fermi surface dominates over the role of weak nesting at this premartensite phase. On the other hand, the ANE only picks up the change due to the magnetic field, where the substantial background is ultimately subtracted by reversing the magnetic field – although, such a significant change across the T_{PM} is almost invisible in the $M(T)$ data measured at a field of 2000 Oe. Previously, such phenomena of ANE that are beyond the magnetization scaling is explained with

the role of effective Berry curvature [219, 220], where the form of the sample, used for the measurements, is a single crystalline specimen. As our sample is a polycrystalline slab, the role of effective Berry curvature is very unlikely to be present in our observations. In another possibility, that could occur in this premartensite phase, is to have some level of coupling between the local magnetism and the Fermi surface – so that, it can add an extra contribution to the measured V_{ANE} by the changes in the Fermi surface due to the application of external magnetic field. Recently, G. Lantz and co-workers also have inferred about such a coupling in their pump-probe experiments on the stoichiometric Ni_2MnGa sample [196]. This coupling might help in understanding the link between the magnetic field and the structural modulation, which is so called the MFIS. Interestingly, a previous theoretical work also predicts that the premartensitic transition is driven by the magnetoelastic interaction (or by the MFIS) [195]. Thus, in short, the aforementioned coupling can provide a much deeper insight into this class of materials.

4.6 Conclusion

In conclusion, we present a detailed investigation of a near stoichiometric Ni-Mn-Ga sample, which shows all the sequential transitions that occur in the line of the reported phase diagram. Across the premartensitic transition, a predominant suppression of the anomaly in the $M(T)$ curve is observed at a higher magnetic field – suggesting the occurrence of magnetoelastic effect in this premartensitic phase of this material. The ANE is investigated for the first time in this Ni-Mn-Ga class of materials, and it clearly shows the substantial sensitivity across the premartensitic phase in contrast to other conventional transport measurements, like, $\rho(T)$, $K(T)$, and $S_{xx}(T)$. With the ANE being sensitive to changes in the Fermi surface, we suggest that such sensitivity of the

$V_{ANE}(T)$ is due to the changes in the Fermi surface − which further supports the soft phonon based model. Finally, tallying the $V_{ANE}(T)$ with both the $M(T)$ and the $S_{xx}(T)$, we also suggest the possibility of some level of coupling between the local magnetism and the Fermi surface, which could have significant implications in understanding such potential functional materials. Finally, we conclude that the ANE could be utilized as a powerful tool for further investigations on various different magnetic shape memory alloy systems having different compositions and/or forms, like, single crystals or thin films.

Chapter 5

The magnon Hall effect in single crystalline $Y_2V_2O_7$

The discovery of the magnon Hall effect (MHE), driven by the Berry curvature of the magnon bands, has been a significant advancement in the field of Spintronics. In this chapter, we report on our investigation of the MHE in a single crystalline $Y_2V_2O_7$ specimen. In particular, we quantify the thermal Hall effect of magnons along two different orientations of the crystal, {100}, and {111}, by putting a thin non-magnetic metal-layer on top of the [100] or [111] plane of that crystal. Our observation reinforces the need to individually ascertain the contributions of all the magnon-bands in quantifying the Hall response of magnons. A possible role of the Weyl magnon is also discussed in determining the observed thermal Hall signals. Additionally, the measurements from the crystals oriented along the {111} plane are found to display a significant magnon drag effect at the interface. By considering the theoretically predicted magnon band structure of the pyrochlore ferromagnets, we link the magnon drag effect with the chiral surface state of magnons.

5.1 Introduction

The Hall effect pertains to the generation of a transverse electric current on the application of the longitudinal electric field. In the case of ordinary non-magnetic metals (e.g., Cu or Al), it is well described in terms of the Lorentz force proportional to the applied magnetic field, that deviates the moving charged particle into the transverse direction. However, in a magnetic material, there is an additional contribution due to the associated magnetization causing the anomalous Hall effect (AHE) [85, 87]. A thermal analogue of the anomalous Hall effect is known as the anomalous Nernst effect (ANE)− where the driving force is the applied thermal gradient instead of the electric field [10, 88]. A series of investigations have revealed that the origin of the ANE (or the AHE) could be explained in terms of an effective spin-orbit interaction− which is further decomposed into three different mechanisms, namely, Berry curvature effect, side jumping, and skew scattering mechanisms [9, 10, 85, 87, 88]. Among them, the Berry curvature effect is also recognized as an intrinsic effect, originating from the band structure of the material, and is thus protected by the symmetry of the specimen [78, 81, 82, 87, 221–223]. For instance, in recent experiments, the Berry curvature driven anomalous Hall transport of electrons were demonstrated in terms of ANE [219, 220]. Since the Berry curvature effect is not restricted only to electrons, a similar effect is also expected in other types of particle systems as well. Prior experimental investigations have also confirmed the Hall transport of photons [224, 225], phonons [55, 56, 226], and magnons [12, 15] − where these particles, even though they are charge-neutral, are influenced by the effective Berry curvature of their energy-bands giving rise to an intrinsic Hall transport.

Magnon Hall effect (MHE), a relatively new topic in the context of Berry curvature effect, has earned a lot of attention due to its fundamental importance to the field of spintronics. In 2010, H. Katsura et al. first introduced a theoretical description of MHE in the context of the thermal Hall effect of magnons (THEM) − where the transverse thermal current is carried by magnons [111]. First experimental demonstration was performed by Y. Onose and co-workers, where the THEM was observed in a pyrochlore single crystal of $Lu_2V_2O_7$ specimen [12]. In prior experiments, the THEM was demonstrated in terms of the transverse thermal conductivity (K_{zx}) − where the K_{zx} was studied as a function of the applied magnetic field (H) and temperature (T) that confirmed magnons as the carrier of the transverse thermal current [12, 15]. It is worthwhile to mention that the K_{zx} is estimated by measuring the transverse thermal gradient (∇T_{zx}) in a direction orthogonal to both the applied thermal gradient (∇T_{zz}) and the external magnetic field (H) [15]. In this chapter, we report the observations of THEM in single-crystalline $Y_2V_2O_7$ specimens, where the measurements are performed in two different crystals whose planes are cut and polished into two different orientations, {100} and {111}. Unlike the previous experimental detection method [12, 15], we measure the ∇T_{zx} by putting a thin non-magnetic normal metal (NM), like, Pt, or W, on top of the crystal's plane. The THEM is then quantified in terms of thermopower, generated along the length of the NM-bar (also called as the detection layer). In contrast to prior reports, where the ∇T_{zx} was directly measured by utilizing thermocouples [12, 15], our method significantly improves the signal to noise ratio. The detailed investigation on the $Y_2V_2O_7$ crystals reveals that a significant part of the observed THEM signal is contributed by the magnons of the higher energy bands. This is in contrast to the previous report, where the contribution of the lowest magnon-band

was considered to have a solitary role in dictating the THEM-signal [12, 15]. Additionally, the crystal with {111} planes is observed to display a significant magnon drag effect at the interface with the NM layer – which is further linked to the topologically protected chiral surface state of magnons.

5.2 Sample Preparation

The single crystal of $Y_2V_2O_7$ were grown by Dr. Dharmalingam Prabhakaran from the University of Oxford, UK. All the crystals were cut and polished into two sets of two different orientations. The first set was oriented along {100} planes, and the other one along {111} planes. Hereafter, the crystal with {100} orientations will be mentioned as YVO[100], and that with {111} orientation will be mentioned as YVO[111]. For the detection of ∇T_{zx}, we deposited a thin non-magnetic NM-bar, like, Pt or W, on top of the crystal surface by using the DC magnetron sputtering technique. Figure 5.1 depicts the device geometry of the measurements.

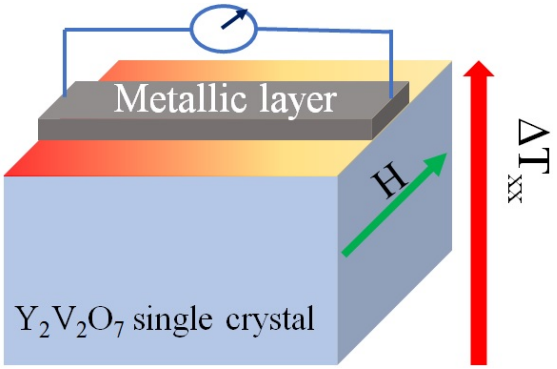

Figure 5.1: Device geometry to measure the THEM signal, where the generated transverse thermal gradient is measured by the attached metal bar.

Depending on both the choice of crystal and the choice of NM layer, four different types of devices are made: YVO[100]/Pt, YVO[100]/W, YVO[111]/Pt, and YVO[111]/W.

The thickness of both the Pt (t_{Pt}) and W (t_W) layers are maintained at 10nm. The dimensions of the YVO[100] and the YVO[111] crystals are (I) 3 mm × 2.5 mm × 1 mm, and (II) 4.5 mm × 2 mm × 1 mm, respectively.

5.3 Results and discussions

5.3.1 Magnetic and electronic characterization

The magnetic and electronic transport characterization of both the YVO[100] and the YVO[111] crystals are described below.

Temperature dependence of the magnetization (M-T), with $H \parallel [100]$ and $H \parallel [111]$, are depicted in Fig. 5.2 (a) and (b), respectively. The M-T measurements are performed in conventional zero-field cooled (ZFC), as well as field cooled (FC) mode, where a magnetic field of 100 Oe is applied during each measurement. Both M-T plots illustrate the ferro-to-paramagnetic transition at $T_c \approx 70$ K.

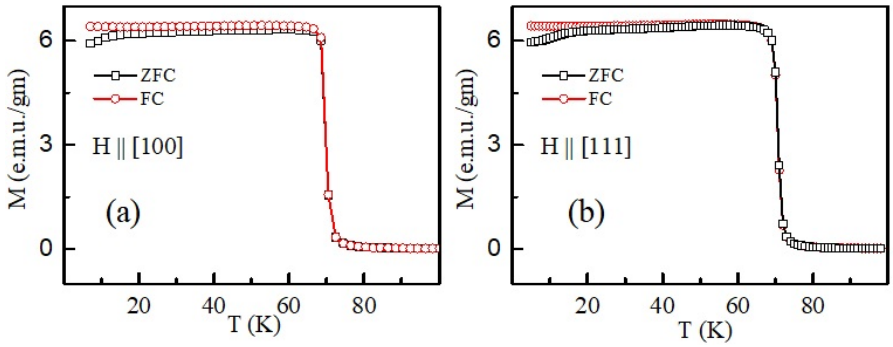

Figure 5.2: Temperature dependent magnetization as measured from (a) YVO[100], and (b) YVO[111] crystals.

Magnetic field dependence of the magnetization (M-H) of both the YVO[100] and YVO[111] crystals are depicted in Fig. 5.3, where the direction of the magnetic field is kept along the [100] and the [111] planes, respectively. Here, the sample temperature is

kept fixed at 15 K.

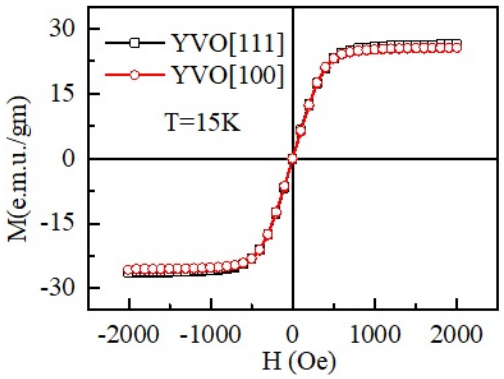

Figure 5.3: Magnetic field dependent magnetization as measured from (a) YVO[100], and (b) YVO[111] crystals. The sample temperatures are maintained at 15 K.

The temperature-dependence of the resistance, measured across the YVO[100] sample, is depicted in Fig.5.4. It clearly shows the specimen's insulating nature. In the inset of the Fig. 5.4, the first derivative of the measured resistance is shown to illustrate the occurrence of phase transition across T_c.

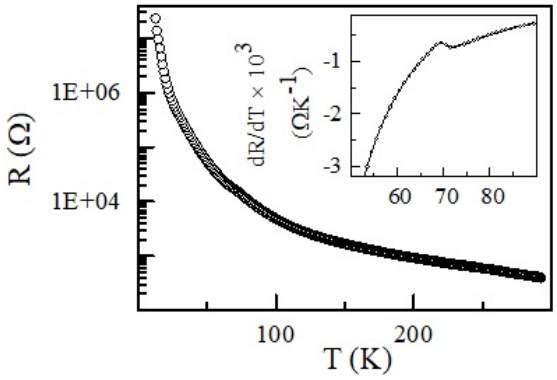

Figure 5.4: Temperature dependent of the total resistance, as measured from YVO[100]. In the inset, first derivative of the measured resistance is depicted to show the insulator-to-insulator transition at T_c.

Prior reports confirmed that the structural, magnetic, and electronic properties of the pyrochlore $Y_2V_2O_7$ are quite similar to that of the $Lu_2V_2O_7$ specimen [227–229].

Since $Lu_2V_2O_7$ is a well-known material that offers a significant MHE, a similar effect is also expected in a single crystalline $Y_2V_2O_7$ specimen. The magnetism in these materials is driven by the V^{4+} ($3d^1$, $S = 1/2$) sub-latices, which share their corners to form a corner-sharing Vanadium tetrahedron [12, 229]. This structure could also be viewed as the stacking of alternative Kagomé and triangular lattices along the [111] direction, as depicted in Fig. 5.5.

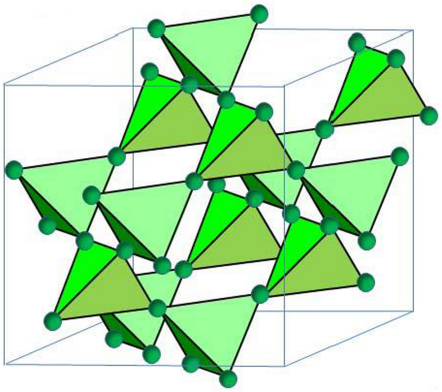

Figure 5.5: depicts a pyrochlore crystal structure [12]. In our case, the V^{4+} latices are sitting at the corner of each tetrahedron, forming the magnetic structure of the $Y_2V_2O_7$ crystal. The [111]-direction is along the body diagonal of the surrounding cube. The figure is adapted from Ref.[12], and reprinted with permission from AAAS.

Since the midpoint between any two apices of a tetrahedron is not an inversion symmetry centre, these samples exhibit non-vanishing DM-interactions. According to the Moriya's rule, each DM-vector on the bond should be perpendicular to the bond and parallel to the surface of the surrounding cubic unit-cell. The spin Hamiltonian in describing this system is given by [12, 230, 231]

$$H_{eff} = -\sum_{ij} J_{ij}\mathbf{S}_i \cdot \mathbf{S}_j + \sum_{ij} \mathbf{D}_{ij} \cdot (\mathbf{S}_i \times \mathbf{S}_j) - \sum_i \mathbf{B} \cdot \mathbf{S}_i \tag{5.1}$$

where, J_{ij} is the isotropic symmetric exchange integrals, $\mathbf{D}_{ij}$ is the DM-vectors, and $\mathbf{B}$ is the externally applied magnetic field. The DM-interaction acts as an effective gauge field that gives rise to a non-vanishing Berry phase effect on the magnons. Here, we note that the DM-vectors do not hamper the ferromagnetic ground state of the material because the sum of all the DM-vectors on the bonds sharing the same site is zero ($\sum_{i(\neq j)} \mathbf{D}_{ij} = 0$) [12, 229].

5.3.2 THEM studies

For the generation of magnon Hall current, a thermal gradient (∇T_{zz}) is applied across the thickness of the device (along the z-direction) with the magnetic field (H) being applied along the y-direction. Thus, the THEM is determined by means of the thermoelectric voltage across the attached NM-layer − which is measured along the x-direction, orthogonal to both the H and the ∇T_{zz}, as depicted in Fig.5.1. The THEM signal is quantified as a function of both H and the average sample temperature (T_{av}). The average sample temperature is determined as $T_{av} = \frac{1}{2}(T_1 + T_2)$, where T_1 and T_2 are the temperatures at opposite surfaces of the crystal, measured by two Cernox sensors. Thus, the applied $\nabla T_{zz} = T_2 - T_1$. During the H-dependent measurement, the measured voltage at $H = 0$ Oe is considered as the background voltage (V_0); and the THEM-signal is then quantified as $V_{THEM}(H) = V_i(H) - V_0$ by keeping both the T_{av} and the ∇T_{zz} fixed, where V_i is the measured voltage with field H. On the other hand, during the T-dependent measurement, the background voltage is subtracted by reversing the direction of the magnetic field. T-dependence of the THEM signal is quantified as $V_{THEM}(T) = \frac{1}{2}(V_i(+H,T) - V_i(-H,T))$, where both the H and the ∇T_{zz} are kept fixed.

Apart from the thermoelectric voltage across the NM-bar, the ∇T_{zx} could generate

an additional voltage due to the spin Nernst effect (SNE) if the attached NM-layer possesses a significant spin Nernst angle (θ_{SN}) [49, 232]. The SNE, akin to the spin Hall effect [48], pertains to the generation of a transverse spin current ($\mathbf{J}_s$) under the influence of an external thermal gradient [49, 232]. Mathematically, it could be expressed as [49]:

$$\mathbf{J}_s = \theta_{SN} \nabla T \times \boldsymbol{H} \tag{5.2}$$

Thus, the applied thermal gradient across a bare NM having significant spin-orbit coupling (e.g., Pt or W) results in the generation of spin-current inside that NM, where the generated spin-current propagates in the opposite direction for having the opposite spin-polarization. However, such spin-current reflects back from the surfaces of the specimen and cancel each other. Whereas, in contact with a ferromagnetic insulator (FMI), the generated spin-current inside the NM layer induces a net spin accumulation at the interface, which exerts a torque on the ferromagnet by means of the spin-transfer torque (STT) [49, 232]. Thus, the incident spin-current is partially absorbed by that ferromagnet by means of STT, creating a non-vanishing spin current in the direction normal to the interface, which is further converted into an electric voltage by the inverse spin Hall effect (ISHE) [49, 232, 233]. In our case, this ISHE-voltage − also termed as spin Nernst voltage − contributes additively to the thermoelectric voltage. Since both the thermoelectric effect and the SNE are caused by the ∇T_{zx}, the total transverse voltage is termed as THEM-Voltage (V_{THEM}). Mathematically, the V_{THEM} could be expressed as [49, 232]

$$V_{THEM} = \left[S + \Delta S_1 + \Delta S_2 (1 - m_y^2) \right] \nabla T_{zx} \tag{5.3}$$

where,

$$\Delta S_1 = S\theta_{SH}\theta_{SN}\frac{2\lambda}{t_N}\tanh\left(\frac{t_N}{2\lambda}\right) \tag{5.4}$$

$$\Delta S_2 = -S\theta_{SH}\theta_{SN}\frac{\lambda}{t_N}Re\frac{2\lambda G\tanh^2\frac{t_N}{2\lambda}}{\sigma_{NM}+2\lambda G\coth\frac{t_N}{\lambda}} \tag{5.5}$$

$$m_y = \mathbf{M}\cdot\hat{y}/|\mathbf{M}| \tag{5.6}$$

Here, S is the Seebeck coefficient of the NM-layer, ΔS_1 and ΔS_2 are the corrections to the Seebeck coefficient due to SNE, θ_{SH} is the spin Hall angle of the NM, θ_{SN} is the spin Nernst angle of the NM, λ is the spin diffusion length inside the NM-layer, t_N is the thickness of the NM-layer, σ_{NM} is the electrical conductivity of the NM, G is the spin-mixing conductance at the interface, and $\mathbf{M}$ is the magnetization of the FMI. Prior experimental demonstration of SNE was demonstrated by applying a constant in-plane thermal gradient, where the spin Nernst voltage was found to vary symmetrically with respect to the magnetization of the FMI, as expected from the third term in Equation 5.3 [49, 232]. In contrast, here, the ∇T_{zx} is generated at the interface by means of the THEM – suggesting that the SNE, along with the thermoelectric effect across the NM-layer, would contribute anti-symmetrically with respect to the magnetization of the specimen in determining the V_{THEM} signal.

5.3.2.1 THEM studies on YVO[100]

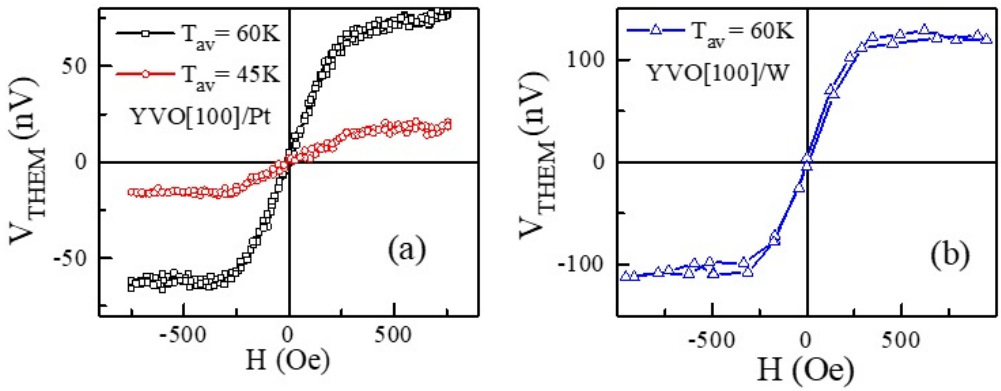

Figure 5.6: H-dependence of the THEM signal, measured from (a) YVO[100]/Pt and (b) YVO[100]/W devices.

Fig.5.6(a) depicts the H-dependence of the THEM signal ($V_{THEM}(H)$), measured from the YVO[100]/Pt device at two different sample temperatures (60 K and 45 K) by keeping the applied ∇T_{zz} = 10 K. Since the measurement-geometry, as well as the measurement-protocols, are similar to that of the longitudinal spin Seebeck measurements [5, 103, 109, 234], there could be an additional role of longitudinal spin Seebeck effect (LSSE). Prior investigations demonstrated that the generation of LSSE-voltage is possible if a net spin current is pumped through the interface into the NM-layer. The spin-pumping is determined by the properties of the interface, such as the spin-mixing conductance of the interface, the roughness of the interface, and the effective temperature difference between the magnons and the conduction electrons at the interface [5, 7, 101, 171, 234, 235]. On the other hand, any contamination due to the ANE is neglected since the prior experiments confirmed the absence of ANE in systems comprised of magnetic-insulator/NM bilayers [103, 109, 110, 234]. In the case of LSSE, the generated voltage is known to change its polarity by changing the spin Hall angle of the detection layer [2, 72, 234]. For this reason, a similar measurement has also been performed by replacing the detection layer of Pt by W, where all other control parameters,

like, the ∇T_{zz} and T_{av}, are kept unchanged. Fig. 5.6(b) depicts that the polarity of the observed signal, as measured from the YVO[100]/W device, is similar to the signal measured from YVO[111]/Pt device (Fig.5.6(b)), even though the sign of the spin Hall angle of Pt is opposite to that of W [72]– confirming the THEM signal.

Fig.5.7 depicts the temperature-dependence of the THEM signal ($V_{THEM}(T)$), measured from the YVO[100]/Pt system by varying the T_{av}, where the ∇T_{zx} and H are kept fixed at 10K and 500 Oe, respectively. The V_{THEM} vs. T plot clearly depicts a characteristic temperature T^* ($\approx$ 35 K), below which the observed signal vanishes. Both the ANE and the LSSE are monotonically increasing functions of the sample temperature. At low temperatures, the ANE varies proportionally with T [88], and the LSSE varies as $T^{0.5}$ [234] or T [117]. This implies that the ANE or the LSSE vanishes only at $T = 0$ and that any contamination of the THEM signals by the ANE or the LSSE could be ruled out in our case.

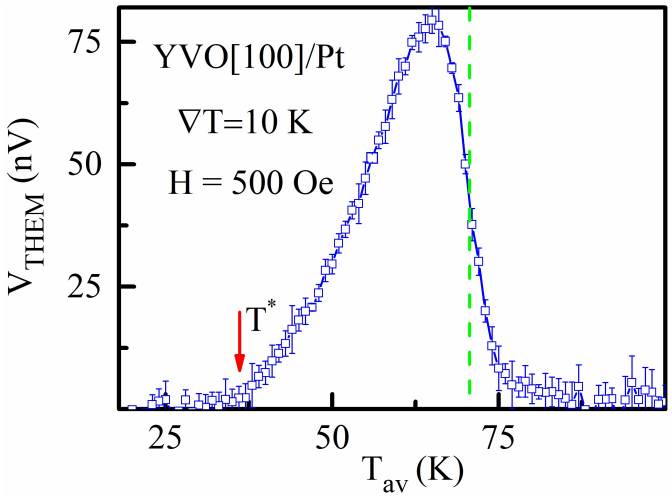

Figure 5.7: T-dependence of the THEM signal measured from YVO[100]/Pt. The dotted line is marked at T_c, and red arrow is marked at T^*.

In the case of Pt, the $\theta_{SH} \approx 0.1$ [72], and $\theta_{SN} \approx -0.12$ to -0.24 [232]. Thus, with $\lambda \approx t_{Pt}$ in our case, the contribution of SNE (via the ΔS_1 and ΔS_2 terms) is

expected to be a couple of orders smaller than the thermoelectric voltage across the Pt bar. Furthermore, the contribution of ΔS_2 vanishes when the magnetization gets saturated in the y-direction (see equation 5.2). So, the $V_{THEM}(T)$ primarily constitutes of the conventional thermoelectric effect in the Pt layer. Thus, the functional form of the $V_{THEM}(T)$ is determined by the T-dependence of both the $\nabla T_{zx}(T)$ and the Seebeck coefficient of the Pt layer ($S_{Pt}(T)$). Prior reports also showed that the S_{Pt} displays a smooth and non-vanishing functional form in the whole temperature regime of our experiments [236]. The fact that the $V_{THEM}(T)$ vanishes at a temperature below T^* suggests that temperature dependence of the $\nabla T_{zx}(T)$ must be at play in determining the THEM-signal.

Prior experimental findings of the THEM have been quantified in terms of K_{zx}, determined via the relation $K_{zx} \approx \frac{K_{zz}^2 \nabla T_{zx}}{j_q}$ where K_{zz} is the longitudinal thermal conductivity, and j_q is the thermal current density [15]. Initially, the analytical expression of the K_{zx} was derived by using the Kubo formula, where the K_{zx} was shown to arise as a consequence of non-vanishing Berry curvature of the magnon band in momentum space (k-space) [12, 15, 111]. It is also shown that the effective DM-interaction makes the Berry curvature non-zero [12, 15, 111]. However, later in 2011, Matsumoto and Murakami pointed out an additional correction due to the rotational motion of magnons [13, 14]. The expression of K_{zx} for the three dimensional pyrochlore ferromagnet could be expressed as [13–15, 237]

$$K_{zx} = 2T \sum_n \int_{BZ} \frac{d^3k}{(2\pi)^3} c_2(\rho_n(\mathbf{k}))\Omega_{n,z}(\mathbf{k}) \tag{5.7}$$

with $c_2(\rho) = (1+\rho)\left(\log\frac{1+\rho}{\rho}\right)^2 - (\log\rho) - 2Li(-\rho)$, and the local Berry curvature of the n^{th} magnon band $\Omega_{n,z}(\mathbf{k}) = Im\left\langle \frac{\partial\psi_n(k)}{\partial k_x} \middle| \frac{\partial\psi_n(k)}{\partial k_y} \right\rangle$. Here, n is the index that describes the

discrete energy level of the magnon bands, ρ is the Bose-Einstein distribution function of magnons, and $\psi_n(\mathbf{k})$ is the wave function of magnons at the n^{th} energy band having momentum $\mathbf{k}$. Equation 5.7 suggests that the THEM-signal is determined by the additive contribution of all magnon bands, where the c_2-function acts like a weightage to each band, determined by the population of magnons at that band. At low temperatures, the lower energy states become more populated and so the primary contribution comes from the lower bands due to the c_2 function. As the temperature is increased, bands of higher energy levels become occupied and provide significant contributions to the Hall transport. Prior theoretical work, based on stacking of Kagomé layers, also showed the energy (ε) dependency of the c_2 function, depicted in Fig.5.8 – suggesting that at low temperatures the contribution of the magnons with higher energy are significantly suppressed by this c_2 function [231]. The fact that the observed signal (depicted in the Fig.5.7) vanishes at temperatures below T^*, whereas it rises steeply with the temperatures above T^*, suggests that the magnons from the higher energy-bands contribute significantly to the THEM signal.

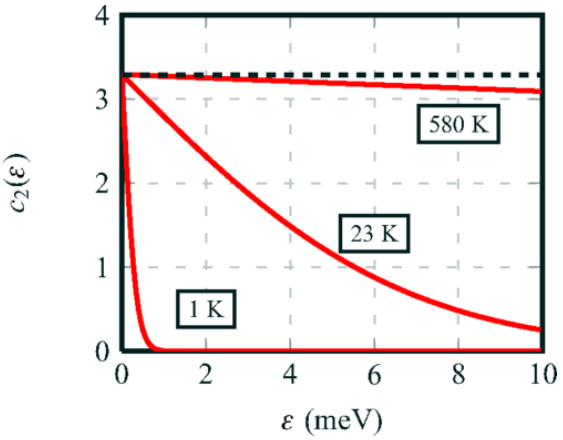

Figure 5.8: depicts the $c_2(\varepsilon)$ vs. ε plots at three different sample temperatures, where $c_2(\varepsilon)$ is the population weightage of magnons at a energy band and ε is the energy of momgons [231]. Adapted with permission from Ref.[231], copyright (2014) by the American Physical Society.

Previous experimental findings of the THEM in the closely related $Lu_2V_2O_7$ system was analysed by fitting the H-dependent K_{zx} data, where the analytical expression of k_{zx} was derived by assuming that only the lowest magnon band contributes to the THEM [12, 15]. As a result, it ended up with an overwhelming value of the $\frac{D}{J}$ ratio ($\approx$ 38% [15] or 35% [12]) in comparison to that of the previously reported $Y_2V_2O_7$ specimen (a first principle calculation suggested that $\frac{D}{J}$ ratio of the $Y_2V_2O_7$ is only 5% [229]). However, the magnetic properties of $Y_2V_2O_7$ are similar to that of the $Lu_2V_2O_7$ [227–229]. This mismatch was also pointed out in another theoretical work by A. Mook et al., where they described that the assumption of the solitary contribution of the lowest energy-band causes an overestimation of the DM interaction [231]. Finally, the functional form of K_{zx}, derived from lowest-band approximation, shows a monotonically increasing function of the sample temperature [15], which could not explain the observation of the characteristic temperature (T^*). In contrast, our observation clearly indicates the contributions of the higher energy-bands of magnons. Interestingly, in a recent theoretical work by Christian Moulsdale and co-workers, the effective K_{zx} was also calculated by the individual contribution of all the bulk bands, where both the polarity and the magnitude of the individual contributions of each magnon-band were determined by the associated local Berry curvature and occupation probability of magnons at that band [237].

5.3.2.2 THEM studies on YVO[111]

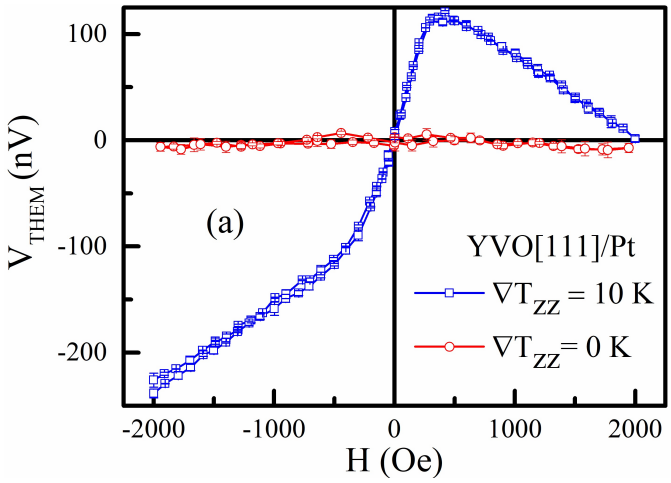

Figure 5.9: Magnetic field dependence of the THEM-signal, measured from YVO[111]/Pt device, with the T_{av} = 50 K.

Fig.5.9 depicts the H-dependent THEM-signals, measured from the YVO[111]/Pt device, with two different applied thermal gradients (∇T_{zz} = 10K and 0 K). Here, the average sample temperature (T_{av}) is maintained at 50 K during each of these measurements. In contrast to that of YVO[100]/Pt, the YVO[111]/Pt device depicts that the V_{THEM} does not saturate with the magnetization. The THEM-signal is found to be contaminated by an additional signal that varies symmetrically with respect to applied H. To distinguish this additional signal, we decompose the measured signal into the anti-symmetric and symmetric components: $V_{THEM} = V^{A,Pt}_{THEM} + V^{S,Pt}_{THEM}$; where $V^{A,Pt}_{THEM} = \frac{1}{2}(V_{THEM}(+H) - V_{THEM}(-H))$ and $V^{S,Pt}_{THEM} = \frac{1}{2}(V_{THEM}(+H) + V_{THEM}(-H))$. Here, $V^{i,NM}_{THEM}$ notation is used to describe both the anti-symmetric and the symmetric components of the measured THEM-signal, where $i \equiv A$ or S stands for the anti-symmetric or symmetric, respectively. NM is the metal layer that is used to quantify the THEM-signal in the YVO[111] crystal.

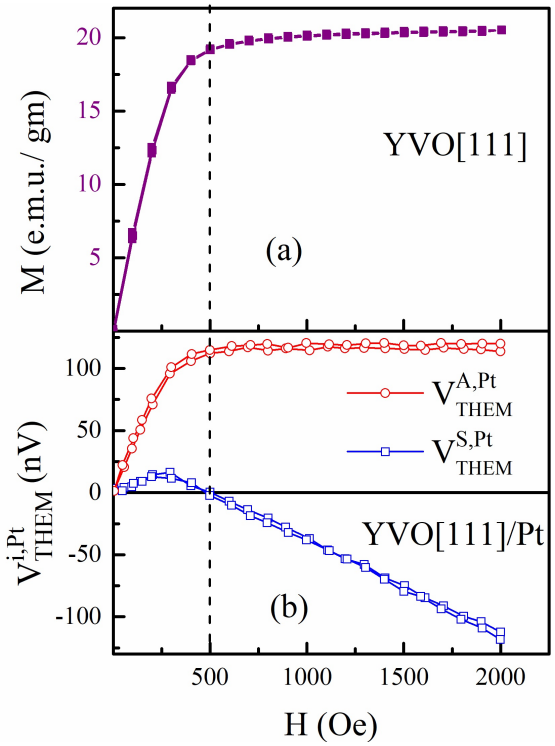

Figure 5.10: Magnetic field dependence of (a) the magnetization, and (b) symmetric and antisymmetric components of the THEM-signal which is measured from YVO[111]/Pt device. The dotted line is marked at the saturating magnetization.

Figure 5.10(b) illustrates the $V^{A,Pt}_{THEM}$ and the $V^{S,Pt}_{THEM}$ components of the total-signal, depicted in Fig.5.9 with the ∇T_{zz} of 10 K. To demonstrate how these components vary with the magnetization, we also show the M-H plot in Fig.5.10(a), shown only in the positive sector of the applied magnetic field. The $V^{A,Pt}_{THEM}$ is found to be saturated with the magnetization of the specimen, as expected in the case of THEM-signal. $V^{S,Pt}_{THEM}$ also shows a profound dependence on the applied magnetic field. At low fields, it starts to increase with $|H|$. However, after a certain increment of that field, it decreases with further increasing $|H|$, and then it changes its sign from positive to negative near the saturation of the magnetization. In particular, after achieving the saturated magnetization of the specimen, $V^{S,Pt}_{THEM}$ varies linearly with $|H|$. We infer that the initial rise

of the $V_{THEM}^{S,Pt}$ in the low magnetic field could be a consequence of various magnetoresistive (MR) effects, such as anisotropic magnetoresistance (AMR) [238], spin-orbit magnetoresistance (SOMR) [239], and spin Hall magnetoresistance (SMR) [240, 241]. However, each of these MR gets saturated with the magnetization of the specimen – implying that such MR-effects do not have any role in determining the variation of $V_{THEM}^{S,Pt}$ beyond the saturation magnetization. However, prior experimental demonstration of Hanle magnetoresistance (HMR) showed that the HMR varies with the external magnetic field, instead of the magnetization of the specimen [242]. However, the fact that the $V_{THEM}^{S,Pt}$ varies linearly with the applied magnetic field, whereas the HMR shows a parabolic functional form with respect to the external magnetic field [242], suggests that HMR is unlikely to play a role in this case. For further cross-checking, another similar measurement is performed by replacing the Pt-layer with W. Fig.5.11 (a) depicts the magnetic field dependence of the transverse signal, measured from YVO[111]/W device – and, both the symmetric ($V_{THEM}^{S,W}$) and the antisymmetric ($V_{THEM}^{A,W}$) components of that observed signal are illustrated in Fig.5.11 (b). The blue dashed line in Fig.5.11 (b) is marked at the field at which the magnetization becomes saturated. Clearly, the polarity of the $V_{THEM}^{A,W}$ is found to be similar to that of the $V_{THEM}^{A,Pt}$ – as expected for the THEM-signal. On the other hand, the $V_{THEM}^{S,W}$ is also found to exhibit profound dependence on the external magnetic field. However, unlike the $V_{THEM}^{S,Pt}$, the $V_{THEM}^{S,W}$ increases monotonically with the applied field without having any sign change. A expanded view of both the $V_{THEM}^{S,Pt}$ and the $V_{THEM}^{S,W}$ are depicted in Fig.5.13 (a) and 5.13(b), respectively, shown in the saturated magnetization regime. The $V_{THEM}^{S,Pt/W}$ is observed to vary linearly with H with a slope that alters its sign when the NM layer is changed from Pt to W. However, the resistive modulation due to HMR is known to be proportional to the square of the spin Hall angle of the NM-layer ($\Delta\rho_{HMR} \propto \theta_{SH}^2$) [242] – suggesting that

the role of HMR could be ruled out in our case.

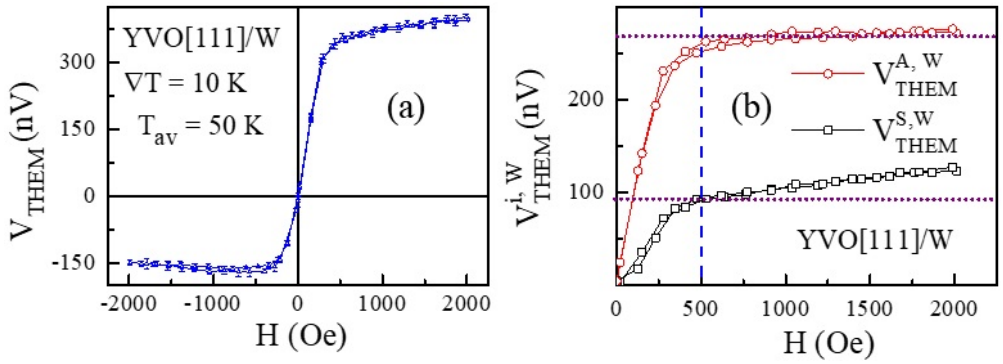

Figure 5.11: Magnetic field dependence of (a) the THEM-signal measured from the YVO[111]/W device, and (b) symmetric and anti-symmetric components of that THEM-signal. The dashed vertical-line is marked at the saturating magnetization of the specimen. The dotted horizontal-line is placed to guide how both the symmetric and anti-symmetric components vary above thee saturated magnetization.

In order to explain such a linearly varying $V_{THEM}^{S,Pt/W}$ signal, in addition to the thermodynamic contribution, we invoke the magnon drag effect (MDE) that ultimately stems from spin-orbit interactions [243–247]. The microscopic mechanism of the MDE is described by two different theoretical approaches. The first one is the hydrodynamic approach, introduced by G. N. Grannemann and L. Berger in 1976, where both the magnons and the electrons are treated as two interpenetrating fluids [243]. The magnon drag thermopower in this approach is given by [243]:

$$S_{md} = \frac{\alpha_m}{n_e e} \frac{k_B^{\frac{5}{2}} T^{\frac{3}{2}}}{6\pi^2 D^{\frac{3}{2}}} L(y) \tag{5.8}$$

where, α_m is a dimensionless parameter that arises from the electron current dragged due to the magnon flow, n_e is the density of conduction electrons, e is the charge of an electron, k_B is the Boltzmann constant, D is the spin-stiffness, and $L(y)$ is called

'quenching function'. Here, $y = \frac{g\mu_B B_{eff}}{k_B T}$ with g, μ_B, and B_{eff} being the Landé g-factor, the Bohr magneton, and effective magnetic field, respectively. With the help of numerical integration, it is shown that the $L(y)$ varies linearly with $|B_{eff}|$ in low magnetic field limit (typically, bellow $3T$ when temperature of the specimen $T \leq 50$K). Recently, M.V. Costachethe and co-workers experimentally demonstrated the MDE in the context of magnon drag thermopile, where the magnetic field dependence of the magnon drag thermopower was showed to obey such linear functional form owing to that quenching function [246]. Here, the B_{eff} is determined by the external magnetic field ($|H|$) in addition to the magnetization (M). Thus, in the low field limit, $L(y)$ is expected to vary linearly with $|H|$ in the saturated magnetization regime. Fig.5.12 clearly depicts such linear functional form of the $V_{THEM}^{S,Pt/W}$ signal – suggesting the possible role of the MDE in determining the symmetric component.

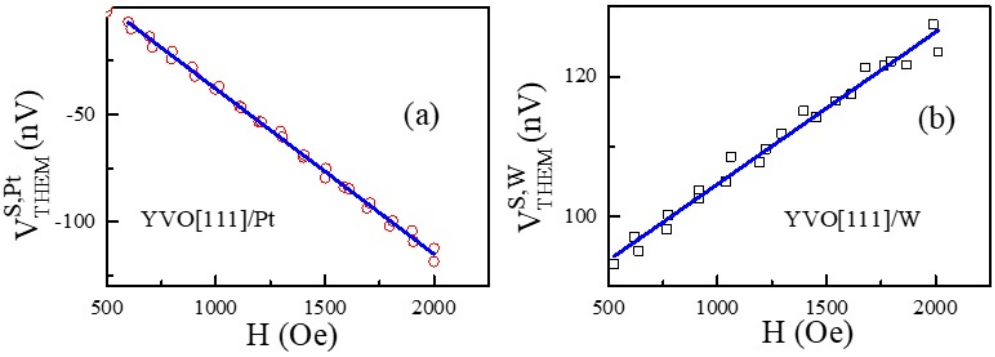

Figure 5.12: Magnetic field dependence of the (a) $V_{THEM}^{S,Pt}$, and (b) $V_{THEM}^{S,W}$, measured by utilising YVO[111]/Pt or W device

In an alternative theoretical approach, the MDE is described in terms of the spin-motive force ($\langle F_i \rangle$), in which magnons exert a dragging force on the conduction electrons that depends on the spin-polarization of those electrons [244, 245, 247, 248]. In our case, an in-plane magnon flow at the interface could possibly drag the conduction electrons that can give rise to such a $V_{THEM}^{S,Pt/W}$-signal. The electric current due to magnon

drag could be written as [244, 245, 247, 248]:

$$\mathbf{j}_{drag} = \frac{\sigma_{\uparrow} - \sigma_{\downarrow}}{e^2} \langle \mathbf{F}_i \rangle = -\left(1 - \frac{\beta}{3\alpha}\right) \frac{\hbar^2 \sigma \gamma P_s}{2eS_0 D} k_m \nabla T_{zx} \tag{5.9}$$

Here, α is the Gilbert damping constant, β is a dimensionless parameter that arises from the electric current pumped by the dynamic magnetization associated with a magnon heat flux, γ is the gyromagnetic ratio of the conduction electrons, σ is the conductivity of NM-layer with $\sigma_{\uparrow}$ and $\sigma_{\downarrow}$ being the conductivities with up and down spin-polarizations, e is the charge of an electron, S_0 is the magnon density, D is the spin stiffness at the interface, $P_s = \frac{\sigma_{\uparrow} - \sigma_{\downarrow}}{\sigma}$ is the spin-polarization of conduction electrons at the interface, and k_m is the thermal conductivity of magnons at the interface. The symmetric nature of $\mathbf{j}_{drag}$ is expected since both the P_s and ∇T_{zx} reverse their sign with the applied field direction ($\mathbf{n} = \frac{\mathbf{H}}{|H|}$). Equation 5.9 shows the crucial role of P_s in determining the dragged electric current. Since the SNE creates a net spin-accumulation at the interface [49, 232], it could significantly change the effective P_s at that interface – implying a commensurate change in the magnon drag voltage that depends on the spin Nernst angle (θ_{SN}) of the NM-layer. With the polarity of θ_{SN} of Pt being opposite to that of W [232], the slope of $V_{THEM}^{S,Pt/W}$ in the saturated magnetization regime is observed to change its sign by changing the NM-layer of Pt by W, thus confirming the MDE in this YVO[111]/Pt or W systems (see Fig.5.12 (a) and 5.12(b)). It is worth mentioning that the linearly varying $V_{THEM}^{S,Pt/W}$ signal with respect to H in the saturated magnetization regime is also understood in terms of spin-accumulation at the interface, which also increases linearly with the applied field via Equation 5.2. Here we also note that the SNE of W is reported to be suppressed when the t_W is larger than 6Å[233], which also explains why the rate of increment of the $V_{THEM}^{S,W}$ is much lower than that of $V_{THEM}^{S,Pt}$.

Since the magnon flow at the interface is caused by the MHE, the associated dragging effect is also expected to vanish at $\nabla T_{zz} = 0$. It explains why the total signal, depicted in Fig.5.9, vanishes at $\nabla T_{zz} = 0$.

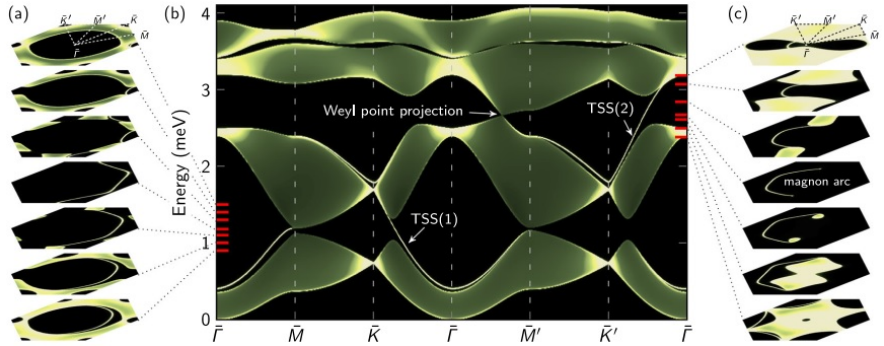

Figure 5.13: Magnons at the (111) surface of a ferromagnetic pyrochlores of the form $A_2V_2O_7$, with 'A' being the rare-earth element. (a) and (c) show constant-energy cuts near the band gap and Weyl points, respectively [230]. (b) Spectral density along high-symmetry directions of the surface Brillouin zone. The broad features are the contribution of bulk bands, whereas the sharp lines represent the surface states of magnon [230]. Adapted with permission from Ref.[230], copyright (2016) by the American Physical Society.

In order to understand why the YVO[111]/Pt system displays the MDE, whereas the YVO[100]/Pt system does not show such an effect, we look into the fact that how the magnon's band-structure is modified by changing the direction of the applied magnetic field (**n**). Recently, A. Mook and co-workers theoretically predicted the magnon band structure of a ferromagnetic pyrochlore system, described by four bulk-bands, termed as B_1, B_2, B_3, and B_4. All of these bulk-bands possess non-vanishing Berry curvature, which is a crucial ingredient for the THEM [230]. It was also shown that there is a band-gap between the B_1 (lowest bulk-band) and the B_2 (second bulk-band) as long as the **n** is not within the {100} plane [230]. Fig.5.13 depicts the reported band structure with the magnetic field being applied along the [111] direction [230]. With the Chern number of the B_1 being reported to be -1 [230], the winding number of this gap would

be −1, suggesting that there exists a topological surface state (termed as TSS1) as long as the gap-opened condition is satisfied. Thus, in our case, by changing the direction of **H** from the [100] to the [111], we incorporate topologically protected chiral surface magnons (CSM). Since the TSS1 appears at an energy-level where no other bulk state exists [230], we speculate that this CSM would be more efficient in transferring its momentum to the neighbouring conduction electrons at the interface, resulting a significant MDE. In contrast, the YVO[100]/Pt device does not show the MDE-signal because the aforementioned band-gap remains closed – where, instead of the TSS1, only trivial surface state of magnon (TSSM) would exist. Since the TSSM appears at an energy level at which other bulk-magnons also do coexist, the trivial surface magnons could dissipate its momentum to the bulk-magnons causing a suppression of this effect. On the other hand, it is also reported that the B_2-band and the third bulk-band (B_3) linearly cross each-other at two different points in the Brillouin zone. This gives rise to a couple of Weyl points with opposite topological charges, where another topological surface state (termed as TSS2) appears that connects these Weyl points [230]. Thus, an unidirectional magnon-flow through the TSS2 is also expected from the positively charged Weyl point to the negatively charged Weyl point. However, with the Weyl points being reported to appear along the line parallel to the applied **H** [230], the contribution of such a magnon flow through the TSS2 would be orthogonal to the voltage picking axis. Thus, we ignore the contribution of TSS2 in determining the observed MDE. It is also realized from the fact that the measured signal from the YVO[100]/Pt device is observed to be anti-symmetric with respect to **H**, even though such TSS2 also exists in this case (**H** || [100]) [230]. Nonetheless, the Berry curvature of the bulk-bands would be significantly large near the Weyl points, which can have a significant role in determining the THEM-signal. Recently, V. A. Zyuzin et al. theoretically disentangled the

role of Weyl magnon from the anomalous Hall magnon [249]. We also note that, in the case of a pyrochlore ferromagnet, such Weyl points are created at the higher energies of the system (≈ 2.67 meV [230]), which is in good agreement to the characteristic temperature T^* (since K_BT^* is close to 2.67 meV, with K_B being the Boltzmann constant). Thus, the fact that the THEM signal vanishes bellow T^* (depicted in Fig.5.7 and Fig.5.14), although the lowest magnon band possesses non-vanishing Berry curvature [230], reinforce the need to look into the possible role of Weyl magnons in determining the THEM signal.

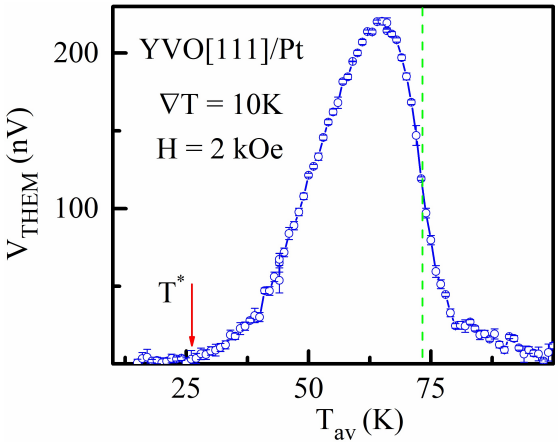

Figure 5.14: T-dependence of the THEM signal measured from YVO[111]/Pt. The dotted line is marked at T_c, and red arrow is marked at T^*.

The temperature dependence of the THEM signal, measured from the YVO[111]/Pt system, is depicted in Fig.5.14. During this measurement, both the applied field and thermal gradient are kept fixed at 2 kOe and 10 K, respectively. It is also worth mentioning that, by virtue of measurement protocols, this signal stems from the anti-symmetric component of the measured signal. Fig.5.14 clearly shows the characteristic temperature, $T^* \approx 27$ K – again suggesting that a significant contribution to the THEM-signal arises from the higher energy-bands of magnons in this pyrochlore ferromagnet system.

5.4 Conclusion

In conclusion, we have studied the THEM signals from the single crystal of $Y_2V_2O_7$ pyrochlore ferromagnet, where the generated transverse thermal gradient is measured by putting a NM-layer on top of the crystal plane. Our observations reinforce the need to individually ascertain the contribution of all magnon-bands in quantifying the THEM-signal. Our investigation also hints the possible role of Weyl-magnons in determining the THEM-signal. Finally, the magnetic field dependent measurements reveal that, in contrast to YVO[100]/Pt system, the YVO[111]/Pt device also displays a significant MDE at the interface. By looking into the theoretically predicted band structure of a ferromagnetic pyrochlore, we link the observed MDE-signal to the topologically protected surface states of magnons.

Chapter 6

Summary and Outlook

In summary, the main focus of this thesis lies in the investigation of various spin caloritronic phenomena, in which an externally applied thermal gradient acts as a driving force for the generation of the spin-caloritronic signals. The work was begun with instrumentation, followed by the studies of the longitudinal spin Seebeck effect (LSSE), anomalous Nernst effect (ANE), and thermal Hall effect of magnons (THEM) in the various material system with different forms like thin-films, polycrystalline bulk-sample, and single-crystalline specimen. The summary of the key work, along with its future perspectives, are pointed below.

- The measurement-unit for sensitive measurements of spin-caloritronic signals has been designed and developed. The set-up comprises of a closed cycle refrigerator (CCR), a temperature controller, a nano-voltmeter, a source meter, and an electromagnet with an upper field limit of 2 kOe. Two PID controlled heaters control the temperature gradient across the sample, as well as the average temperature of the sample. The temperature is measured by two temperature sensors attached near the sample edge. The sample holder is so designed that the applied thermal gradient is always orthogonal to the magnetic field's rotation plane. The whole set-up was put inside a Faraday cage to reduce the noise. Presently, signals as low as 10

nV can be reliably measured in this set-up. The primary limitation of this set-up is that the upper limit of the applied magnetic field is 2 kOe. Thus, the possible future direction to upgrade the set-up is to increase that upper limit of the applied magnetic field, so that many other material systems, including anti-ferromagnets and hard-magnets, could be investigated in search of potential candidates for the generation of spin-caloritronic signals.

- The LSSE in an optimally doped $La_{0.7}Ca_{0.3}MnO_3$ system has been investigated. After disentangling the contribution due to ANE, we observed that in the low-temperature regime, the longitudinal spin Seebeck voltage ($V_{LSSE}(T)$) varies as $T^{0.5}$ – an observation which is in good agreement with the magnon-driven spin current model. In the para-to-ferromagnetic transition region, the LSSE exponent was found to be much larger than that of the magnetization. Interestingly, this exponent was also found to vary with the thickness of the spin-to-charge conversion layer (Pt-layer in our case), indicating that the temperature dependence of spin mixing conductance played an important role in the measured $V_{LSSE}(T)$. Our investigation emphasizes the need to individually ascertain the temperature dependencies of the contributory mechanisms – especially the spin mixing conductance – which play a role in determining both the magnitude of spin current as well as the extent of spin to charge conversion to understand the temperature-dependent LSSE in strongly correlated materials. As a future direction, the quantification of spin-mixing conductance is suggested. A set-up of ferromagnetic resonance (FMR) measurements could be utilized to quantify this particular quantity. So, the FMR measurement is proposed for future developments in this area of the Spin-Caloritonics.

- The ANE has been investigated for the first time in the Ni-Mn-Ga class of materials, and it clearly showed the substantial sensitivity across the premartensitic phase in comparison to other conventional transport measurements, like, the resistivity, the thermal conductivity, and the Seebeck coefficient. In particular, we have quantified the temperature dependence of the ANE ($V_{ANE}(T)$) in a polycrystalline specimen of Ni_2MnGa. By eliminating the possible role of the Berry phase effect due to the polycrystalline form of our sample, the functional form of $V_{ANE}(T)$ across the premartensitic phase highlights the coupling between magnetism and the Fermi surface, where the ANE is tuned by the magnetic field-driven changes at the Fermi surface. It is worth mentioning that, besides the structural modulations, the occurrence of charge density wave (CDW) at the onset of premartensitic transition was also reported in this Ni_2MnGa system. Since the magnetic field induced strain (MFIS) originates from this structural modulations, such sensitivity of the ANE describes the link between the structural modulations and the modulation of the Fermi surface via its nesting features, where the MFIS acts like a mediating mechanism for the magnetic field-driven changes at the Fermi surface. With ANE being sensitive to the changes in the Fermi surface, our work suggests that it could be utilized as a sensitive tool to probe the physics of CDW in many other material systems, which is associated with the Fermi surface nesting features.

- The thermal Hall effect of magnons (THEM) has been investigated in single crystals of the $Y_2V_2O_7$ system. In particular, we quantify the THEM along two different orientations of the crystal, {100}, and {111}, by putting a thin non-magnetic metal-layer (NM) on top of the [100] or [111] plane of that crystal. Our observation reinforces the need to individually ascertain the contributions of all the

magnon-bands in quantifying the Hall response of magnons. A possible role of the Weyl magnon was also discussed in determining the observed thermal Hall signals. Additionally, the measurements from the crystals oriented along the {111} plane were found to display a significant magnon drag effect (MDE) at the interface. By considering the theoretically predicted magnon band structure of these pyrochlore ferromagnets, we link the MDE with the chiral surface state of magnons. As of future planning, a detailed characterization of such effects is proposed, where the temperature and magnetic fields dependencies of this effect, the role of topologically protected chiral surface magnons in such Hall transport, and its potential utility in device applications could be investigated.

Bibliography

[1] K Uchida et al., Nature **455**, 778 (2008).

[2] K.-i. Uchida et al., Nat. mater. **9**, 894–897 (2010).

[3] C. Jaworski et al., Nat. mater. **9**, 898 (2010).

[4] K.-i. Uchida et al., Phys. Rev. X **4**, 041023 (2014).

[5] K.-i. Uchida et al., Applied Physics Letters **97**, 172505 (2010).

[6] D. Meier et al., Nat. commun. **6**, 8211 (2015).

[7] J. Xiao et al., Phys. Rev. B **81**, 214418 (2010).

[8] S. M. Rezende et al., Phys. Rev. B **89**, 014416 (2014).

[9] Y. Pu et al., Phys. Rev. Lett. **101**, 117208 (2008).

[10] T. C. Chuang et al., Phys. Rev. B **96**, 174406 (2017).

[11] A. Ghosh et al., Appl. Phys. Lett. **113**, 262405 (2018).

[12] Y Onose et al., Science **329**, 297–299 (2010).

[13] R. Matsumoto and S. Murakami, Phys. Rev. Lett. **106**, 197202 (2011).

[14] R. Matsumoto and S. Murakami, Phys. Rev. B **84**, 184406 (2011).

[15] T. Ideue et al., Phys. Rev. B **85**, 134411 (2012).

[16] V. Uskokovic, Curr. Nanosci. **5**, 372–389 (2009).

[17] E. Pop, Nano Res. **3**, 147–169 (2010).

[18] A. Agarwal et al., IEEE Micro **26**, 68–80 (2006).

[19] S. Bhunia and K. Roy, in 2007 ieee international test conference (IEEE, 2007), pp. 1–10.

[20] A. Hoffmann and S. D. Bader, Phys. Rev. Applied **4**, 047001 (2015).

[21] N. F. Mott, Proceedings of the Royal Society of London. Series A-Mathematical and Physical Sciences **153**, 699–717 (1936).

[22] M. N. Baibich et al., Phys. Rev. Lett. **61**, 2472–2475 (1988).

[23] G. Binasch et al., Phys. Rev. B **39**, 4828–4830 (1989).

[24] M. Julliere, Phys. Lett. A **54**, 225–226 (1975).

[25] T. Miyazaki and N Tezuka, J. Magn. Magn. Mater. **139**, L231–L234 (1995).

[26] J. S. Moodera et al., Phys. Rev. Lett. **74**, 3273–3276 (1995).

[27] T. Endoh and H. Honjo, Journal of Low Power Electronics and Applications **8**, 44 (2018).

[28] S. Wolf et al., science **294**, 1488–1495 (2001).

[29] J. Lu et al., Int. Mater. Rev. **61**, 456–472 (2016).

[30] I. Žutić et al., Rev. Mod. Phys. **76**, 323 (2004).

[31] S. Maekawa and T. Shinjo, *Spin dependent transport in magnetic nanostructures* (CRC press, 2002).

[32] A. Schuhl and D. Lacour, Comptes Rendus Physique **6**, 945–955 (2005).

[33] S. Bader and S. Parkin, Annu. Rev. Condens. Matter Phys. **1**, 71–88 (2010).

[34] S. R. Boona et al., Energy Environ. Sci. **7**, 885–910 (2014).

[35] G. E. Bauer et al., Nat. Mater. **11**, 391 (2012).

[36] H. Yu et al., Phys. Lett. A **381**, 825–837 (2017).

[37] W. Thomson, Earth and Environmental Science Transactions of The Royal Society of Edinburgh **21**, 123–171 (1857).

[38] S. R. De Groot, J. Math. Phys **4**, 147–153 (1963).

[39] L. Onsager, Phys. Rev. **37**, 405–426 (1931).

[40] L. Onsager, Phys. Rev. **38**, 2265–2279 (1931).

[41] E. H. Hall, Amer. J. Math. **2**, 287–292 (1879).

[42] E Saitoh et al., Appl. Phys. Lett **88**, 182509 (2006).

[43] B. F. Miao et al., Phys. Rev. Lett. **111**, 066602 (2013).

[44] D. Qu et al., Phys. Rev. B **97**, 024402 (2018).

[45] S. Twaha et al., Renew. Sustain. Energy Rev **65**, 698–726 (2016).

[46] K. Behnia, *Fundamentals of thermoelectricity* (OUP Oxford, 2015).

[47] J. Sólyom, *Fundamentals of the physics of solids: volume ii: electronic properties*, Vol. 2 (Springer Science & Business Media, 2008).

[48] J. Sinova et al., Rev. Mod. Phys. **87**, 1213–1260 (2015).

[49] S. Meyer et al., Nature materials **16**, 977 (2017).

[50] S.-g. Cheng et al., Phys. Rev. B **78**, 045302 (2008).

[51] H. Hubert, *Peltier-effect heat pump*, US Patent 3,635,037, 1972.

[52] T. Harman et al., J. Appl. Phys **30**, 1351–1359 (1959).

[53] J. Flipse et al., Phys. Rev. Lett. **113**, 027601 (2014).

[54] S. Daimon et al., Nat. Commun **7**, 13754 (2016).

[55] C. Strohm et al., Phys. Rev. Lett. **95**, 155901 (2005).

[56] L. Zhang et al., Phys. Rev. Lett. **105**, 225901 (2010).

[57] L. Sheng et al., Phys. Rev. Lett. **96**, 155901 (2006).

[58] M. Mori et al., Phys. Rev. Lett. **113**, 265901 (2014).

[59] P. Sharma, Science **307**, 531–533 (2005).

[60] A. Hirohata, *Book review: spin current*, Vol. 6 (Frontiers, 2018), p. 23.

[61] K. ichi Uchida et al., *Chapter one - spin-wave spin current in magnetic insulators*, Vol. 64, Solid State Physics (Academic Press, 2013), pp. 1 –27.

[62] H. Adachi et al., Reports on Progress in Physics **76**, 036501 (2013).

[63] J. E. Hirsch, Phys. Rev. Lett. **83**, 1834–1837 (1999).

[64] J. Sinova et al., Phys. Rev. Lett. **92**, 126603 (2004).

[65] E. Sagasta et al., Phys. Rev. B **94**, 060412 (2016).

[66] M. Dyakonov and V. Perel, Physics Letters A **35**, 459 –460 (1971).

[67] Y. K. Kato et al., science **306**, 1910–1913 (2004).

[68] S. O. Valenzuela and M Tinkham, Nature **442**, 176 (2006).

[69] T. Yang et al., Nat. Phys. **4**, 851 (2008).

[70] Y. Fukuma et al., Nat. Mater. **10**, 527 (2011).

[71] S. Geprägs et al., Nat. commun. **7**, 10452 (2016).

[72] H. L. Wang et al., Phys. Rev. Lett. **112**, 197201 (2014).

[73] C. Herschbach et al., Phys. Rev. B **88**, 205102 (2013).

[74] A. Fert and A. Friederich, Phys. Rev. B **13**, 397–411 (1976).

[75] A. Ferreira et al., Phys. Rev. Lett. **112**, 066601 (2014).

[76] M. Morota et al., Phys. Rev. B **83**, 174405 (2011).

[77] S. Lowitzer et al., Phys. Rev. Lett. **106**, 056601 (2011).

[78] D. Xiao et al., Rev. Mod. Phys. **82**, 1959–2007 (2010).

[79] A. BÃl'rard and H. Mohrbach, Physics Letters A **352**, 190 –195 (2006).

[80] H. Kurebayashi et al., Nature Nanotechnology **9**, 211–217 (2014).

[81] D. Xiao et al., Phys. Rev. Lett. **97**, 026603 (2006).

[82] F. D. M. Haldane, Phys. Rev. Lett. **93**, 206602 (2004).

[83] G. Y. Guo et al., Phys. Rev. Lett. **100**, 096401 (2008).

[84] T. Tanaka et al., Phys. Rev. B **77**, 165117 (2008).

[85] S. Nair et al., Advances in Physics **61**, 583–664 (2012).

[86] E. H. Hall, American Journal of Mathematics **2**, 287–292 (1879).

[87] N. Nagaosa et al., Rev. Mod. Phys. **82**, 1539–1592 (2010).

[88] T. Miyasato et al., Phys. Rev. Lett. **99**, 086602 (2007).

[89] A. Hackl and M. Vojta, Phys. Rev. B **80**, 220514 (2009).

[90] H. X. Tang et al., Phys. Rev. Lett. **90**, 107201 (2003).

[91] Y. Bason et al., Applied Physics Letters **84**, 2593–2595 (2004).

[92] Y. Pu et al., Phys. Rev. Lett. **97**, 036601 (2006).

[93] H. Sharma et al., Materials Chemistry and Physics **180**, 390 –395 (2016).

[94] A. D. Avery et al., Phys. Rev. Lett. **109**, 196602 (2012).

[95] C. T. Bui and F. Rivadulla, Phys. Rev. B **90**, 100403 (2014).

[96] C. Hahn et al., Phys. Rev. Lett. **111**, 217204 (2013).

[97] M. Weiler et al., Phys. Rev. Lett. **111**, 176601 (2013).

[98] S. Watanabe et al., Nat. Phys. **10**, 308 (2014).

[99] M. Toka ç et al., Phys. Rev. Lett. **115**, 056601 (2015).

[100] B. Heinrich et al., Phys. Rev. Lett. **107**, 066604 (2011).

[101] L. Zhu et al., Phys. Rev. Lett. **123**, 057203 (2019).

[102] M. Arana et al., Phys. Rev. B **98**, 144431 (2018).

[103] P. Bougiatioti et al., Phys. Rev. Lett. **119**, 227205 (2017).

[104] D. Tian et al., Applied Physics Letters **106**, 212407 (2015).

[105] S. M. Wu et al., Applied Physics Letters **105**, 092409 (2014).

[106] Y. Xu et al., Applied Physics Letters **105**, 242404 (2014).

[107] A. Kehlberger et al., Phys. Rev. Lett. **115**, 096602 (2015).

[108] C. Du et al., Phys. Rev. Applied **1**, 044004 (2014).

[109] T. Kikkawa et al., Phys. Rev. Lett. **110**, 067207 (2013).

[110] B. F. Miao et al., AIP Advances **6**, 015018 (2016).

[111] H. Katsura et al., Phys. Rev. Lett. **104**, 066403 (2010).

[112] R. Chisnell et al., Phys. Rev. Lett. **115**, 147201 (2015).

[113] G. K. White and P. J. Meeson, *Experimental techniques in low-temperature physics*, Vol. 5 (Clarendon Press Oxford, 1959).

[114] W. E. Gifford, in *Advances in cryogenic engineering* (Springer, 1966), pp. 152–159.

[115] M. Schreier et al., Applied Physics Letters **103**, 242404 (2013).

[116] J. B. S. Mendes et al., Phys. Rev. B **89**, 140406 (2014).

[117] H. Jin et al., Phys. Rev. B **92**, 054436 (2015).

[118] G. Subramanyam et al., Journal of Applied Physics **114**, 191301 (2013).

[119] R. K. Singh and J. Narayan, Phys. Rev. B **41**, 8843–8859 (1990).

[120] P. Sigmund, Phys. Rev. **184**, 383–416 (1969).

[121] S Swann, Physics in technology **19**, 67 (1988).

[122] G. Betz, Surface Science **92**, 283–309 (1980).

[123] K. Ishii, Journal of Vacuum Science & Technology A: Vacuum, Surfaces, and Films **7**, 256–258 (1989).

[124] M. Bellardita et al., in *Heterogeneous photocatalysis*, edited by G. MarcÃň and L. Palmisano (Elsevier, 2019), pp. 25 –56.

[125] S. Bedanta et al., Review of Scientific Instruments **76**, 083910 (2005).

[126] E. Saitoh et al., Applied Physics Letters **88**, 182509 (2006).

[127] Y.-J. Chen and S.-Y. Huang, Phys. Rev. Lett. **117**, 247201 (2016).

[128] R. Iguchi et al., Phys. Rev. B **95**, 174401 (2017).

[129] S. Wang et al., Nanoscale **7**, 17812–17819 (2015).

[130] T. Kikkawa et al., Phys. Rev. B **92**, 064413 (2015).

[131] U. Ritzmann et al., Phys. Rev. B **92**, 174411 (2015).

[132] E.-J. Guo et al., Phys. Rev. X **6**, 031012 (2016).

[133] R Ramos et al., Applied Physics Letters **102**, 072413 (2013).

[134] B. W. Wu et al., Phys. Rev. B **96**, 060402 (2017).

[135] R. Ramos et al., Phys. Rev. B **90**, 054422 (2014).

[136] L. Berger, Phys. Rev. B **5**, 1862–1870 (1972).

[137] T. Kikkawa et al., Phys. Rev. B **88**, 214403 (2013).

[138] I Diniz and A. T. Costa, New Journal of Physics **18**, 052002 (2016).

[139] S. R. Boona, New Journal of Physics **18**, 061002 (2016).

[140] M. B. Salamon and M. Jaime, Rev. Mod. Phys. **73**, 583–628 (2001).

[141] G. Campillo et al., Journal of Magnetism and Magnetic Materials **237**, 61 –68 (2001).

[142] G. J. Snyder et al., Phys. Rev. B **53**, 14434–14444 (1996).

[143] , Journal of Magnetism and Magnetic Materials **238**, 160 –167 (2002).

[144] M. F. Hundley et al., Applied Physics Letters **67**, 860–862 (1995).

[145] D. Kim et al., Phys. Rev. Lett. **89**, 227202 (2002).

[146] H Huhtinen et al., Journal of applied physics **91**, 7944–7946 (2002).

[147] D. Tian et al., Applied Physics Letters **106**, 212407 (2015).

[148] S. M. Wu et al., Applied Physics Letters **105**, 092409 (2014).

[149] Y. Xu et al., Applied Physics Letters **105**, 242404 (2014).

[150] V. Castel et al., Applied Physics Letters **101**, 132414 (2012).

[151] C. Du et al., Journal of Applied Physics **117**, 172603 (2015).

[152] J. Xiao et al., Phys. Rev. B **82**, 099904 (2010).

[153] S. R. Marmion et al., Phys. Rev. B **89**, 220404 (2014).

[154] Y. M. Lu et al., Phys. Rev. Lett. **110**, 147207 (2013).

[155] S. Y. Huang et al., Phys. Rev. Lett. **109**, 107204 (2012).

[156] W Schnelle et al., Journal of Physics D: Applied Physics **34**, 846 (2001).

[157] J. L. Cohn et al., Phys. Rev. B **56**, R8495–R8498 (1997).

[158] M. T. Buscaglia et al., Journal of the European Ceramic Society **34**, 307–316 (2014).

[159] S. R. Boona and J. P. Heremans, Phys. Rev. B **90**, 064421 (2014).

[160] S. Etesami et al., Applied Physics Letters **107**, 132402 (2015).

[161] J. Barker and G. E. W. Bauer, Phys. Rev. Lett. **117**, 217201 (2016).

[162] H. Adachi et al., Journal of Physics D: Applied Physics **51**, 144001 (2018).

[163] A. Berger et al., Journal of applied physics **91**, 8393–8395 (2002).

[164] S. Taran et al., Journal of applied physics **98**, 103903 (2005).

[165] Y. Wang et al., Applied Physics Letters **105**, 152412 (2014).

[166] M. Isasa et al., Phys. Rev. B **91**, 024402 (2015).

[167] J. W. Lynn et al., Phys. Rev. Lett. **76**, 4046–4049 (1996).

[168] V Dyakonov et al., Journal of applied physics **93**, 2100–2106 (2003).

[169] H. Nakayama et al., Phys. Rev. B **85**, 144408 (2012).

[170] O. Mosendz et al., Phys. Rev. Lett. **104**, 046601 (2010).

[171] T. K. H. Pham et al., Scientific reports **8**, 1–8 (2018).

[172] C. Swindells et al., Phys. Rev. B **99**, 064406 (2019).

[173] W. Cao et al., Phys. Rev. B **99**, 094406 (2019).

[174] A. Ghosh et al., Phys. Rev. Lett. **109**, 127202 (2012).

[175] C. L. Jermain et al., Phys. Rev. B **95**, 174411 (2017).

[176] M Haidar et al., Journal of Applied Physics **117**, 17D119 (2015).

[177] J. Marcos et al., Phys. Rev. B **68**, 094401 (2003).

[178] M. Qian et al., Scientific reports **8**, 16574 (2018).

[179] C. Biswas et al., Appl. Phys. Lett. **86**, 202508 (2005).

[180] M. Chmielus et al., Nat. Mater **8**, 863 (2009).

[181] A. Likhachev and K. Ullakko, Physics Letters A **275**, 142 –151 (2000).

[182] A. Sozinov et al., Appl. Phys. Lett. **80**, 1746–1748 (2002).

[183] A. Sozinov et al., Appl. Phys. Lett. **102**, 021902 (2013).

[184] P. Webster et al., Philosophical Magazine B **49**, 295–310 (1984).

[185] P. J. Brown et al., J. Phys. Condens. Matter **14**, 10159–10171 (2002).

[186] S. Singh et al., J. Phys. Condens. Matter **25**, 212203 (2013).

[187] S. Singh et al., Phys. Rev. B **90**, 014109 (2014).

[188] A. Zheludev et al., Phys. Rev. B **54**, 15045–15050 (1996).

[189] S. Singh et al., Phys. Rev. B **92**, 054112 (2015).

[190] A. Zheludev et al., Phys. Rev. B **51**, 11310–11314 (1995).

[191] S. Kaufmann et al., Phys. Rev. Lett. **104**, 145702 (2010).

[192] T. Fukuda et al., Scr. Mater **61**, 473 –476 (2009).

[193] L. Righi et al., Acta Mater. **55**, 5237 –5245 (2007).

[194] S. J. Murray et al., Applied Physics Letters **77**, 886–888 (2000).

[195] A. Planes et al., Phys. Rev. Lett. **79**, 3926–3929 (1997).

[196] G. Lantz et al., Phys. Rev. Lett. **119**, 227207 (2017).

[197] S. Banik et al., Phys. Rev. B **74**, 085110 (2006).

[198] V. V. Khovaylo et al., Phys. Rev. B **72**, 224408 (2005).

[199] A. N. Vasil'ev et al., Phys. Rev. B **59**, 1113–1120 (1999).

[200] B. Ludwig et al., Physical Review B **80**, 144102 (2009).

[201] B. JM et al., Applied Physics Letters **94**, 051909 (2009).

[202] C. YT et al., Journal of Physics: Condensed Matter **16**, 3061 (2004).

[203] W. WH et al., Journal of Physics: Condensed Matter **13**, 2607 (2001).

[204] F. Zuo et al., Phys. Rev. B **58**, 11127–11130 (1998).

[205] G. Y. Guo et al., Phys. Rev. B **89**, 214406 (2014).

[206] A. G. Khachaturyan et al., Phys. Rev. B **43**, 10832–10843 (1991).

[207] L. Mañosa et al., Phys. Rev. B **64**, 024305 (2001).

[208] S. M Shapiro et al., Europhysics Letters (EPL) **77**, 56004 (2007).

[209] S. W. D'Souza et al., Phys. Rev. B **85**, 085123 (2012).

[210] M. Belesi et al., Phys. Rev. B **91**, 134415 (2015).

[211] C. P. Opeil et al., Phys. Rev. Lett. **100**, 165703 (2008).

[212] C. Bungaro et al., Phys. Rev. B **68**, 134104 (2003).

[213] Y. Lee et al., Phys. Rev. B **66**, 054424 (2002).

[214] T. D. Haynes et al., New Journal of Physics **14**, 035020 (2012).

[215] F. Li et al., Journal of Superconductivity and Novel Magnetism **32**, 3183–3189 (2019).

[216] S. M. Wu et al., Applied Physics Letters **111**, 223109 (2017).

[217] B. Dóra et al., Phys. Rev. B **68**, 241102 (2003).

[218] K. K. Kolincio et al., Phys. Rev. B **94**, 241118 (2016).

[219] S. N. Guin et al., NPG Asia Mater. **11**, 16 (2019).

[220] A. Sakai et al., Nat. Phys **14**, 1119 (2018).

[221] E. Liu et al., Nature physics **14**, 1125–1131 (2018).

[222] A. K. Nayak et al., Science Advances **2**, e1501870 (2016).

[223] G.-Y. Guo and T.-C. Wang, Phys. Rev. B **96**, 224415 (2017).

[224] M. Onoda et al., Phys. Rev. Lett. **93**, 083901 (2004).

[225] O. Hosten and P. Kwiat, Science **319**, 787–790 (2008).

[226] Y. Kagan and L. A. Maksimov, Phys. Rev. Lett. **100**, 145902 (2008).

[227] A. A. Biswas and Y. Jana, Journal of magnetism and magnetic materials **329**, 118–124 (2013).

[228] A. Haghighirad et al., Journal of crystal growth **310**, 2277–2283 (2008).

[229] H. J. Xiang et al., Phys. Rev. B **83**, 174402 (2011).

[230] A. Mook et al., Phys. Rev. Lett. **117**, 157204 (2016).

[231] A. Mook et al., Phys. Rev. B **89**, 134409 (2014).

[232] D.-J. Kim et al., Nature Communications **8**, 1400 (2017).

[233] P. Sheng et al., Science Advances **3**, e1701503 (2017).

[234] A. De et al., Phys. Rev. Lett. **124**, 017203 (2020).

[235] K. Mallick et al., Phys. Rev. B **100**, 224403 (2019).

[236] M. Kockert et al., Journal of Applied Physics **126**, 105106 (2019).

[237] C. Moulsdale et al., Phys. Rev. B **99**, 214424 (2019).

[238] A. Kobs et al., Phys. Rev. Lett. **106**, 217207 (2011).

[239] L. Zhou et al., Science Advances **4**, eaao3318 (2018).

[240] M. Althammer et al., Phys. Rev. B **87**, 224401 (2013).

[241] N. Vlietstra et al., Phys. Rev. B **87**, 184421 (2013).

[242] S. Vélez et al., Phys. Rev. Lett. **116**, 016603 (2016).

[243] G. N. Grannemann and L. Berger, Phys. Rev. B **13**, 2072–2079 (1976).

[244] M. E. Lucassen et al., Applied Physics Letters **99**, 262506 (2011).

[245] S. J. Watzman et al., Phys. Rev. B **94**, 144407 (2016).

[246] M. V. Costache et al., Nature Materials **11**, 199–202 (2012).

[247] T. Yamaguchi et al., Phys. Rev. B **99**, 094425 (2019).

[248] B. Flebus et al., EPL (Europhysics Letters) **115**, 57004 (2016).

[249] V. A. Zyuzin and A. A. Kovalev, Phys. Rev. B **97**, 174407 (2018).